UNIVERSIDAD DE CHILE
FACULTAD DE CIENCIAS FÍSICAS Y MATEMÁTICAS
DEPARTAMENTO DE ASTRONOMÍA

PHOTOMETRIC REDSHIFTS IN THE HDFS

TESIS PARA OPTAR AL GRADO DE MAGÍSTER EN CIENCIAS MENCIÓN ASTRONOMÍA

SIMÓN YECO SILVA FERNÁNDEZ

PROFESOR GUÍA:
PAULINA LIRA TEILLERY

MIEMBROS DE LA COMISIÓN:
LEOPOLDO INFANTE LIRA
SEBASTIÁN LÓPEZ MORALES
RICARDO MUÑOZ VIDAL

SANTIAGO DE CHILE
2015

RESUMEN DE LA TESIS PARA OPTAR AL GRADO DE:
Magíster en Ciencias con Mención Astronomía
POR: Simón Yeco Silva Fernández
FECHA: 19/01/2015
PROFESOR GUÍA: Paulina Lira Teillery

PHOTOMETRIC REDSHIFTS IN THE HDFS

Se presenta fotometría óptica en 11 bandas medias a partir de observaciones realizadas con el telescopio de 2.2m en LSO (WFI) sobre un campo de $\sim 30' \times 30'$ deg extendido en el Hubble Deep Field-South (EHDF-S), el cual es uno de los campos que contiene información en multibandas como parte del Multiwavelength Survey by Yale-Chile (MUSYC). Este campo tiene una gran cantidad de datos públicos y datos auxiliares en bandas UV, óptico, infrarrojo cercano e infrarrojo lejano. Se determinaron aperturas óptimas para fotometría de alta precisión para diversas fuentes y brillos. Se proporcionan incertezas en magnitud a través de una técnica mejorada que considera correlaciones a mayor y menor escala en el ruido. Se incluyen datos auxiliares en el óptico a partir del catálogo de MUSYC en bandas $UBVRIz'$ hasta una magnitud total de $R_{\rm AB} = 25$, además de datos en infrarrojo cercano JHK de dos campos de $10' \times 10'$ deg con profundidades de $J \sim 22.5$, $H \sim 21.5$ y $K \sim 21$ (5 σ; Vega).

Se creó un catálogo fotométrico de ~ 62.000 galaxias detectadas en la imagen BVR de MUSYC. Se miden *redshifts* fotométricos mediante el código EAzY y se compara con ~ 500 fuentes identificadas espectroscópicamente con la finalidad de probar la precisión y desempeño de los filtros en bandas medias. Los *redshifts* fotométricos resultaron más confiables para $R < 24$ cuando la muestra contiene ~ 12.000 galaxias, particularmente en $0.1 < z < 1.2$, región de sampleo en el óptico de características como el quiebre de Balmer. La precisión de los *redshifts* fotométricos en $\Delta z/(1+z)$ es de 0.029, lo cual es comparable a estudios recientes con un mejoramiento del 20%. Estos valores se degradan en calidad para galaxias más débiles o cuando se utilizan menos bandas. Como demostración de la calidad de los resultados, se derivan tipos espectrales de las fuentes, luego se construyen funciones de luminosidad para comparar con trabajos similares, y así confirmar la fuerte dependencia de las SEDs con la densidad numérica de fuentes.

Se incorporan datos observacionales en radio en el HDFS del Australia Telescopio Hubble Deep Field-South para estudiar en detalle su población. Este proyecto realizó observaciones en cuatro longitudes de onda, 20, 11, 6 y 3 cm y alcanza una sensibilidad en rms alrededor de 10 μ Jy para cada longitud de onda. Utilizando una muestra de 227 fuentes en radio seleccionadas, se realiza una clasificación detallada de la población en AGNs (-loud de radio (9%) y -quiet (46 $\%$)), galaxias con formación estelar (SFG; 39%), y galaxias normales (6%), usando los *redshifts* fotométricos, información en multibanda, un template combinado quasares, índices espectrales, las SEDs derivadas y la dependencia redshift-luminosidad.

Se confirman los resultados recientes sobre la disribución de AGNs y SFGs. Asimismo las LFs muestran consistencia para las fuentes en radio para $z \sim 1.0$. Los resultados obtenidos siguen la tendencia de los trabajos previos de los últimos 4 a 5 años en la distribución de las fuentes de radio, y sugiere nuevas metodologías en torno a la caracterizacón la población en radio.

Abstract

We present optical 11-medium-band photometry from observations made with the Wide Field Imager (WFI) instrument on the 2.2m telescope at LSO over the $\sim 30' \times 30'$ deg Extended Hubble Deep Field-South (EHDF-S), which is one of the fields comprising the Multiwavelength Survey by Yale-Chile (MUSYC). This field has a wealth of deep public ground- and space-based ancillary data at UV, optical, near-infrared, and far-infrared wavelengths. We determine optimal apertures for accurate photometry for a broad number of object sizes and brightnesses, and provide their uncertainties through an improved technique that considers small and large scale noise correlations. We include ancillary data in our catalog from the MUSYC Survey in optical $UBVRIz'$ images to a total magnitude of $R_{\rm AB} = 25$, and deep near-infrared JHK imaging data, of two $10' \times 10'$ fields, with point-source limiting depths of $J \sim 22.5$, $H \sim 21.5$, and $K \sim 21$ (5σ; Vega). We create a photometric catalog of ~ 62000 galaxies detected in the MUSYC $''BVR''$ image with $R_{\rm AB} \leq 25$ and made multi-color classification . Photometric redshift measurements are accomplished using the EAzY code and compared to nearly ~ 500 spectroscopically identified objects in the field in order to test the accuracy and performance of the medium-band filters which were designed to maximize the accuracy of photometric redshifts. Photometric redshifts are most reliable at $R < 24$ where the sample contains ~ 12000 galaxies, particularly at $0.1 < z < 1.2$, by evenly sampling the optical range and strong continuum features such as a Balmer break. Galaxy photometric redshifts are accurate to a 1σ scatter in $\Delta z/(1+z)$ of 0.029, which is similar to comparable works and represent an improvement on photometric redshift estimates over a 20%. These values degrade in quality for fainter galaxies or when less bands are used. As a demonstration of the quality data, we used available UV-optical template spectra of quiescent and starburst galaxies to derive spectral types of our sources and then construct luminosity functions to compare with similar works, and confirm the strong SED-type dependence at all redshifts covered. We used radio observations data on the HDFS drawn by the Australia Telescope Hubble Deep Field-South radio survey to study

in detail its population. This survey was conducted at four wavelengths, 20, 11, 6, and 3 cm and achieves an rms sensitivity of about 10 μJy at each wavelength. Using a sample of 227 of theses radio-selected galaxies we performed a detailed classification of the population into AGNs (radio -loud (9%) and -quiet (46%)), star-forming galaxies (39%), and normal galaxies (6%), using: a wealth of multiwavelength information in the radio and optical bands, fits with tested quasar template spectra, radio spectral index when available, SED-types and redshift-luminosity dependence. Due to the faint radio levels reached by the radio data, we confirm recent results about the higher contribution at submilijansky levels from radio quiet AGNs. Our accurate photometric redshifts allow us to derive reliable radio luminosity functions for our subsets out to $z \sim 1.0$. Our results follow the trend of previous works for the past 4 to 5 years on the distribution of radio sources, and suggest new insights on establishing the nature of sources in a radio population.

Acknowledges

Cuando pienso en esta sección descubro que en estos minutos transcurridos ya habría escrito varios párrafos de mi trabajo, en cambio en ésto llevo sólo dos líneas. Inevitablemente me emociono y me cuesta mucho como siempre expresar lo humano que vive en mí. Pero son mis padres, claro que sí, Cecilia y Eduardo a quienes debo la vida, los primeros en agradecer; ellos siempre priorizaron mi educación, mi bienestar, mi felicidad, y todos aquellos factores que me han permitido crecer como ser persona y estudiante. En mi línea de tiempo también aparece Sergio con su amor incondicional, a quien he querido y admirado como padre.

Agradezco muy especialmente a mi hermano Leonardo, por todas las conversaciones y experiencias vividas, y con quien de las peleas de niños pasamos a ser amigos inseparables. A mi hermana Rayén, quien durante mi niñez me sorprendía con su arte mientras los números eran lo mío, y quien me enseñó a concentrarme en la lectura mientras leía *Mac, el microbio desconocido*, aunque dudo ella lo recuerde. Dedico también este trabajo a mi prima Paula, con quien comparto muchos intereses y además manejamos un lenguaje que nos permite entender la vida desde el razonamiento y la experimentación. Agradezco mucho a Carolina por acompañarme en estos últimos dos años, quien con sus encantos ha hecho de cada tormenta un paraíso. A Patricia, por toda su generosidad y quien es indudablemente la mejor mujer que puede acompañar a mi padre. A toda mi enorme familia.

Debo dar las gracias a Paulina, mi profesora guía. Aunque más allá de todo su apoyo, compromiso y presencia constante en este trabajo, como así también tolerancia hacia mi personalidad académica y profesional dispersa, debo reconocer que ha sido su severidad la que me permitió sentarme hace unos años a pensar que es lo que realmente quiero profesionalmente. También agradezco a mis amigos y compañeros de la vida, aunque entre amigos las frases de agradecimiento estén de más: Beatriz y Francisco desde la niñez y la adolescencia; Fernando, Gabriela y Klaus por las maravillosas experiencias de la U; el cómo nos ponemos viejos con Israel y Claudio; y todos quienes me hayan dado un espacio en sus vidas.

Contents

1 Introduction **1**

2 Observations **3**

2.1 The MUSYC Survey 3

2.2 The Extended Hubble Deep Field South (EHDF-S) 4

2.3 MediumBand Optical Imaging 5

3 Data Reduction **7**

3.1 Image Processing 8

3.2 Astrometric Treatment 8

3.3 Final Images 8

4 Ancillary Data **10**

4.1 Deep Optical $\mathbf{UBVRIz'}$ Data 11

4.2 Deep Near-Infrared $\mathbf{JHK}$ Data 12

4.3 Radio Data at Wavelengths 20, 11, 6, and 3 cm 13

4.4 COMBO-17 13

5 Photometry **15**

5.1 Photometric Calibration 15
5.2 Noise Properties at Small and Large Scales 16
5.3 Optimal Apertures for Photometry 20
5.4 Source Detection and Aperture Photometry 24
5.5 Photometric Errors & Fluxes 27
5.6 The Photometric Catalog 27

6 Classification **30**

6.1 Star/Galaxy Separation 30
6.2 Number Counts 35

7 Redshifts **38**

7.1 EAZY($E_{asy\ and}$ $A_{ccurate}$ $Z_{(photometric\ redshifts)\ from}$ Y_{ale}) 39
7.2 Spectroscopic Redshifts 42
7.3 Photometric Redshifts 43
7.3.1 The Performance of Medium-Band Filters 44
7.3.2 The Performance of Near-Infrared Bands 45
7.3.3 Photometric Redshift Accuracy 45

8 Luminosity Functions of Radio Sources. **53**

8.1 The Luminosity Function 54
8.2 Luminosity Functions by Spectral Type of Radio Sources 55
8.2.1 Galaxy Spectral Classification 56
8.2.2 The SED Type Dependence: General results 58
8.2.3 The Redshift Evolution of M^* and ϕ^* Since $\mathbf{z \sim 1}$. 60

8.3 Luminosity Functions of Radio Detected AGN and SFGs 62

8.3.1 AGN / SFG Separation 62

8.3.2 Radio Luminosity Functions for AGNs and SFGs at $z < 1$. 74

9 Summary and Conclusions **80**

10 Bibliography **83**

Chapter 1

Introduction

Studies concerning the formation and evolution of distant galaxies and active galactic nuclei (AGNs) are at the forefront of ongoing astrophysical research. New and more sophisticated techniques to determine distances and associated look-back times have been developed, along with the identification of the basic physical processes that drive the formation and evolution of galaxies, such as the gravitational collapse of baryons in the potential well of dark matter halos, the efforts on tracing the variation in star formation rates with time, and the consequences of galaxy mergers. However, modelling these observed properties for a wide range of galaxy types and redshifts has proven exceedingly difficult. Even though a precise determination of the cosmological parameters has removed some of the uncertainties in galaxy models, it is largely accepted that comprehensive observations of galaxies at low and high redshifts are necessary to yield an understanding of galaxy evolution.

An efficient method for assembling large redshift samples for faint galaxies, is the determination of photometric redshifts (photo-z), which are an estimate of galaxy distances based on the observed colors (Baum 1962). For optically bright objects, redshifts can be mesured efficiently with multi-slit spectrographs on large telescopes. However, spectroscopic redshift measurements are very difficult for galaxies and AGNs that are at $z > 1$, obscured, or intrinsically faint. As a result, we have to rely almost exclusively on photometric redshifts determined

from broadband photometry for galaxies with $I \geq 23$ (see, e.g., Grazian et al. 2006; Wuyts et al. 2009, and many other studies). Despite having a lower accuracy than spectroscopic redshifts (spec-z), phot-z have the convenience of improving completeness down to a flux limit fainter than the spectroscopic limit.

The COMBO-17 survey (Wolf et al. 2004) provided deep photo-z samples and pioneered the use of medium-bandwidth filters as a compromise between imaging and spectroscopy. These filters sample the spectral energy distributions (SEDs) of galaxies at a resolution of $R = 10 - 20$ and provide a redshift quality of 1%-2%, intermediate between spectroscopy and broadband imaging. This improvement enables measurements of rest-frame colors and the environment of galaxies by identifying clustered populations, and improves the accuracy of determinations of the physical properties of galaxies. It also opens up the possibility of directly detecting strong emission lines, which is particularly relevant for the identification of AGN.

In this work the method of using medium-band photometry will be applied to the study of the Hubble Deep Field South. The derived distances will be then used to study the radio properties of galaxies in this field. Throughout this work we assume a standard ΛCDM cosmology with $H_0 = 70$ km^{-1} s^{-1} Mpc^{-1}, $\Omega_m = 0.3,$ and $\Omega_\Lambda = 0.7$. Magnitudes are mainly given in the AB system.

Chapter 2

Observations

2.1 The MUSYC Survey

The MUltiwavelength Survey by Yale-Chile (MUSYC[1], Gawiser et al. 2006) was mainly carried out to study the formation and evolution of galaxies and their central black holes. More specifically they attempt to study the properties and interrrelations of galaxies at $z \sim 3$. In order to obtain large samples of objects, four fields comprising about one square degree of the sky were observed (Table I). These $30' \times 30'$ imaged regions, have deep observations in optical and near-infrared passbands along with extensive follow up spectroscopy to the limit of $R \simeq 25$, and were carefully selected to have very low Galactic reddening, H I column density to reduce the effect of the galactic interstellar medium (Burstein & Heiles 1978), 100μm dust emission (Schlegel et al. 1998), to cover a wide range in right ascension, accessibility to ground-based observations from the southern hemisphere, and high Galactic latitude ($|b| > 30$) to reduce stellar density. Some of these fields also benefit from space-based imaging in the X-ray, optical, and infrared by *Chandra* and *XMM*, *Hubble Space Telescope* and *Spitzer* respectively. The exact locations of the deep MUSYC fields within the larger $30' \times 30'$ fields were chosen to avoid bright stars.

[1]Updated information and data releases are available at http://www.astro.yale.edu/MUSYC.

Table I: MUSYC Fields

Field	R.A. (J2000.0)	Decl. (J2000.0)	Galactic Coordinates (deg)	Ecliptic Coordinates (deg)	$E(B-V)$	$100\mu m$ Emission (MJy sr^{-1})	$N(HI)$ (cm^{-2})
EHDF-S.....	22:32:35.6	-60:47:12	(328,-49)	(311,-47)	0.03	1.37	1.6E+20
ECDF-S.....	03:32:29.0	-27:48:47	(224,-54)	(41,-45)	0.01	0.40	9.0E+19
SDSS1030+05.....	10:30:27.1	05:24:55	(239,50)	(157,-4)	0.02	1.01	2.3E+20
CW 1255+01.....	12:55:40.0	01:07:00	(306,-64)	(192,7)	0.02	0.81	1.6E+20

These fields were observed in the $UBVRIz'$ filters for a total optical coverage (Gawiser et al. 2006), reaching AB depths of $U, B, V, R = 26.5$. Lyα emitters were identified through a narrowband 50 $\AA$ FWHM filter centered at 5000 $\AA$. The four $30' \times 30'$ fields were also observed in at least one of the J, H and K bands. Four $10' \times 10'$ subfields were observed to greater depth in all of JHK bands (Quadri et al. 2007). Two of them are adjacent and lie within the EHDF-S, reaching point-source limiting depths of $J \sim 22.5$, $H \sim 21.5$ and $K \sim 21$ (5σ; Vega). Thanks to its unique combination of wavelength coverage, depth and total area, MUSYC covers the gap between deep narrow surveys like GOODS (Great Observatories Origins Deep Survey) and shallow wide surveys such as the EIS Deep Public Survey or the Las Campanas Infra-Red Survey (LCIRS).

2.2 The Extended Hubble Deep Field South (EHDF-S)

The extended area of the Hubble Deep Field-South (Table I) covers a 0.32 deg^2 region and has deep public space-based observations at UV, optical, near-infrared, and far-infrared wavelengths. The center of this field center was chosen to keep a bright star ($m = 6.8$) which lies quite close to the WFPC2 field off of the CTIO+MOSAIC detectors. This extended area has previously been imaged by Palunas et al. 2000 and Teplitz et al. 2001, both in broadband $uBVRI$, reaching ~ 24 mag, which enables a reliable study of galaxies out to $z \sim 1$. These images were published and combined with deep H-band images by the Las Campanas Infrared Survey (LCIRS, Chen et al. 2003) to study red galaxies out to $z \sim 1.5$. The HDFS itself also covers a small $\sim 2.'5 \times 2.'5$ central region with WFPC2 plus STIS and NICMOS regions,

with deep ground-based JHK coverage of the WFPC2 region available from the Faint Infrared Extragalactic Survey (FIRES) (Labbé et al. 2003). Futher imaging in near- and far-infrared have been performed by Spitzer IRAC and MIPS of the central $5' \times 15'$ in Guaranteed Time Observation (GTO) time. MUSYC survey goes about one magnitude deeper than previous imaging in $UBVRIz'$ to probe the $z = 3$ universe. The imaging and catalogues for the EHDF-S are published in Gawiser et al. 2006 along with the techniques used for data reduction and photometry.

2.3 MediumBand Optical Imaging

The MediumBand survey was created to obtain medium band optical imaging of the EHDF-S. The observations were made with the Wide Field Imager (WFI) instrument on the 2.2m telescope at LSO in 11 different filters. The Wide Field Imager (WFI) is a focal reducer-type camera which is permanently mounted at the Cassegrain focus of the 2.2-m MPG/ESO telescope at La Silla. This instrument consists of a mosaic camera of eight CCDs of 2000 $\times$ 4000 pixels each, providing a field of view of 34' $\times$ 33' with a pixel scale of 0".238 pixel^{-1}. It offers excellent sensitivity from 350 nm to the near IR, with more than 40 filters simultaneously available, many of them specifically selected to support the determination of photometric redshifts of distant objects. We show the medium-band filter response curves in Figure 2.1. The use of a medium-band filter set was designed to maximize the accuracy of photometric redshifts and they were chosen to be arrange among the $UBVRIz'$ filter set with an effective resolution of $\lambda/\Delta\lambda \sim 23$.

Table II gives detailed information of the total exposure times in each medium band filter for each run, along with the filter FWHM and its center, and the epoch when the observations were performed.

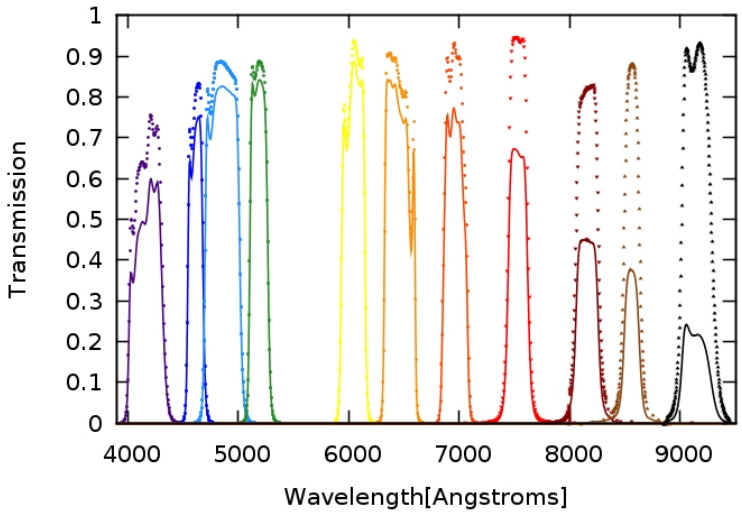

Figure 2.1: WFI medium-band filter transmission curves. Dotted lines represent filter throughput, and solid lines include atmospheric transmission and quantum efficiency. The filter set samples the wavelength range from 4000 to 9000 $\mathring{A}$.

Table II: Optical Medium-Band Observations with WFI on La Silla 2.2m on the HDFS.

Filter	λ_{cen}/FWHM (nm)	Dates	Total Exposure Time (s)
ESO872.....	416/29	2004 Sep 9, 13, 18, 19 2006 Aug 17	21060
ESO874.....	461/13	2004 Sep 9, 14, 16 2006 Aug 17	9360
ESO860.....	485/31	2004 Sep 9, 15, 16	6435
ESO862.....	518/16	2004 Sep 9, 14, 17	6435
ESO864.....	604/21	2004 Sep 9, 15, 16	6435
ESO867.....	646/27	2004 Sep 9 2006 Aug 24	3510
ESO869.....	696/20	2004 Sep 9, 14 2006 Aug 17, 28	6435
ESO848.....	753/18	2004 Sep 9, 13, 16 2006 Aug 28	9360
ESO851.....	815/20	2004 Sep 9, 14, 16, 17	18135
ESO853.....	856/14	2004 Sep 9, 13, 14 2005 Nov 8 2006 Sep 23	18135
ESO854.....	914/27	2004 Jul 7 2004 Sep 9, 10, 15 2006 Sep 24, 25	15795

Chapter 3

Data Reduction

The image reduction process was performed by María Fernanda Durán as a member of MUSYC. We will very briefly describe the procedure which follows that of Gawiser et al. 2006. The Wide Field Imager information is summarized in Table I.

Table I: Wide Field Imager Information Summary.

WFI		Characteristics
Field of view	:	34'×33'
Pixel scale	:	0.238 arcsec/pixel
Detector	:	4x2 mosaic of 2kx4k CCDs
Filling factor	:	95.9%
Read-out time	:	27 seconds
Read-out noise	:	4.5 e-/pixel
(Inverse) Gain	:	2.0 e-/ADU
Dynamical range	:	16 bit
Full-well capacity	:	$>$ 200, 000e-
Telescope aperture	:	2.2 m
Telescope focus	:	Cassegrain (f/8)
Instrument F ratio	:	5.9
Wavelength range	:	Atmospheric cutoff to 1 micron
Intrinsic image quality	:	0.4 arcsec
Geometrical distortions	:	$\leq$ 0.08%
Raw data format	:	MEF, 142 Mbyte/file

3.1 Image Processing

For the treatment of the images we followed the standard procedure based on the NOAO Deep Wide-Field Survey (NDWFS) MOSAIC reduction notes available on line[1]. We mainly used IRAF[2] tasks from the `mscred` package. We also used the special package `esowfi` from mscred to work properly when dealing with images from LSO.

A master bias image was created for each observed night. Dark frames were not necessary due to low exposure times. Bad pixel masks were obtained from the support pages of LSO for the treatment of bad pixels. For the redder filters (ESO848, ESO851, ESO853 and ESO854) the fringing contribution was removed by creating a fringe template, which was scaled and substracted from each science image. Finally, to account for the sky gradient, a superflat was created from science images.

3.2 Astrometric Treatment

Due to some shifts in all the images respect to the original WCS written in the headers, `mscsetwcs`, `msccmatch`, `msctvmark` and `mscdisplay` tasks were used.

3.3 Final Images

Cosmic rays were rejected using the IRAF routine `craverage`, while large scale gradients were removed using `mscskysub`. In order to increase the signal-to-noise ratio, for each filter we produced three deep images by stacking all the science images. This was performed in three different ways: unweighted, with weights optimized for point sources and with weights optimized for extended sources. For each filter we are only using the point source optimized

[1] http://www.noao.edu/noao/noaodeep/ReductionOpt/frames.html

[2] IRAF is distribuited by the National Optical Astronomy Observatory, which is operated by the Association of Universities for Research in Astronomy, Inc., under a cooperative agreement with the National Science Foundation

weighted image during the subsequent analysis, as the optimal weights cause S/N to add in quadrature so it will never formally decrease no matter how poor an input image is.

Chapter 4

Ancillary Data

The extended area around the HDFS has a wealth of deep public ground- and space-based ancillary data at UV, optical, near-infrared, and far-infrared wavelengths. This field has previously been imaged by Palunas et al. 2000 and Teplitz et al. 2001 to a depth sufficient for the study of galaxies at $z < 1$. MUSYC $UBVRIz'$ optical imaging goes about one magnitude deeper to probe the $z = 3$ Universe (Gawiser et al. 2006). Additionally, the EHDF-S has a small $\sim 2.'5 \times 2.'5$ central region of the WFPC2 with deep JHK coverage from the Faint Infrared Extragalactic Survey (FIRES) (Labbé et al. 2003). *Spitzer* IRAC and MIPS coverage of the central $5' \times 15'$ has been obtained. Deep near-infrared JHK imaging was performed on two $10' \times 10'$ subfields of the HDFS by Quadri et al. 2007. Radio observations of the HDFS region were also performed by the ATHDFS (Australia Telescope Hubble Deep Field-South) survey at four wavelengths, 20, 11, 6, and 3 cm, over a 4 year period (Huynh et al. 2007).

The use of the ancillary data in our work is two-fold. First, existent MUSYC $UBVRIz'JHK$ data will be used in the determination of photometric redshifts and to create a uniform catalog along with our optical 11-medium bands. Second, we use radio observations at $1.4, 2.5, 5.2,$ and 8.7 GHz, and high-quality photometric redshifts, to investigate and discuss the nature of the radio luminosity function, and characterize radio sources from microjansky to high flux density levels. The shape of the available regions with wavelength coverage are drawn onto a BVR

image shown in Figure 4.1. These imaging fields are described in more detail throughout the next three sections. Observations, reduction, and characteristics of these data are described in detail in the cited references.

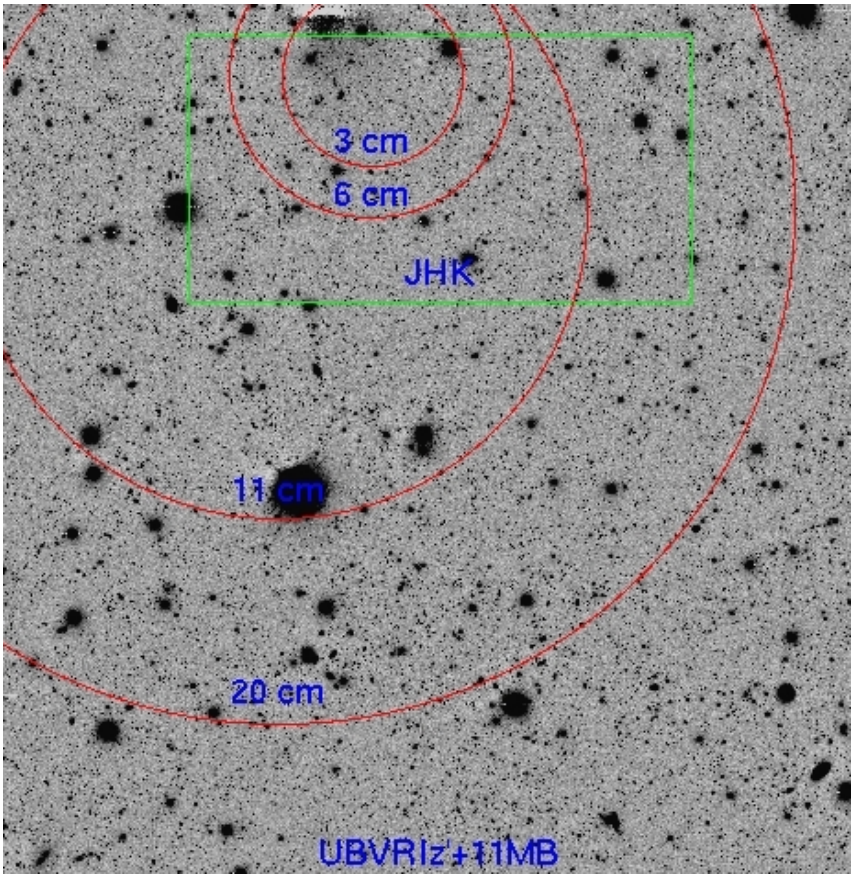

Figure 4.1: Deep combined BVR image of EHDF-S. The full region is covered by optical $UBVRIz'$ plus medium-band observations. Red circles represent the four pointings of the Australia Telescope Hubble Deep Field-South. Working inward, circles represent the cataloged areas of the 20, 11, 6, and 3 cm primary beams respectively. The green rectangle show the total area covered by deep near-infrared JHK data.

4.1 Deep Optical UBVRIz′ Data

The deep optical part of the survey was obtained with the MOSAIC camera on the 4m Blanco telescope at CTIO (Cerro Tololo Interamerican Observatory). Astrometric calibration, weighted image combination, and photometric calibration performed on the UBVRIz' images are fully described in Gawiser et al. 2006. The photometric catalog is complete to a total

magnitude of $R_{\rm AB} = 25$. Table I lists the characteristics of the final $UBVRIz'$ images, i.e. Filter effective wavelengths, PSF FWHM, zero points and 5 σ point source limiting depths.

Table I: Optical Broad Band Data.

Filter	$\lambda_{\rm eff}$ ($\AA$)	Zero Point (AB at 1 count s^{-1})	PSF FWHM arcsec	5 σ Depth (AB)
BVR	-	0.698	0.99	26.3
U	3652	1.660	1.48	26.0
B	4468	0.417	1.29	26.1
V	5505	0.251	0.96	26.0
R	6581	0.182	0.97	25.8
I	8059	0.283	0.99	24.7
z'	9114	0.637	1.06	23.6

4.2 Deep Near-Infrared JHK Data

The HDFS has been targeted with deep near-infrared JHK imaging of two $10' \times 10'$ fields: HDFS1 and HDFS2. We obtain the reduced near-infrared source catalogs from Quadri et al. 2007. The observations were carried out with the Infrared Sideport Imager (ISPI; Probst et al. 2003; van der Bliek et al. 2004) on the CTIO 4 m telescope. The reduction and characteristics of these data are described in Quadri et al. 2007. Table II lists the characteristics of the final JHK images, i.e. Filter effective wavelengths, PSF FWHM, zero points and 5 σ point source limiting depths.

Table II: Near-Infrared Data.

Field	Filter	$\lambda_{\rm eff}$ ($\AA$)	Zero Point (AB)	PSF FWHM arcsec	5 σ Depth (AB)
HDFS1.....	J	12461	23.30	0.96	22.9
	H	16306	23.88	0.96	21.8
	K'	21337	24.13	0.96	21.1
HDFS2.....	J	12470	23.07	1.05	22.5
	H	16366	23.92	1.03	21.4
	K_s	21537	23.97	1.00	20.8

4.3 Radio Data at Wavelengths 20, 11, 6, and 3 cm

The benefit on including radio observations is that they reveal a view of the universe unaffected by absorption, probing physical properties that are faint or unobservable at most other wavelengths. The Australia Telescope Hubble Deep Field-South survey has performed deep radio observations of a wide region centered on the Hubble Deep Field-South (Huynh et al. 2007). A central rms of $\sim 10\mu$Jy is reached at four frecuencies (1.4, 2.5, 5.2, and 8.7 GHz). Table III lists some characteristics and parameters of the radio final images, i.e. Pointings (J2000), synthesized beam (size and position angle), and rms sensitivity.

Table III: Four Frecuency ATCA Observations.

ν (GHz)	R.A. (J2000.0)	Dec (J2000.0)	$b_{\rm maj} \times b_{\rm min}$ (arcsec)	P.A. (deg)	rms (μJy)
1.4	22:33:25.96	-60:38:09.0	7.1×6.2	-5.5	11.0
2.5	22:33:25.96	-60:38:09.0	5.1×4.0	1.7	10.4
5.2	22:32:56.22	-60:33:02.7	3.0×2.2	10.7	7.8
8.7	22:32:56.22	-60:33:02.7	2.3×1.7	-1.6	11.0

We display the single pointings to identify between the 5.2 and 8.7 GHz observations which are centered on the HST WFPC field (Figure 4.1), while the 1.4 and 2.5 GHz observations were pointed halfway between the WFPC field and a bright confusing source as a strategy to deal with it.

4.4 COMBO-17

The COMBO-17 (Classifying Objects by Medium-Band Observations) project has imaged one square degree of the sky in 17 optical filters using the Wide Field Imager (see Baade et al. 1999) camera on the 2.2m telescope at La Silla Observatory. They have found ~ 25000 galaxies, ~ 300 QSOs and more than 5000 stars. The selected imaged regions comprehend the CDFS (R.A. 03:32:25, Decl. -27:48:50), the A 901 field (R.A. 09:56:17, Decl. -10:01:25), the S11 field (R.A. 11:42:58, Decl. -01:42:50), the SGP field (R.A. 00:45:56, Decl -29:35:15) and the

A226 field (R.A. 01:39:00, Decl. -10:11:00). COMBO-17 was mainly carried out to study the evolution of galaxies and their associated dark matter haloes at $z \leq 1$ as well as the evolution of quasars at $1 \leq z \leq 5$ (Wolf et al. 2004).

The main purpose on selecting this survey for comparison with our work is due to the same filter set we both used, which is composed by 5 optical broad-band filters and 12 medium-band filters, covering the whole optical range. This provides low resolution spectra which allow a reliable classification of objects and photometric redshift measurements. Also, exposure times are comparable, therefore we expect to reach similar photometric depths.

To characterize the performance when using medium-band filters to measure photometric redshifts, they compare to nearly 1000 spectroscopically identified objects, reaching accuracies of $\sigma_z \approx 0.03$. This value is among our expectations if we consider similar number of bands and depths in our images. This survey also uses deep and sharp R-band data to explore weak gravitational lensing. More information on the COMBO-17 project can be found on line[1].

[1] http://www.mpia-hd.mpg.de/COMBO/

Chapter 5

Photometry

To achieve uniform photometry for a variety of images in multiple bands as well as accurate photometric errors, special care must be taken on the selection of apertures, the treatment of the background fluctuations and the image calibration, to place all photometry on a standard flux scale, among others. Once we have a single final image for each medium-band filter, we use IRAF task `imalign` to shift and trim the images to match the final MUSYC BVR composite image in order to have a common orientation, size and scale for aperture photometry. This composite image is 7395$\times$ 7749 pixels or 33'$\times$ 34.5', which is the maximum size region that has nearly a uniform signal-to-noise ratio. In this section we discuss all the main aspects involved on the determination of a homogenous photometric catalog.

5.1 Photometric Calibration

In order to place all our medium-band images on a standard flux scale, we must calculate photometric zero points for each image. For photometrical calibration purposes we chose a spectrophotometric standard star, LTT9239, presented in Hamuy et al. 1992, which is suitable for calibrations in the southern hemisphere. This photometric calibration was performed by M. F. Durán and consists of the following steps.

To calculate the zero points for each medium-band, we used the expression

$$m = m_{\text{inst}} + \Psi \times A + Z_p \ , \tag{5.1}$$

where m_{inst} is the instrumental magnitude, Ψ is the mean airmass at the time of the observation, A is the extinction curve, m is the magnitude in the standard system, and Z_p is the zero point. IRAF packages were used to measure instrumental magnitudes. Extinctions are determined from the curve pusblished in the LSO website and interpolating it to match the central wavelength of each filter. Finally the magnitude in the standard system of the star is calculated multiplying the SED of the star by the transmission of the corresponding filter.

Then we calculate the relative shifts between zero points obtained under photometric and non-photometric conditions to form a final image from the stacked images which correponds to the entire dataset for each filter. Zeropoints are summarized in Table II. Finally, fluxes are normalized and the final image has units of flux per second.

5.2 Noise Properties at Small and Large Scales

The motivation for analizing the behaviour of the noise comes from understanding the nature of the background fluctuations in the final images which do not follow a Poissonian distribution. This has a direct impact in the determination of the nominal depth of each final image. The standard formula used by SExtractor (Bertin & Arnouts 1996) or IRAF to determine the flux uncertainty from background noise is $\sigma_{\text{back}} = \sigma_1 (N_{\text{pix}})^{1/2}$, where σ_1 is the standard deviation of background per pixel and N_{pix} is the number of pixels within circular apertures. This method is appropriate only if the flux uncertainties follow a Poissonian distribution which is uncorrelated between adjacent background pixels. However, neighboring pixels are correlated due the stacking image procedure performed to create a final image. The spacial transformations and background subtraction performed on the images, extended wings from bright objects, the presence of artifacs and objects undetected, along with some image imperfection factors, have

created correlations between neighboring pixels leading to a distribution far from poissonian for the large scale fluctuations of the sky. To characterize the noise properties and account for all of these effects, we follow the procedure outlined in Gawiser et al. 2006. This is carry out by placing different apertures with sizes ranging from 1 to 10 pixels in radius (0.238 to 2.38 arcsec) over ~ 1000 random empty regions that do not belong to the segmentation map created by SExtractor over each image as shown in the example of Figure 5.1. The images used in the analysis are the stacked normalized images that have been already transformed to match pixel-to-pixel the MUSYC BVR image.

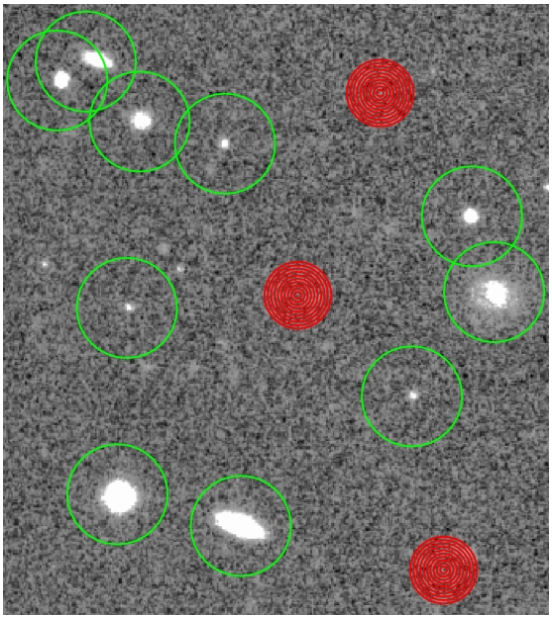

Figure 5.1: Selected region in ESO851 image showing 3 out of 1000 random regions (in red) with apertures sizes ranging from 1 to 10 pixels which do not overlap with objects detected by SExtractor (in green).

We first make histograms representing the distribution of aperture fluxes for 4, 6 and 8 pixels ($\sim 1'', 1.5''$and $2''$) apertures as shown in Figure 5.2. It is evident the roughly Gaussian distribution of flux in these apertures, which better describes the noise in the background of the image. Two things are inmediately apparent: the flux distributions are centered around $\sim$ zero flux, and the dispersion of observed fluxes is larger within larger apertures, as expected. Best-fit Gaussians are aproximated to the distributions in order to have a better visual information on the broaden dispersion or FWHM when increasing aperture size. The sigma width of the

fitted distribution measures the true uncertainty in the background noise, and varies within the aperture size used for photometry.

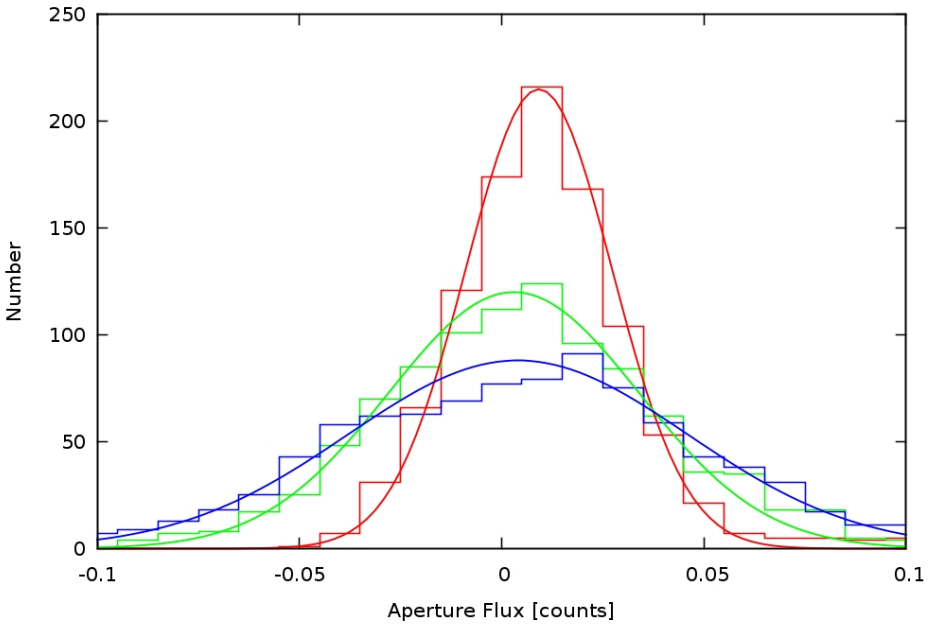

Figure 5.2: Histograms of aperture counts of background fluctuations in 4, 6 and 8 pixels, in red, green and blue respectively, of the ESO851 image. The larger aperture has the broader distribution of fluxes. These distributions are well-approximated by Gaussians.

After we obtain the measurements of the background rms for each aperture in a given filter, we produce a fit to the increasing behavior of the rms flux with aperture using

$$\sigma_{\rm back} = \sigma_1 \alpha N_{\rm pix}^{\beta} \ , \tag{5.2}$$

where α is a constant to be determined, and $1 < \beta < 2$ considers extreme limiting values depending on situations when correlations between pixels are perfectly introduced, yielding $\beta = 2$, or for a Poissonian noise contribution, when adjacent background pixels are uncorrelated, in which case $\beta = 1$. Then we rely on the simplicity of equation (5.2), which reflects the reality that noise exists on a range of scales leading to an effective power-law behavior intermediate between these two extreme.

Figure 5.3 shows how the rms of aperture fluxes changes with aperture size for all our final

medium band images. We made a fit to the changes in width of the best-fitting Gaussians by using the power law expressed in equation (5.2), where numerical values for the fit coefficients α and β of each image are determined and expressed in Table I along with the measured rms-per-pixel σ_1. We also show the limiting predictions for an rms proportional to N and N^2 in order to compare the noise correlations ranging from small to large scales respectively. It is clear that an improvement in the method used by SExtractor, which underestimate background fluctuations, must be performed to estimate accurate photometric errors.

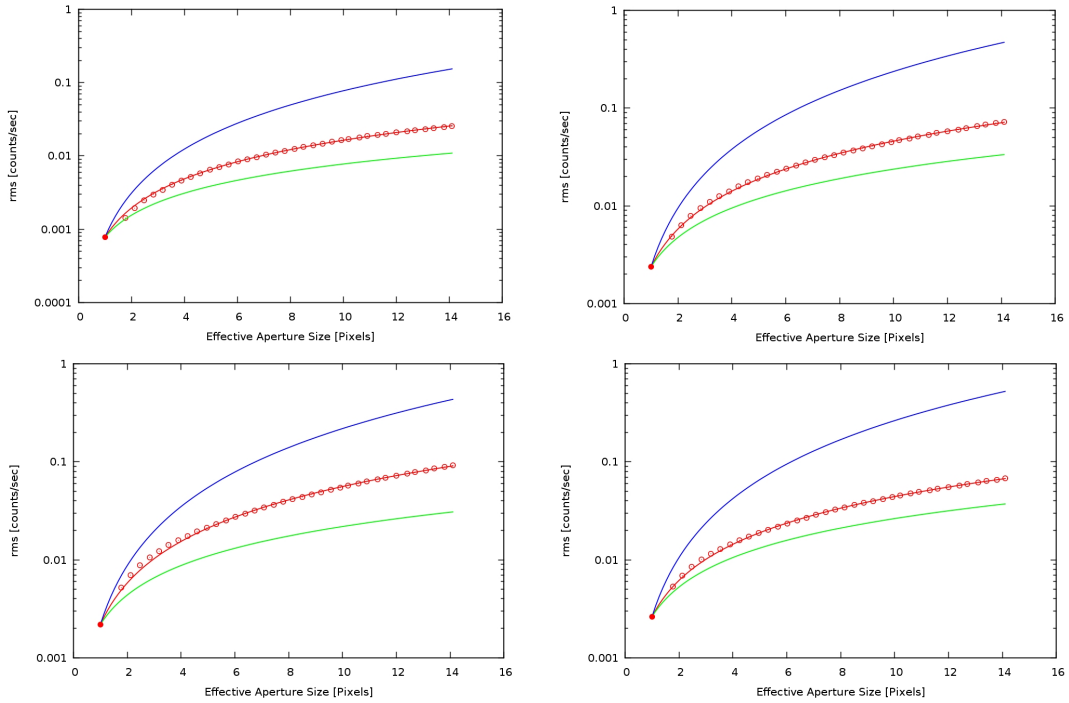

Figure 5.3: Rms fluctuations for four ramdomnly selected medium-band final images as a function of aperture size (red circles). Solid lines in blue ($\beta = 2$) and green ($\beta = 1$) represent the two limiting cases. The best fit to real rms fluctuations using the power law discussed in eq. (5.2), is presented in red.

Five σ depths were determined multiplying the rms of the sky noise for the optimal point source apertures sizes by 5 and corrected using equation (5.4). They are reported in Table II along with the size of the median FWHM, which was determined from a set of suitable stars using IRAF's *imexam* routine, which allows a Moffat fit, instead of SExtractor's *fwhm* parameter, which assumes a Gaussian PSF. The reason of this choice will be clarified in the next section.

Table I: Rms pixel noise σ_1 measured in count s^{-1} and fit coefficients for background fluctuations using Eq. (5.2)

Filter	σ_1	α	β
ESO872.....	0.00051	1.53	1.32
ESO874.....	0.00079	0.76	1.24
ESO860.....	0.00135	1.76	1.29
ESO862.....	0.00103	1.41	1.31
ESO864.....	0.00169	1.28	1.27
ESO867.....	0.00291	1.25	1.24
ESO869.....	0.00190	1.39	1.23
ESO848.....	0.00131	1.56	1.25
ESO851.....	0.00123	1.21	1.27
ESO853.....	0.00118	1.19	1.28
ESO854.....	0.00156	1.05	1.29

Table II: Medium-Band Image Properties.

Filter	FWHM (arcsec)	5 σ depth AB mag	Zero Point AB mag
ESO872.....	1.66	24.80	22.10
ESO874.....	1.66	24.75	21.67
ESO860.....	1.21	24.67	22.78
ESO862.....	1.19	24.44	22.02
ESO864.....	1.11	24.30	22.14
ESO867.....	1.16	23.94	22.34
ESO869.....	1.09	24.02	21.96
ESO848.....	1.16	23.95	21.74
ESO851.....	1.02	24.08	21.40
ESO853.....	1.07	23.44	20.77
ESO854.....	0.95	23.50	20.86

5.3 Optimal Apertures for Photometry

To performe accurate photometry is very important to consider the varying PSFs between different bands, as identical apertures will not account for the same fraction of light when performing photometry. This might compromise our attempt to construct the most accurate spectral energy distributions of our objects in order to refine the information to be provided for estimating a photometric redshift. These issues are of significance when covering a large wavelength

range, and when the data come from different telescopes (e.g., Cardamone et al. 2010).

The issues concerning the photometry for the study of high redshift galaxies turn even worse when comparing colors of sources at different redshifts. There is a considerable effect that would bias colors due to differences in the regions where a flux is measured for galaxies at different distances if an aperture is defined to ensure a high signal-to-noise ratio. For example, for a fixed aperture, photometry on near galaxies comprehends the central region, excluding any color gradient from the outer parts that would influence the measured flux.

One technique commonly used to overcome the non uniform profiles of the same objects in different bands consists on smoothing all images to the PSF size of the image with the worst seeing. However, it is not convenient to degrade good quality images to a large PSF size, as this decreases the sinal-to-noise ratio. In fact, this adjustment requires a non-Gaussian convolution kernel considering the profile shapes in our images as we will see later. Advantageously, the variations in seeing in our images is not too large when comparing with similar studies.

In this work we adopt a method based on selecting an optimal aperture for every image separately. In each case we selected 30 suitable stars randomnly distribuited to create a set of bright-unsaturated objects which seem to be isolated from other objects. We first analize how the signal behaves with aperture size as shown in Figure 5.4, which allow us to determine the effect of a non-Gaussian PSF for accurate photometry.

For a Gaussian PSF and uncorrelated noise dominated by the sky background, the aperture diameter that optimize the signal-to-noise ratio for a point source is equal to 1.35 times the seeing FWHM (Gawiser et al. 2006). However we can notice in Figure 5.4 that a Gaussian PSF is only a good fit to the core of the generated PSF in each medium-band filter, enclosing $\sim 84\%$ of the total flux of our selected unresolved objects. This Gaussian PSF has the median seeing of our medium-band images, which are better represented by a near-Gaussian extended core with a larger fraction of the flux outside as seen in the right panel of Figure 5.4. This non-Gaussian PSF shape can also be noted when comparing a 1.35$\times$FWHM aperture, which is supposed to enclose $\sim 50\%$ of the flux, with the half-light radii $r_{1/2}$ output determined by SExtractor, which

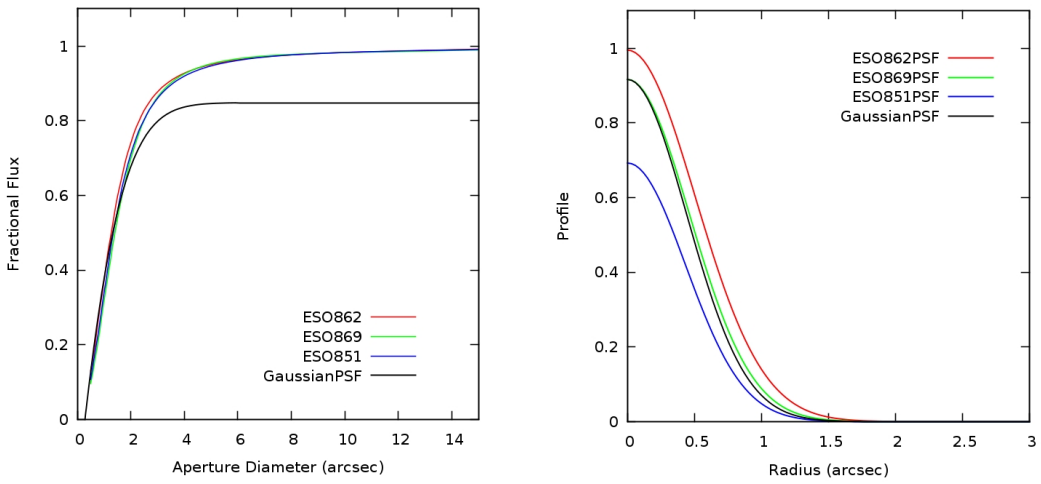

Figure 5.4: Left: Fractional flux averaged over 30 selected bright objects with stellarity above 0.8 according to SExtractor in three different filters. Right: Average Point Spread Functions for the same three medium-band filters. In both panels, the dark curve represent a Gaussian of a median FWHM (left) and 1.19"FWHM (right). A 16" diameter aperture was used to normalize to total flux.

is larger.

As in Gawiser et al. 2006, and considering seeing variations at similar levels with those in our images, we select the optimal apertures in the range where S/N$>$ 95% as the optimal value. Using the same 30 stars mentioned above and the detections performed when analizing background fluctuations, we are able to find a range of apertures satisfying a S/N$>$ 95% for every filter. This allows us to choose those apertures with less variations as possible along filters. In choosing similar apertures for images with similar seeing we reduce the errors when performing photometry on extended sources. The procedure used to select optimal apertures is shown in Figure 5.5, where we trace the behaviour of the signal-to-noise ratio as a function of aperture diameter, along with the enclosed flux and rms background fluctuations. It is quite acceptable to think on an aperture larger than 1.35$\times$FHWM in order to capture more signal when a PSF shows wings broader than those of a Gaussian profile. Since we learned from section 5.2 that noise usually increases with aperture size faster than the Poissonian case, it is no longer correct to adopt an aperture that would increase the noise level and degrades the signal.

The optimal aperture diameters are listed in Table III along with the fractional flux enclosed

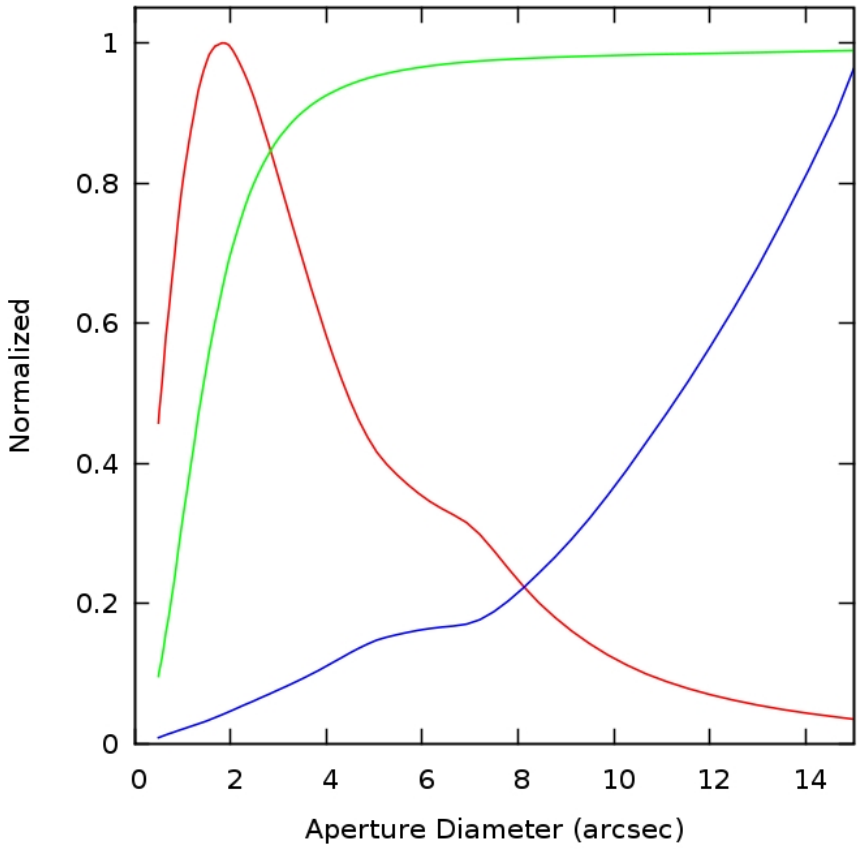

Figure 5.5: Image ESO869: Signal to noise ratio averaged over 30 stars in red, with a S/N$>$ 95% in an interval of $\sim$ $0.8''$ around an aperture of $1.85''$. Averaged fractional flux enclosed by the list of apertures performed in green, where a 16" diameter aperture was used to define the total flux. The blue curve represents the noise as a function of aperture diameter, which is also normalized at 16". For the remaining filters the peak of the S/N curve spans a range smaller than 0.55".

within these apertures, which are used to correct for a total flux in each filter as shown in the next section. This approach seems to be more convenient than using larger apertures, which reduces the signal-to-noise of point source photometry. It is important to mention that the apertures are no longer optimal for extended sources. Thus we will perform some corrections to account for the fraction of flux that is lost when doing photometry with this optimal circular apertures.

Table III: Optimal Apertures for Photometry.

Filter	Optimal Aperture (arcsec)	Enclosed Fractional Flux
ESO872.....	1.65	0.65
ESO874.....	1.90	0.70
ESO860.....	1.65	0.73
ESO862.....	1.65	0.65
ESO864.....	1.65	0.65
ESO867.....	2.15	0.66
ESO869.....	1.90	0.69
ESO848.....	1.65	0.70
ESO851.....	1.65	0.62
ESO853.....	1.90	0.66
ESO854.....	1.65	0.67

5.4 Source Detection and Aperture Photometry

To do photometry, we run SExtractor version 2.4.4 (Bertin & Arnouts 1996) in dual-image mode using the original BVR image for detection, and each final medium-band image as the measurement image. This will allow us to make a common catalog for all filters. However the considerable difference in depths and quality between the BVR composite image and any of our medium-band images will create $\sim 70\%$ of flux detections above 5σ in our filters. For object detection we smoothed the BVR image with the PSF itself using a 7×7 pixel Gaussian convolution kernel. This is explained in Appendix B of Gawiser et al. 2006. We fixed SExtractor parameters common for all medium-band images in the following form: threshold of 1.2σ for analysis and detection, SATUR_LEVEL$= 20.0$, PIXEL_SCALE$= 0.238$, BACK_SIZE$= 64$ and BACK_FILTERSIZE$= 3$. PHOT_APERTURES, MAG_ZEROPOINT, GAIN (GAIN×EXP_TIME) and SEEING_FWHM parameters vary from filter to filter. Using these parameters we detected about 64000 objects in the BVR image, and an average of ~ 58000 reliable non-negative measurements in the medium-band images

SExtractor offers different estimates for the photometry. The SExtractor's AUTO aperture uses a Kron-like (Kron 1980) elliptical aperture which is adapted to each object's light profile

to compute fluxes and has been used in many other works. It measures $\simeq 94\%$ of the flux for extended sources and $\simeq 97\%$ for point sources (Bertin & Arnouts 1996), making an acceptable choice to handle both extended and unresolved sources. However it may be affected by variations in the total fraction of flux detected for different filters. Consequently, we adopt the user-defined aperture fluxes (FLUX_APER) using the optimal apertures for point sources determined in Section 5.3.

In order to address the challenge of making an appropiate correction for extended sources, we will find a more accurate estimate for the flux enclosed than that given by the "optimal" apertures listed in Table III. We use the half-light radius $r_{1/2}$ (FLUX_RADIUS) of each object as determined by SExtractor in the MUSYC BVR image. This selection is based on the depth of the image to guarantee the most accurate measurement of the object size convolved with the seeing of the image. For each object we assume a two-dimensional Gaussian profile with a FWHM twice the value of $r_{1/2}$, giving a good robust estimate of the light profile for each object separately. Using the median half-light radii of point sources in the BVR image (or in terms of its standard deviation: $\sigma = \mathrm{FWHM}/2\sqrt{2\ln 2} = r_{1/2}/\sqrt{2\ln 2}$), we are allowed to deconvolve our two-dimensional source Gaussian profile from the image Point Spread Function (PSF) to determine its intrinsic size. This can in turn be convolved with a new Gaussian profile with twice the median half-light radius of point sources for each filter. This final profile represents a more accurate distribution for extended objects. Considering that the convolution of two Gaussians is another Gaussian, the profile that better represents the light distribution of an extended object i in filter j is expected to be characterized by

$$A\exp\left(\frac{-r_{\mathrm{ap},j}^2/2}{\sigma_i^2+\sigma_j^2-\sigma_{BVR}^2}\right) \ , \tag{5.3}$$

where A is a constant and the denominator is the root mean square, which is the sum determined from the standard deviation of object i detected in the BVR image, the median standard deviation in filter j and BVR for point sources, respectively. The median half-light radii values, provided from SExtractor, are listed in Table IV. By integrating the two-dimensional Gaussian

profile, for each object, we can find an expression to determine the fractional flux enclosed by the optimal aperture radius which we performed photometry with, yielding

$$\text{frac} = 1 - \exp\left(\frac{-r_{\text{ap},j}^2/2}{\sigma_i^2 + \sigma_j^2 - \sigma_{BVR}^2}\right) . \tag{5.4}$$

Table IV: Median Half-Light Radii for Medium-Band Images.

Filter	SE $r_{1/2}$ Median (arcsec)
BVR	0.59
ESO872.....	0.84
ESO874.....	0.87
ESO860.....	0.77
ESO862.....	0.74
ESO864.....	0.69
ESO867.....	0.79
ESO869.....	0.77
ESO848.....	0.59
ESO851.....	0.60
ESO853.....	0.63
ESO854.....	0.56

We can note from Table IV that the diameters based on the half-light radii output by SExtractor are sistematically larger than the FWHM as object profiles are better characterized by the Moffat PSF shapes allowed by IRAF. Moreover they are very close to values determined for circular optimal apertures. We make the final correction for fluxes measured in the optimal apertures using the minimum between the value calculated for *frac* from equation 5.4 and the fractional fluxes enclosed for point sources reported in Table IV. In this way point sources with under-represented sizes, as determined by $r_{1/2}$ due to noisy data, have a more accurate flux determination.

5.5 Photometric Errors & Fluxes

We estimate flux uncertainties considering correlated background noise for each object in each band as

$$\sigma^2_{\text{phot}} = \sigma^2_1 \alpha^2 N^{\beta}_{\text{pix}} + \frac{F}{\text{GAIN}} \ , \tag{5.5}$$

where the first term is determined using the values obtained in section 5.2 and listed in Table I and F is the object flux given by SExtractor in counts within the aperture. Finally we set our photometric measurements in units of flux density in μJy by determining flux zero points using the formula

$$f_\nu(\mu Jy) = \left(3.631 \times 10^9\right) 10^{-0.4 m_{\text{AB}}} \ , \tag{5.6}$$

where m_{AB} are the final magnitud zero points which correspond to the zeropoints determined for the calibration images but corrected to the final stacked images. To achieve this, we chose a set of stars with well defined fluxes in every filter to performe aperture photometry. We determine magnitudes for both the calibration and stacked image, and based in the differences relative to images we performed the correction for each. These magnitude zero points are reported in Table V along with their corresponding flux zero points calculated from equation 5.6 to turn count s^{-1} into μJy. Additionally in the case of uncertainties, we also convert from counts s^{-1} to fluxes using these zero points. A further increase in its value is performed by multiplying the square of the ratio between the flux enclosed by point and extended sources as an extra contribution in case of extended sources that have an amplified uncertainty.

5.6 The Photometric Catalog

Our photometric catalog contains ~ 62000 objects in the Hubble Deep Field South in 11 medium-bands images and 6 broad-bands from MUSYC published in Gawiser et al. 2006. It contains celestial coordinates, positions, and shape parameteres, such as stellarity, are measured from the final BVR image. The information in each column of the catalog is clearly described

Table V: Magnitude and Flux Zero Points.

Filter	Zero Point AB mag at 1 count s^{-1}	Flux Zero Point μJy/(count s^{-1})
ESO872.....	21.86	6.547
ESO874.....	21.62	8.166
ESO860.....	22.79	6.983
ESO862.....	22.00	5.755
ESO864.....	22.00	5.755
ESO867.....	22.25	4.571
ESO869.....	21.83	6.730
ESO848.....	21.59	8.395
ESO851.....	21.31	10.865
ESO853.....	20.59	21.088
ESO854.....	20.83	16.905

in Table VI. The catalog also includes the spectroscopic redshift if available, together with the photometric redshift estimates for all the objects with $R_{\rm AB} < 24$. The issues concerning the determination of photometric redshifts are discussed in chapter 7.

Table VI: Summary of the Photometric Medium-Band Optimal Source Catalog.

Column No.	Units/Title	Description
1	-/Num	Sequential Object Identifier from 0
2	-/Name	Object name as in MUSYC (1)
3	h/RAh	Hour of Right Ascension (J2000) (1)
4	deg/DEdeg	Declination in decimal degrees (J2000 (1))
5	pix/Xpix	The X position barycenter (1)
6	pix/Ypix	The Y position barycenter (1)
7	-/Class	Stellarity classification (1)
8	μJy/Uapcorr	The U band APCORR flux from MUSYC (1)
9	μJy/e_Uapcorr	Uncertainty in Uflux from MUSYC (1)
10	μJy/ESO872apcorr	The ESO872 band APCORR flux (2)
11	μJy/e_ESO872apcorr	Uncertainty in ESO872flux from Equ. 11 (3)
12	μJy/Bapcorr	The B band APCORR flux from MUSYC (1)
13	μJy/e_Bapcorr	Uncertainty in Bflux from MUSYC(1)
14	μJy/ESO874apcorr	The ESO874 band APCORR flux (2)
15	μJy/e_ESO874apcorr	Uncertainty in ESO874flux from Equ. 11 (3)
16	μJy/ESO860apcorr	The ESO860 band APCORR flux (2)
17	μJy/e_ESO860apcorr	Uncertainty in ESO860flux from Equ. 11 (3)
18	μJy/ESO862apcorr	The ESO862 band APCORR flux (2)
19	μJy/e_ESO862apcorr	Uncertainty in ESO862flux from Equ. 11 (3)
20	μJy/Vapcorr	The V band APCORR flux from MUSYC (1)
21	μJy/e_Vapcorr	Uncertainty in Vflux from MUSYC (1)
22	μJy/ESO864apcorr	The ESO864 band APCORR flux (2)
23	μJy/e_ESO864apcorr	Uncertainty in ESO864flux from Equ. 11 (3)
24	μJy/ESO867apcorr	The ESO867 band APCORR flux (2)
25	μJy/e_ESO867apcorr	Uncertainty in ESO867flux from Equ. 11 (3)
26	μJy/Rapcorr	The R band APCORR flux from MUSYC (1)
27	μJy/e_Rapcorr	Uncertainty in Rflux from MUSYC (1)
28	μJy/ESO869apcorr	The ESO869 band APCORR flux (2)
29	μJy/e_ESO869apcorr	Uncertainty in ESO869flux from Equ. 11 (3)
30	μJy/ESO848apcorr	The ESO848 band APCORR flux (2)
31	μJy/e_ESO848apcorr	Uncertainty in ESO848flux from Equ. 11 (3)
32	μJy/Iapcorr	The I band APCORR flux from MUSYC (1)
33	μJy/e_Iapcorr	Uncertainty in Iflux from MUSYC (1)
34	μJy/ESO851apcorr	The ESO851 band APCORR flux (2)
35	μJy/e_ESO851apcorr	Uncertainty in ESO851flux from Equ. 11 (3)
36	μJy/ESO853apcorr	The ESO853 band APCORR flux (2)
37	μJy/e_ESO853apcorr	Uncertainty in ESO853flux from Equ. 11 (3)
38	μJy/zapcorr	The z' band APCORR flux from MUSYC (1)
39	μJy/e_zapcorr	Uncertainty in zflux from MUSYC (1)
40	μJy/ESO854apcorr	The ESO854 band APCORR flux (2)
41	μJy/e_ESO854apcorr	Uncertainty in ESO854flux from Equ. 11 (3)
42	PhotZ	Photometric Redshift
43	SpecZ	Spectroscopic Redshift

Note (1): Parameters obtained from Gawiser et al. 2006.

Note (2): After dividing by the minimum between *frac* from equation 5.4 and fractional fluxes reported in Table IV.

Note (3): After correction by additional factors to consider the amplified error for extended sources.

Chapter 6

Classification

6.1 Star/Galaxy Separation

The developement of wide-deep surveys that aim to study galaxy formation and evolution, requires a reliable identification of stars and galaxies to determine which objects we might be confronted with. Typically the deep imaging of these high latitude fields are expected to have galaxies as the most abundant objects. Stars are the second-most common objects, representing about one tenth the number of galaxies for $R < 24$ depending on the coordinates of the field (Metcalfe et al. 1995; Bahcall & Soneira 1981). Most stars should be late-type main sequence stars, and only a few should be of other type, such as white dwarfs, giants, T-L dwarfs, etc. Active galaxies characterized by broad-line emission spectra are supposed to be the third-most abundant objects. Therefore a detail classification of objects into stars, galaxies and quasars must be performed in order to identify more than 99% of the members in our photometric catalog.

There are several techniques to make a stellar classification. SExtractor offers a classification through the CLASS_STAR parameter, which separates objects into stars and galaxies by analysing the profiles of each object; a stellarity parameter larger than 0.8 implies an unresolved profile, while cases with a stellarity smaller than 0.3 point to extended profiles. Stellarity val-

ues in the interval 0.3 <CLASS_STAR< 0.8 represent uncertain objects. Figure 6.1 shows the SExtractor stellarity classification for objects in our catalog. It can be seen that the SExtractor CLASS_STAR parameter does not give a reliable stellar classification for dimmer objects than $R \geq 25$, where the stellarity falls mostly in the uncertain regime and becomes nearly useless. On the other hand, brighter objects clearly split between stellar and extended profiles.

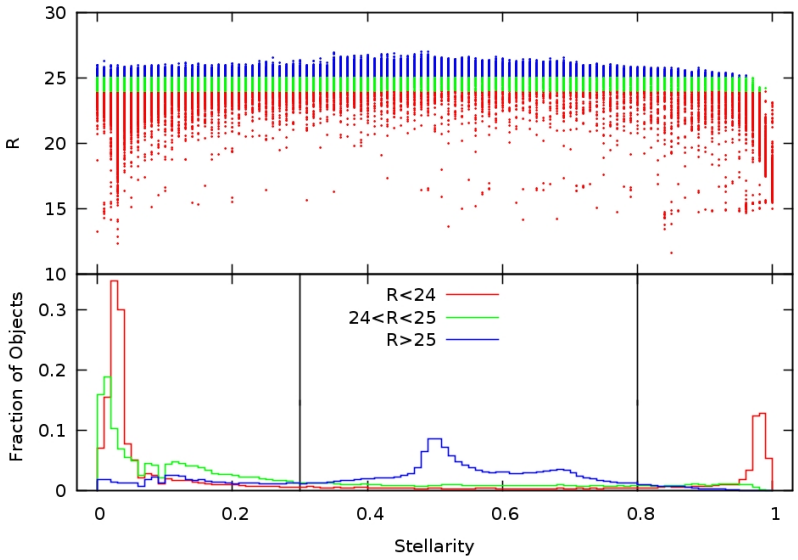

Figure 6.1: SExtractor stellarity for the ~ 60000 objects in our catalog. The classification is distributed versus total R-band AB magnitude (top) and versus the fraction of objects for the three chosen magnitude ranges (bottom). The top panel shows an agglomeration of objects pointing to the uncertain regime, while in the lower magnitude range this effect is noticeable towards the extreme values in stellarity, which represent unresolved (CLASS_STAR> 0.8) and extended profiles (CLASS_STAR< 0.3). The bottom panel shows a more explicit relation of the fraction of objects according to the apparent profiles when separating through vertical solid lines galaxies, uncertain objects, and stars, for the selected magnitude ranges.

Quadri et al. 2007 adopted a method based on fitting the NextGen stellar atmospheres models (Hauschildt et al. 1999) to identify stars, due to the unfortunate presence of objects with a high stellarity parameter in the NIR images, which contrary show extended profiles in the optical bands. Other works have performed similar techniques fitting template spectra for specific morphological types of objects (i.e. Ilbert et al. 2009; Cardamone et al. 2010). For each object, they evaluate a χ^2 value for both the galaxy templates and a set of stellar templates, reaching agreement identifications for more than $\sim 80\%$ of the stellar objects when comparing

with $Bz'K$ color selection techniques or morphological classifications.

We perform a double selection method based on the fitting of stellar Spectral Energy Distribution (SED) templates, and the stellarity parameter. We use the stellar SED template library of Pickles 1998 to identify stars, which consists of 131 flux-calibrated spectra, spaning from O to M spectral types, all luminosity classes, and a large variety in metal richness. These stellar templates can be compared statistically to our broad- and medium- band data all together, as they have a spectral coverage from 1150 to 10620 $\AA$, increasing to 25000 $\AA$ for about half of them. Therefore we evaluate a $\chi^2_{\rm star}$ when fitting every object to each of the stellar SED templates, and compare this to a $\chi^2_{\rm gal}$ using six galaxy templates separately, that made up the galactic templates of the photometric redshift code we will use later. If $\chi^2_{\rm gal} - \chi^2_{\rm star} > 0$, the object is flagged as a possible star.

To test the accuracy of our classification of stars we also build a BzK color-color diagram using the $(B-z)_{\rm AB}$-$(z-K)_{\rm AB}$ colors, in the region where infrared JHK data are available in the HDFS. This color criteria was introduced by Daddi et al. 2004, and it was developed using a different set of filters than the ones used in this work. Thus we apply the offsets determined by Blanc et al. 2008 of -0.04 mag in $(z-K)_{\rm AB}$ and 0.56 mag in $(B-z)_{\rm AB}$. This method allows to identify galaxies at $z > 1.4$ and separate all galaxies from a stellar sequence confined by the colors $(z-K)_{\rm AB} \leq 0.3(B-z)_{\rm AB} - 0.5$ as shown in Figure 6.2. The precision to identify stars by this approach has proven to be very effective ($> 90\%$; e.g. Daddi et al. 2004; Blanc et al. 2008; Taylor et al. 2009). The stars identified through fitting stellar SED templates are represented by blue squares, and agree up to 91.6% with those lying in the stellar sequence of the BzK color-color diagram, in good agreement with the previous results.

According to the stellar SED identifications, which we have proved to be very effective, we sub-divide the stellar classification into three groups: (1) Those with $\chi^2_{\rm gal} - \chi^2_{\rm star} > 0$, $R < 24.5$ and CLASS_STAR> 0.8, as reliable stellar objects; (2) Cases with $\chi^2_{\rm gal} - \chi^2_{\rm star} > 0$, $R < 24.5$ and $0.3 <$CLASS_STAR< 0.8, as very good stellar object candidates; and (3) $\chi^2_{\rm gal} - \chi^2_{\rm star} > 0$, with $\chi^2_{\rm star}$ having a probability in a chi-square distribution being regarded as statistically significant,

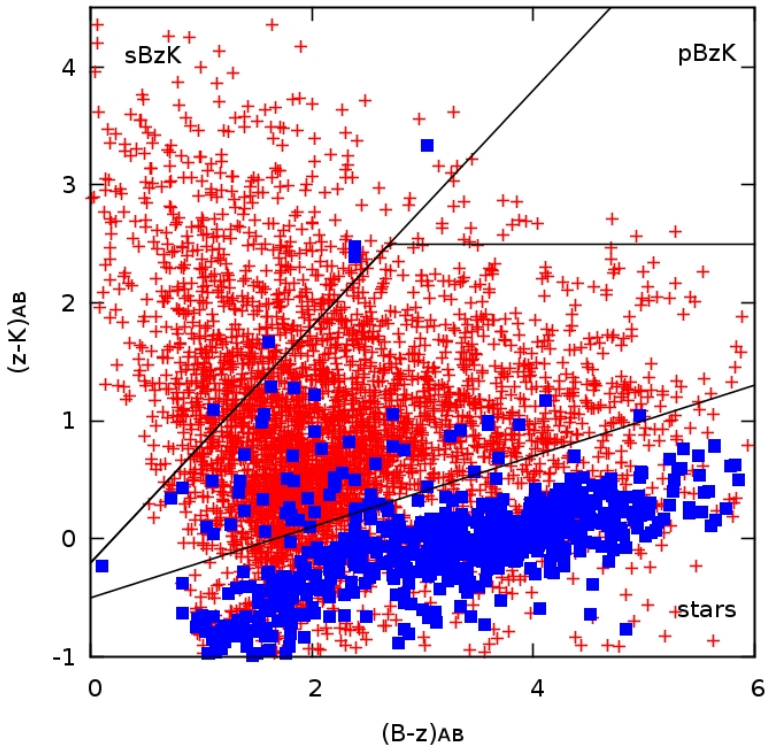

Figure 6.2: BzK color-color diagram used by Daddi et al. 2004. The three regions identified are used to separate star-forming galaxies and passive galaxies at $z \geq 1.4$, and stars. Filled blue squares represent stars selected by fitting stellar SED templates.

$R > 24.5$ and CLASS_STAR> 0.3, as potential stellar object candidates. We fixed $R < 24.5$ in order to take into account only objects that are well identified as stars or galaxies in most cases, according to the SExtractor CLASS_STAR parameter. In the first case we believe the classification is more than 95% accurate, as we incorpore two independent criteria. The second case is a less certain regime where $\sim 80\%$ of stars can be identified. The third case is even less reliable as high redshift galaxies which look like point sources might have star-like SEDs, and also considering that any method loses ability to separate stars from galaxies at fainter magnitudes. This also becomes uncertain as CLASS_STAR> 0.3, corresponds to a region that includes many ambigous cases when $R > 24.5$.

Finally the objects are distributed by this three fold identification as shown in Figure 6.3. We classified about 9.5% and 1.5% objects as stars in our catalog, by methods (1) and (2) respectively when $R < 24.5$, and about 3.5% by method (3) when $R > 24.5$. The resulting

classification by method (1) shows very clearly that the SExtractor CLASS_STAR> 0.8 parameter does not give a reliable classification for stars, getting worse with increasing magnitudes. As a fitting stellar SED approach is included, the number of star candidates is reduced by a factor of 2. This number is reduced even more for the other two cases. We identify only a few percent of star-like objects by method (2). This is not surprising as we are examining the uncertain regime where all objects have $0.3 <$CLASS_STAR< 0.8. Method (3) only allows us to classify a very small number of stars due the very restricted conditions performed in pursue of an accurate estimate. Spectroscopic follow up clears this up very effectively.

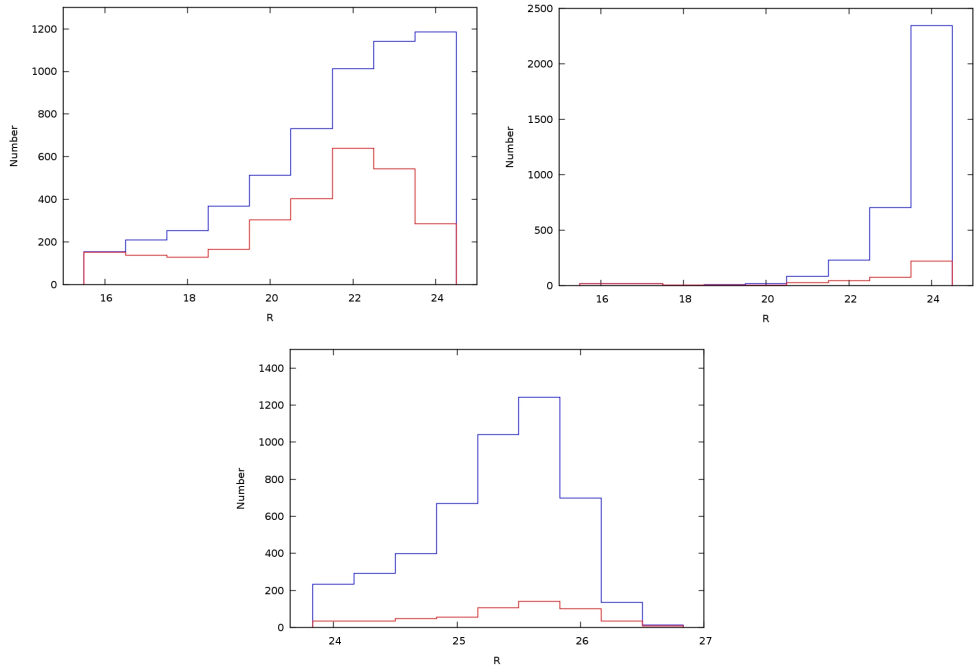

Figure 6.3: Distribution of star candidates through methods (1), (2), and (3), ranging from left to right respectively. The blue bar distribution represent the star classification using the CLASS_STAR criteria, while the red bar distribution is found when the fitting stellar SED classification is included.

In summary we have identified 3668 stars by methods (1), (2), and (3) in our photometric catalog, which represents about 6% of the whole sample. These sources will be tagged in the published catalog including the classification method with the method number in order to identify how precise is the nature of the object. For the rest of this work, we discard all the star-like objects as our study focuses on galaxies.

6.2 Number Counts

In order to verify the quality of our medium-band, we determine the differential number counts for all galaxies in our filters in the HDFS. The results are presented in Figure 6.4 together with the corresponding medium-band data from the COMBO-17 survey (Section 4.4). We exclude objects classified as stars according to the procedure outlined in the last section. The number counts are calculated in 0.3 AB magnitude bins. It is clearly a good agreement when comparing to COMBO-17. The reason for the absence of galaxies in some regions at faint magnitudes is not quite clear, and cannot be related to the dimensions of the fields in comparison, since they have areas large enough to overcome the problem of cosmic variance. At bright magnitudes differences are mostly related to the small number of objects and the presence of some stars that could not be filtered out in any of both surveys. Furthermore, we do have large differences in depth to affect notoriously the number counts cause our medium-band images are characterized, in some bands, by similar depths in comparison with their counterparts of COMBO-17 in most filters. There are some other factors that may explain inconsistencies at faint magnitudes, such as seeing conditions, stack image procedures, sky substraction, and parameter values set for SExtractor. Since most of our study is based on reliable photometric redshifts, which belong to objects with $R < 24$, we are not really concerned with discrepancies at very faint levels when comparing both survey medium-band number counts.

There is evidence of a consistent higher density of objects at faint magnitudes, and a lower density at bright magnitudes for COMBO-17 along filters. Other studies have shown galaxy overdensities at different redshift ranges which affect a reliable comparison. Moreover medium bands are more affected by lower S/N than broad bands, which represent a significant effect that explain disagreements when comparing number count s among different surveys.

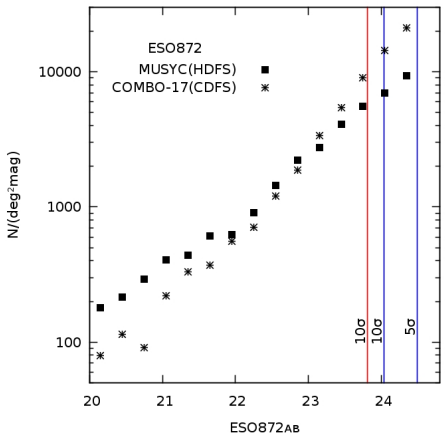
ESO872
MUSYC(HDFS)
COMBO-17(CDFS)
N/(deg²mag)
ESO872AB
10σ
10σ
5σ

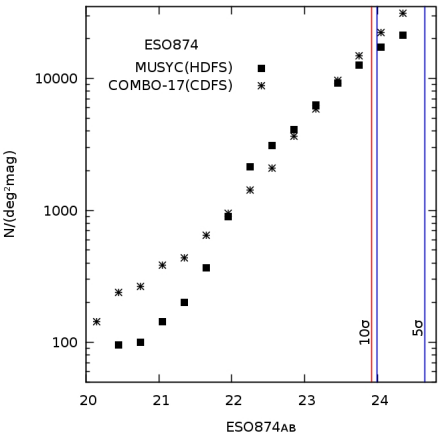
ESO874
MUSYC(HDFS)
COMBO-17(CDFS)
N/(deg²mag)
ESO874AB
10σ
5σ

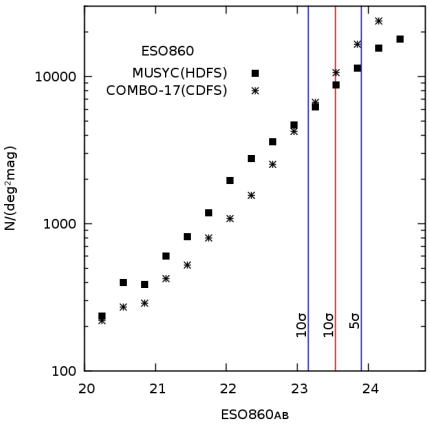
ESO860
MUSYC(HDFS)
COMBO-17(CDFS)
N/(deg²mag)
ESO860AB
10σ
10σ
5σ

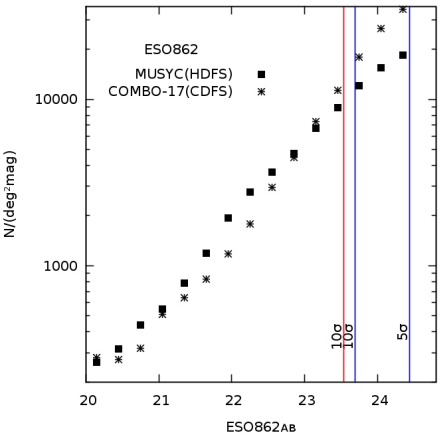
ESO862
MUSYC(HDFS)
COMBO-17(CDFS)
N/(deg²mag)
ESO862AB
10σ
10σ
5σ

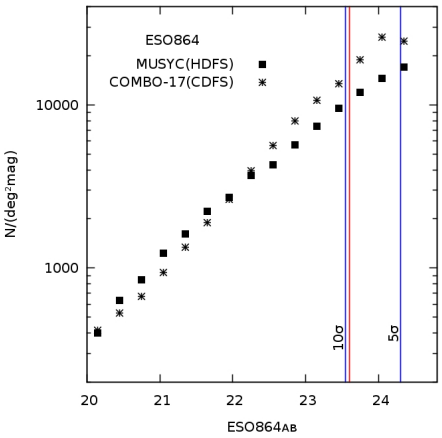
ESO864
MUSYC(HDFS)
COMBO-17(CDFS)
N/(deg²mag)
ESO864AB
10σ
5σ

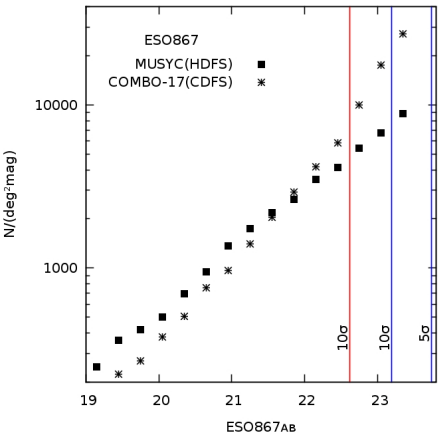
ESO867
MUSYC(HDFS)
COMBO-17(CDFS)
N/(deg²mag)
ESO867AB
10σ
10σ
5σ

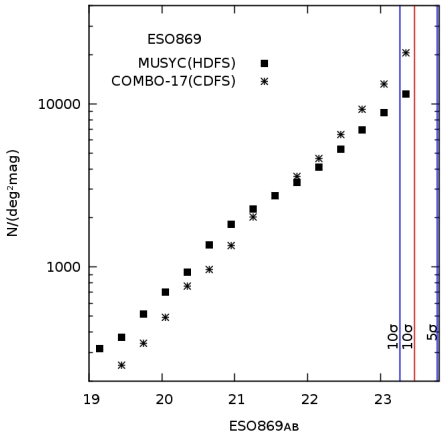
ESO869
MUSYC(HDFS)
COMBO-17(CDFS)
N/(deg²mag)
ESO869AB
10σ
10σ
5σ

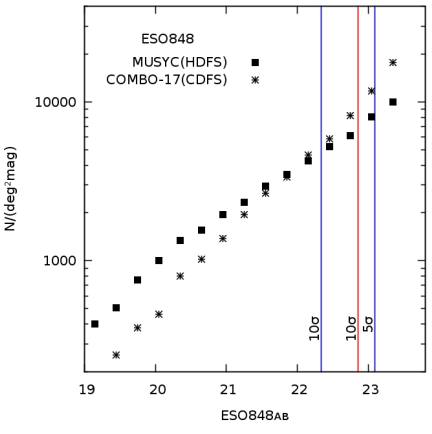
ESO848
MUSYC(HDFS)
COMBO-17(CDFS)
N/(deg²mag)
ESO848AB
10σ
10σ
5σ

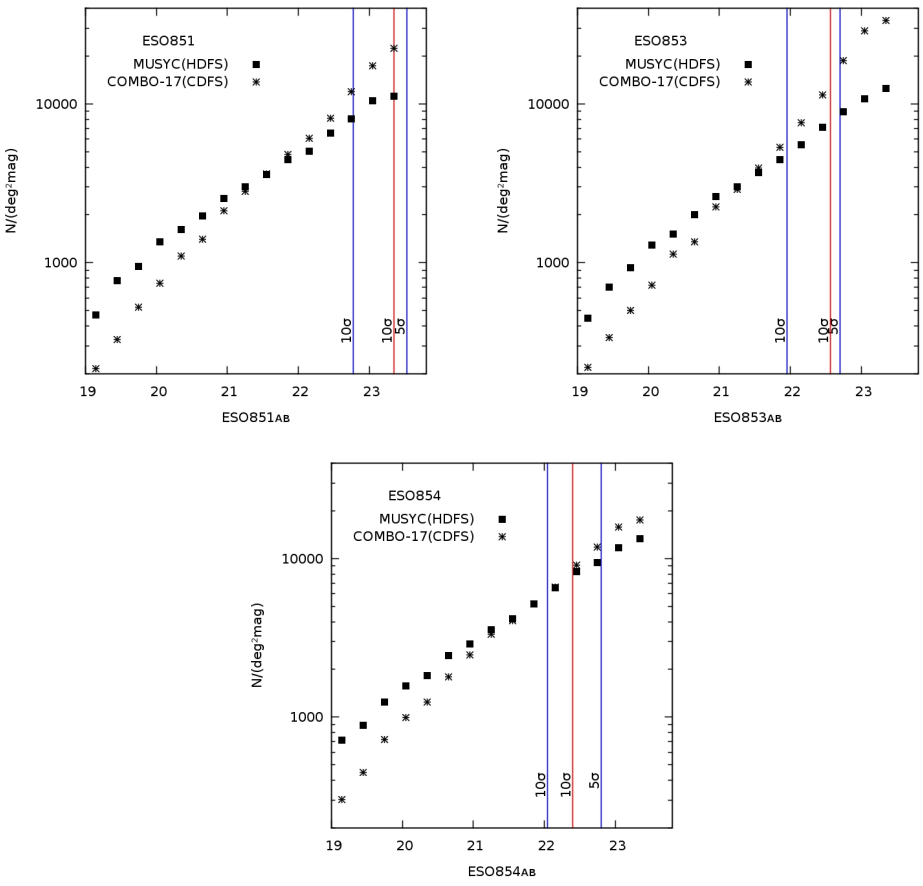

Figure 6.4: Medium band number counts in the HDFS for MUSYC (squares) and for COMBO-17 (crosses) excluding objects classified as stars.

Chapter 7

Redshifts

The development of observational cosmology is strongly connected with the availability of accurate redshifts of distant galaxies, covering a range of morphology types as broad as possible. Presently we benefit from having hundred of thousands computed redshifts of galaxies, courtesy of multiobject spectrographs on 8-10 m class telescopes, which are already published (e.g., Steidel et al. 2003; Davis et al. 2003; Le Fèvre et al. 2005). However these spectroscopic calibration samples are highly biased against or incomplete for galaxies fainter than $R \sim 24$. To illustrate this a L^* galaxy will have $m \sim 24$ at $z \sim 1.5$.

Nonetheless we can rely on photo-z for fainter galaxies, which significantly improved completeness down to a very faint flux limit. These photo-zs are derived from the fitting of galaxy template spectra to broad- or medium-band photometry, and the quality of photo-zs depends on the availability of intrinsic spectral features, spectral coverage, and resolution. By reaching an accuracy of $\Delta z/(1+z_s) \sim 0.02 - 0.04$ we are allowed, to study the evolution of galaxy stellar masses and luminosities as well as the relations between galaxy properties and environment. In this section we assess the computation of phot-zs, and their accuracy by comparison with high-confidence spec-zs. We describe both methods in detail and compare our results with recent works.

7.1 EAZY(E$_{\text{asy and}}$ A$_{\text{ccurate}}$ Z$_{\text{(photometric redshifts) from}}$ Y$_{\text{ale}}$)

EAzY is a public photometric redshift code[1] designed to derive high-quality photo-z over $0 \leq z \leq 4$, where complete spectroscopic calibration samples are not available (Brammer et al. 2008) due to divergent survey selection criteria. The code combines features from various existing codes by fitting linear combinations of templates, including optional flux and redshift priors (e.g., BPZ; Benítez 1999), and it has a structure interface similiar to the HYPERZ code (Bolzonella et al. 2000). Many codes perform this template-fitting procedure interpreting the residuals from a χ^2 minimization, using Monte Carlo methods or Bayesian statistics. The innovation of EAzY is that the default set of 6 templates (Figure 7.1), carefully selected and optimized for optical-NIR surveys, and the forms of magnitude priors, are not based on spectroscopic samples, that are usually highly biased. Instead, they are based on semianalytical models which are significantly improved to a completeness down to a flux limit much fainter than the spectroscopic limit. The derivation of the optimized set of 6 templates was chosen to be large enough that it spans the broad range of multiband galaxy colors and small enough that the color and redshift degeneracies are kept to a minimum. This significant improvement on selecting the template set increase the quality of photometric redshift estimates. Most other frequently used templates in recent photo-z codes are determined from local galaxies or have limited wavelength coverage. EAZY templates are derived as follows:

- For the input list of N_{in} models to the BR07 algorithm, EAZY uses the library of PÉGASE models (Fioc & Rocca-Volmerange 1997), which includes $N_{\text{in}} \sim 3000$ models with ages between 1 Myr and 20 Gyr, and different star formation histories.

- EAZY obtain synthetic $UBVRIzJHK$ phtometry of a subsample of 10^4 galaxies with $K_{\text{AB}} < 25$ from a 1 deg^2 light cone (Blaizot et al. 2005) created in the semianalytic model (SAM) of De Lucia & Blaizot 2007, which is based on the Millennium Simulation (Springel 2005).

[1] Please visit http://www.astro.yale.edu/eazy/

- The Blanton & Roweis 2007 (BR07) "nonnegative matrix factorization" (NMF) algorithm is used to calculate an optimized template set from a large number, N_{in}, of synthetic models, to create a reduced set of N_{out} basis templates.

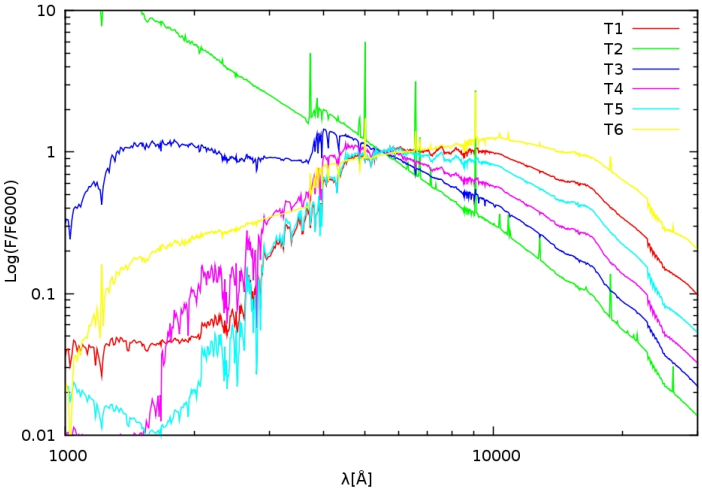

Figure 7.1: Five EAZY templates calculated from the library of PÉGASE models following the Blanton & Roweis 2007 (BR07) algorithm along with a calibration set of synthetic photometry derived from semianalytic models. Shown in yellow is the added dusty starburst model to compensate for the lack of extremely dusty galaxies in the SAMs. Templates are normalized at 6000$\mathring{A}$.

The PÉGASE models have the advantage of having additional reddening $[0.5 \leq E(B-V) \leq 1.1]$ to represent young, dusty objects, and they provide a self-consistent treatment of emission lines. Although there are PÉGASE models with significant dust absorption, the dust treatment in the SAM is unable to produce extremely dusty galaxies. Therefore a dusty starburst model ($t = 50$ Myr, $A_V = 2.75$) was added to the $N_{\text{out}} = 5$ EAZY templates computed from the NMF algorithm. These 6 final templates are shown in Figure 7.1.

For a given galaxy spectrum, colors oscillate with redshift as filters sample different distributions of energies. As the use of medium-band width filters provides better resolution than broad-band imaging, we expect more noticeable variations for medium-band than broad-band filters due the presence of emission lines, causing up to 0.4 mag changes in the colors (Ilbert et al. 2009). Consequently, EAzY has recently been implemented to account for the contribution of strong narrow emission lines to the spectral energy distributions. Emission line fluxes have been modelled for each template at different redshifts, estimating an [O_{II}] emission line

flux from the stellar UV luminosity of the scaled template, and fixing line ratios for [O_{III}/O_{II}], [Hβ/O_{II}], and [Hα/O_{II}].

The algorithm finds the best-fitting synthetic template spectrum from a user-defined grid of redshifts by minimizing

$$\chi^2_{z,T} = \sum_{f=1}^{N_{\rm filt}} \frac{\left(F_{\rm pred}(T,z,f) - F_{\rm obs}(f)\right)^2}{\left(\delta F(f)\right)^2} \ , \tag{7.1}$$

where $N_{\rm filt}$ is the number of filters, $F_{\rm pred}(T,z,f)$ is the synthetic flux of template T in filter f for redshift z, $F_{\rm obs}(f)$ is the observed flux in filter f and $\delta F(f)$ is the uncertainty in $F_{\rm obs}(f)$. As the fiting-template is carry out as a linear combination, this allows a proper treatment of flux errors and of negative fluxes. It also avoids a template mismatch as a source of errors in photo-z when galaxies are not well represented by any individual template. Rather than finding the best-fitting template, the code finds the best linear combination of two or more templates by weighting template T for redshift z through positive coefficients as

$$F_{\rm pred}(z) = \sum_{f=1}^{N_{\rm temp}} \alpha_f F_{\rm pred}(T,z) \ , \tag{7.2}$$

where $\alpha_f \geq 0$. The program allows a simultaneous fit of one, two, or all of the templates from a user-defined list.

The code also incorporates important features such as a template error function to account for wavelength-dependent template mismatch, and a photometric redshift quality parameter Q_z, which represents a statistical estimate based on the χ^2 of the fitting procedure and the width of the 68% confidence interval. The larger its value the worse the estimate, making a rough assessment of the reliability in the photo-z. The Q_z parameter that gives a robustness of a redshift is defined as

$$Q_z = \frac{\chi^2}{N_{\rm filt} - 3} \frac{z_{\rm up} - z_{\rm low}}{p_{\Delta z=0.2}} \ , \tag{7.3}$$

where $z_{\rm up}$ and $z_{\rm low}$ are the upper and lower confidence limits in the probability distribution of redshifts, and $p_{\Delta z=0.2}$ is a parameter that represents the fraction of the total integrated probability that lies within $\pm\Delta z$ of the $z_{\rm phot}$ estimate. Cardamone et al. 2010 recommend to adopt a conservative cut of $Q_z \leq 1$. Not surprisingly values of Q_z are a strong function of magnitude, e.g. $\sim 80\%$ of good quality photometric redshifts ($Q_z \leq 1$) can be found at $R_{\rm AB} \leq 24$, while only 31% of a sample have $Q_z \leq 1$ in the magnitude range $25 < R_{\rm AB} < 26$ (C. Cardamone et al. (2010)).

7.2 Spectroscopic Redshifts

The HDFS has about 500 spectroscopic redshifts available in the literature from a variety of surveys. According to the selection criteria of sources for each survey, these redshifts present a large variety of qualities. The main factors of these discrepancies come from the number of spectral lines, which are relevant features to be sampled by spectrographs and the data quality. Table III lists the references we used to obtain spectroscopic redshifts, the number of accesible sources in each data set, and the range covered in redshift. Sawicki & Mallén-Ornelas 2003 select targets to be at $z < 1$ to describe their basic properties; Franceschini et al. 2003 present infrared spectroscopic analysis of faint 15μm sources; Rigopoulou et al. 2005 present low resolution-multiobject spectroscopy of a sample dominated by starburst galaxies to confirm the steep rise in the star formation rate at $z \simeq 1.3$; Glazebrook et al. 2006 selected targets from deep Anglo-Australian Telescope prime-focus images, in order to demonstrate the first use of the nod-and-shuffle technique with a classical multiobject spectrograph, and to test the use of microslist for ultrahigh multiplex observations; Wuyts et al. 2009 present optical spectroscopic of a sample of distant red galaxies selected by $(J-K)_{\rm Vega} > 2.3$. 2dF and MUSYC surveys have both a large number of spectroscopic redshifts at $z \leq 1.56$ and $z \geq 2.56$ respectively for a wide variety of sources. The data sets are not described in detail unless necessary. There are 15 sources with multiple published spectroscopic redshifts, from which we choose those with a higher quality flag if available.

Table I: Spectroscopic Data.

References	No. of Sources	Redshift Range ($z_{\rm min} - z_{\rm max}$)
Sawicki & Mallén-Ornelas 2003	103	0.099-0.853
Franceschini et al. 2003	20	0.170-1.520
Rigopoulou et al. 2005	55	0.290-1.390
Glazebrook et al. 2006	72	0.0-1.268
Wuyts et al. 2009	19	0.439-3.385
2dF	95	0.055-1.560
MUSYC 2007	120	0.0-2.560

7.3 Photometric Redshifts

We compute photometric redshifts for different groups of objects according to their magnitudes, excluding those sources classified as stars in Chapter 6. When using medium-bands and broad-bands all together, we limit the photo-z estimates to those objects with $R_{\rm AB} < 24$. The reason for this choice comes from the criteria adopted by Wolf et al. 2004, which concluded that photo-zs for COMBO-17 are more reliable at $R < 24$. As we are using almost the same set of filters with comparable depths in our medium-bands, we decide to follow their approach for comparison purposes. In general medium-band surveys with similar exposure time per filter are less deep than broad-band surveys. The depth that MUSYC reaches in their broad-bands is larger than medium-bands for all bands.

In what follows photo-z estimates are determined for over 35% of our BVR sources with $R < 24$ when medium- and broad- bands are in use. About 50% of the sources with $R > 24$ are evaluated using only broad-bands. The remaining 15% of sources in our catalog are classified as stars, have fewer than five filters with non-negative detections, or do not follow a conservative requirement of $Q_z \leq 1$ to ensure good quality of photo-zs.

When running EAzY to compute photometric redshifts, we first use the 11 medium-bands in combination with the 6 available broad-bands. We keep most of the default parameters provided by EAzY, such as: SMOOTH_FILTERS=y to smooth the filter curves with a Gaussian profile; TEMPLATE_COMBOS set to a, allowing all template combinations simultaneously;

APPLY_IGM=y, to apply Madau 1995 IGM absorption; APPLY_PRIOR and PRIOR_FILE set in order to adopt the default template error function and R-band photometric prior. Example SEDs are shown in Figure 7.2.

7.3.1 The Performance of Medium-Band Filters

The photo-z estimates are more accurate as more bands are included in the SED fitting procedure. Moreover if those bands sample a narrower wavelength region, the spectrum resolution increases as they provide more accurate information within that region when broad lines are present in the spectrum of the object. Medium-band filters also are more efficient in sampling strong continuum features in the observed wavelength region such as Lyman or Balmer breaks. Figures 7.3, 7.4, and 7.8 show three examples on the improvement on photo-z estimates when medium-band filters are added to broad-band information. In these cases medium bands contribute with additional information about the presence of breaks in the best template construction. When adding medium-band filters it is also possible to find a combination of templates that make a better tracing of the continuum shape by rejecting some very week emission lines as seen in Figure 7.3, constructing a spectrum with a very different nature.

Besides tightening the accuracy, medium-band filters help to alleviate the well known catastrophic failure problem as shown in Figures 7.4 and 7.8. These examples show that the broadband photometry alone is well fit by an Lyα break resulting in extremely redshifted SEDs. When the medium-band photometry is added, the same optical region in the template combination is better fit by a Balmer break feature, decreasing their initial photo-z estimates, making them more consistent with the spec-zs. Additionally we see some differences in the continuum shape: broad bands show a gradual slope while narrow bands show a break in Figure 7.4; broad bands show a sudden break, and narrow bands show a more gradual break in Figure 7.8.

Quantifying the effect, we can see from Table II that when adding medium-band filters we generate a $\sim 20\%$ improvement over photometric redshifts using broadband filters alone.

7.3.2 The Performance of Near-Infrared Bands

At this point it is not surprising to state that as more bands are added, the better our photo-z accuracy. Figure 7.6 shows a very good example of how redder bands tighten the accuracy around the relation photo-spec-zs, eliminating false redshift solutions. In this example, broad- and medium-band filters are not sufficient to sample the Balmer break feature that lies in the near-infrared region, determining a $z_{\rm phot} = 0.018$, far below $z_{\rm spec} = 2.067$. When near-infrared photometry is added, we are able to explore a region where the 4000$\mathring{A}$ and Balmer break lie when the object is located at $z > 1.2$. As a result the photo-z estimate is in total agreement with its spectroscopic counterpart. We quantify the effect of the near-infrared bands in Table II. The improvement is not large due the lack of available spectroscopic redshifts in the region $z > 1.2$ in the area of the HDFS where JHK information is accesible.

7.3.3 Photometric Redshift Accuracy

There are many important factors to consider to obtain accurate photometric redshifts, such as the available wavelength coverage, the width and the number of filters in use, the magnitude of the sources in study, etc. To compare photo-zs of our sources with spectroscopic redshifts we divide the whole sample according to two main criteria which are shown in Figure 7.7. We limit the sample to sources with spectroscopic redshifts $0.1 \leq z \leq 1.2$, where the Balmer and 4000$\mathring{A}$ break fall within our optical bands. As seen in the previous section, these features can be more easily traced by our medium bands. We also base most of our study on sources with $R < 24$ as explained earlier, region where photo-zs estimates come from all medium- and broad- bands.

A common prescription to evaluate the accuracy is to calculate the median of $|z_{\rm spec} - z_{\rm phot}|/(1+z_{\rm spec})$ for all sources with spectroscopic redshift available. We find a median accuracy $\Delta z/(1+z) \sim 0.053$ out to $z \sim 4$ with out introducing the subdivision shown in Figure 7.7. We report median accuracies for cases of interest in Table II. It is noticeable the increase in accuracy as we include more bands, and limit the magnitude or redshift ranges.

We might be severely affected by the quality of spectroscopic redshifts when evaluating the accuracy of photometric redshifts as we include sources from redshift catalogs which adopt different selection criteria. To determine a more reliable redshift accuracy, it is of paramount importance to eliminate sources classified as outliers, which in many cases represent objects with the low quality flags or very faint magnitudes in the optical. We define outliers or catastrophic redshifts as sources with an accuracy value greater than $5 \times \Delta z/(1+z)$, comprising $\sim 10\%$ of the overall sample.

Table II: Photometric Redshift Accuracies.

Filters	No of Sources	Magnitude	Redshift Range	$\Delta z/(1+z)$
$UBVRIz$	400	$R < 26$	$0.0 \leq z \leq 4.0$	0.061
$UBVRIz$+11MB	400	$R < 26$	$0.0 \leq z \leq 4.0$	0.053
$UBVRIz$	321	$R \leq 24$	$0.0 \leq z \leq 4.0$	0.054
$UBVRIz$+11MB	321	$R \leq 24$	$0.0 \leq z \leq 4.0$	0.045
$UBVRIz$	273	$R \leq 24$	$0.1 \leq z \leq 1.2$	0.051
$UBVRIz$+11MB	273	$R \leq 24$	$0.1 \leq z \leq 1.2$	0.037
$UBVRIz^*$	244	$R \leq 24$	$0.1 \leq z \leq 1.2$	0.040
($UBVRIz$+11MB)*	244	$R \leq 24$	$0.1 \leq z \leq 1.2$	0.029
$UBVRIzJHK^*$	126	$R \leq 26$	$0.0 \leq z \leq 4.0$	0.044
($UBVRIzJHK$+11MB)*	126	$R \leq 26$	$0.0 \leq z \leq 4.0$	0.035

* After eliminating outliers which satisfy accuracies over five times the median of $|\Delta z/(1+z)|$.

EAzY is composed by very representative galaxy templates which permit the reconstruction of a large variety of SEDs. As photometric zero points are determined for each image separately, small offsets in adjacent bands cause appreciable color offsets. In order to make an adjustment to obtain accurate colors across the optical spectrum, and to consequently perform accurate SED fitting, we re-calibrate our photometry from the best galaxy combination EAzY fit, which is previously fixed to the spectroscopic redshift catalog. This simply represents a modification to the photometric data in order to provide information to the EAzY template set, as well as the default functional forms of the priors, based on spectroscopic samples. Even though these spectroscopic samples are usually highly biased, they could be very useful if we focus our study in particular type of objects for specific redshift ranges. We assume that this synthetic best-fit EAzY SED is a good approximation to the spectral shapes of the galaxies.

Given that each filter samples different regions for galaxies at different redshifts, any systematic photometric offsets in a filter is due to zeropoint errors in that band instead of a template mismatch in that filter.

To evaluate these photometric offsets we choose those high-quality spectroscopic redshifts for bright sources with a high signal-to-noise detection. Then we measure the offset of the observed flux from the synthetic flux in each medium-band filter, and the median among these values is defined as the zero-point correction. We are not taking into account broad-band filters as they have proved to be very accurate. Table III summarizes the zero-point corrections that we find for all medium-band filters when errors in flux are not normally distributed. These are to be applied in order to increase the photo-z accuracy. A more homogenous and larger sample of spectroscopic redshifts would determine a more accurate estimate for these photometric zero-point offsets. The increase in accuracy when these corrections are applied is over a 20%. These corrections were used for the final estimate of the photo-zs for the whole catalog of sources in the HDFS.

Table III: Photometric Zero-Point Offsets.

Filter	Zero Point Magnitude AB mag
ESO872.....	21.86
ESO874.....	21.62
ESO860.....	22.79
ESO862.....	22.00
ESO864.....	22.00
ESO867.....	22.25
ESO869.....	21.83
ESO848.....	21.59
ESO851.....	21.31
ESO853.....	20.59
ESO854.....	20.83

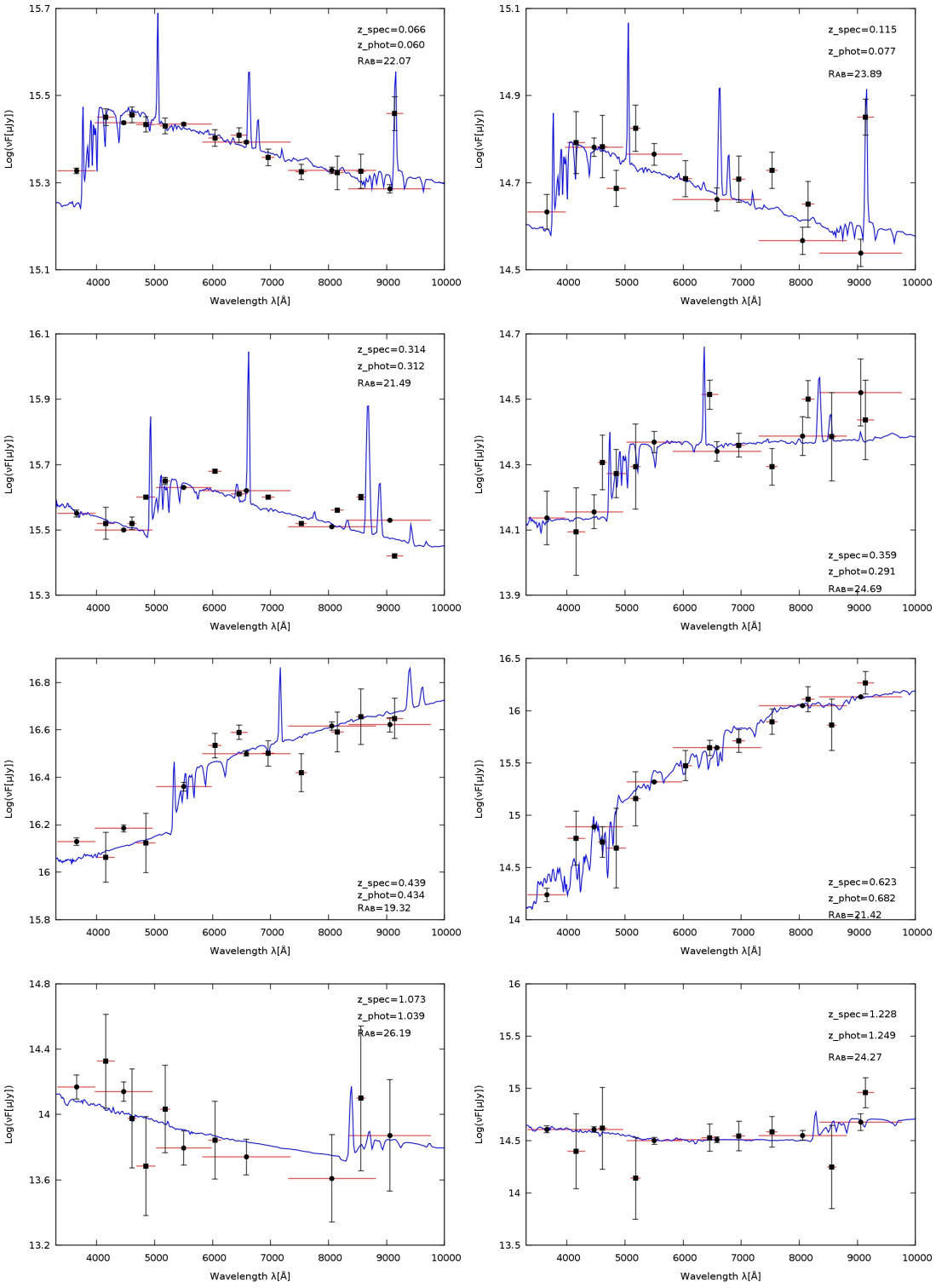

Figure 7.2: Example SEDs with EAzY spectral fits. The blue line represents the best template-fitting combination to the observed data. $UBVRIz'$ data is shown as black points and medium-band data is represented by black squares. The range of template spectra clearly fits the photometric data. The presence of a Balmer break is crucial for EAzY to determine a redshift. Horizontal red lines indicate the FWHM for each filter.

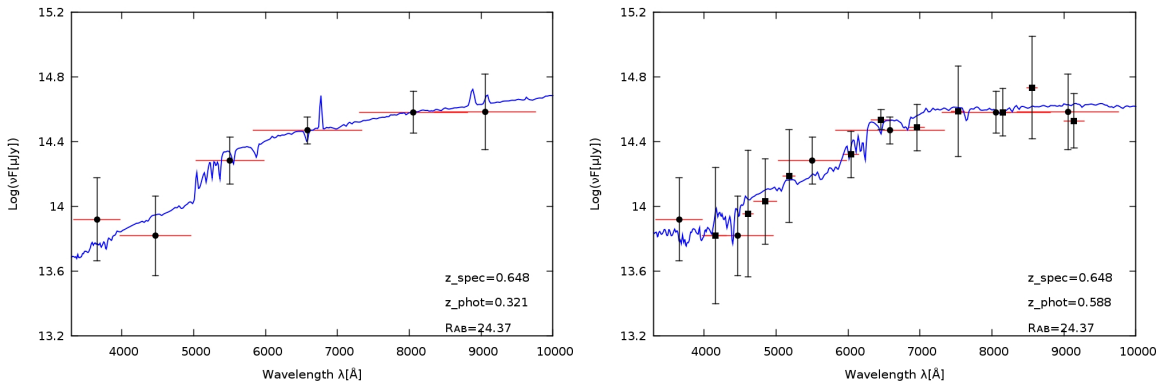

Figure 7.3: Two example SEDs of a source at $z \sim 0.648$. Broad-band filters (left) are not sufficient to fit the break around $6500\mathring{A}$, instead they fit a break at shorter wavelengths, subestimating the photometric redshift value. The photo-z estimate benefits when medium-band photometric data is added (right) as they efficiently trace the mentioned break with filters ESO864 and ESO867.

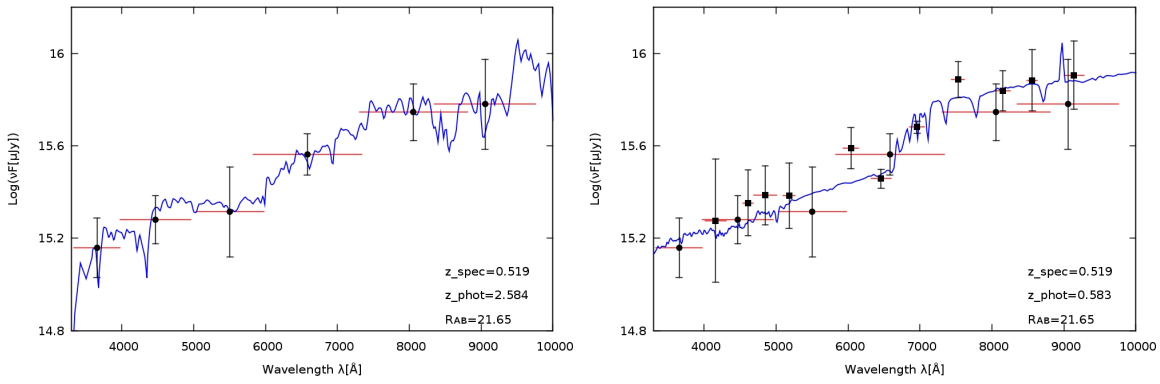

Figure 7.4: Two example SEDs of a source at $z \sim 0.519$. Broad-band filters (left) are not sufficient to provide information about special features that help to fit the SED and estimate a reliable photometric redshift. The photo-z estimate benefits when medium-band photometric data is added (right) as they efficiently trace a break at $\sim 6800\mathring{A}$ with filters ESO867 and ESO869.

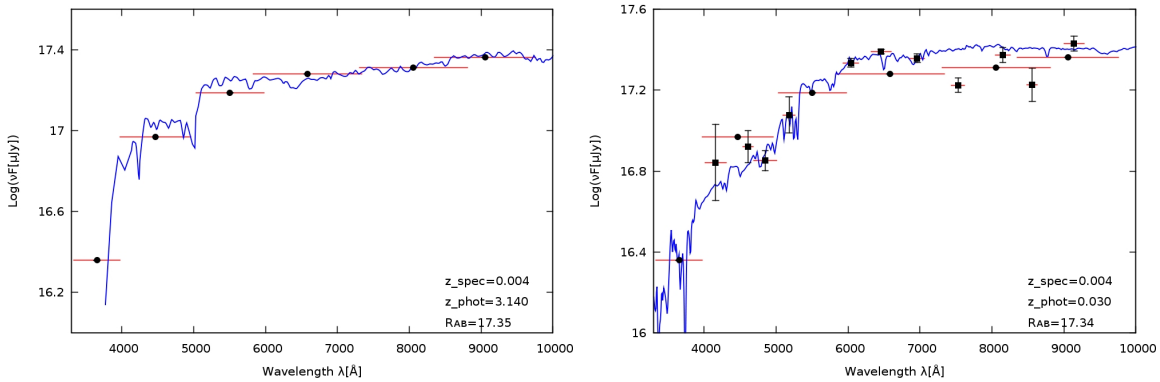

Figure 7.5: Two example SEDs of a very near source at $z \sim 0.004$. Broad-band filters (left) detect a prominent break at $4000\mathring{A}$, which is identified as a lyman break in the rest-frame, determining the SED of a high-redshift object. The photo-z estimate benefits when medium-band photometric data is added (right) as they provide information by the filters ESO874 and ESO860 to better classify this break as a $4000\mathring{A}$ break in the rest-frame.

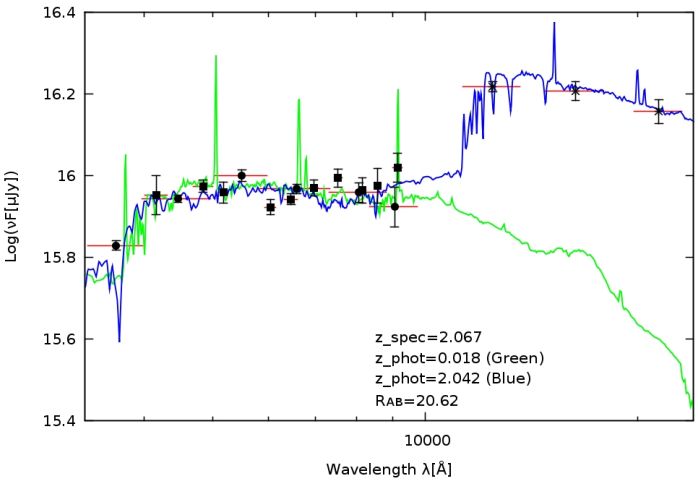

Figure 7.6: Two example SEDs of a source at $z \sim 0.023$. Broad-band filters (left) are not sufficient to fit the break around $4000\mathring{A}$, instead they fit a break at longer wavelengths, making an increase in the photometric redshift. This estimate benefit when medium-band photometric data is added (right) as they efficiently trace the mentioned break.

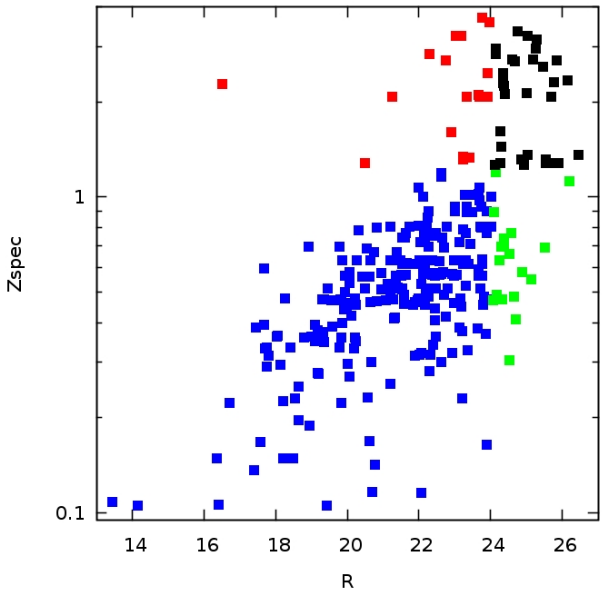

Figure 7.7: Distribution of sources in the plane B-Specz. Blue squares represents sources with $0.1 \leq z < 1.2$, where the Balmer break falls within our medium bands, and $R < 24$ to account for sources with more reliable photo-zs. The remaining cases are represented by red and green squares which are limited to $R < 24$ and $z < 1.2$ respectively, while black squares are sources expected to have unreliable photo-zs.

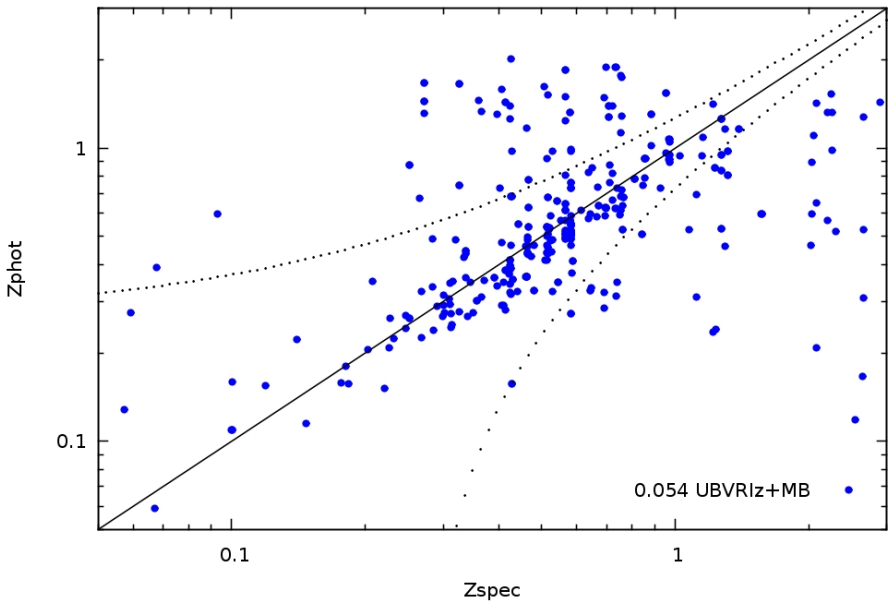

Figure 7.8: Comparison of photometric and spectroscopic redshifts for all sources obtained from literature with available high-quality spectroscopic redshifts. We find a median $|\Delta z| / (1 + z) \sim 0.043$. We trace dotted lines to separate catastrophic outliers which are defined by medians $|\Delta z/(1 + z)| > 5 * 0.043$.

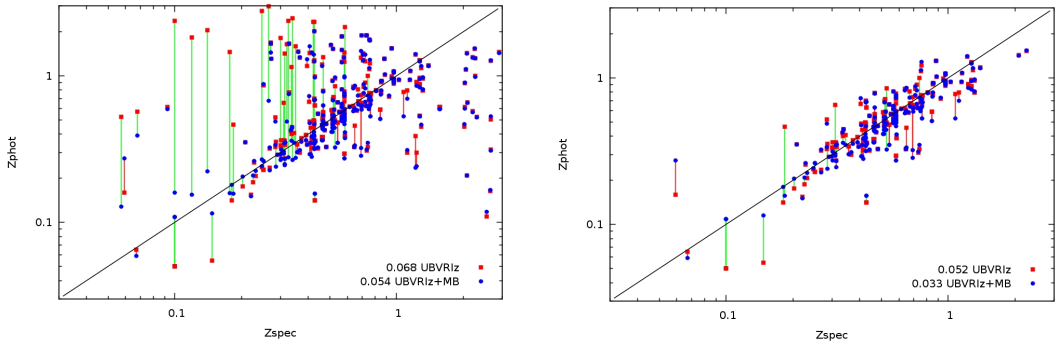

Figure 7.9: Comparison of photometric and spectroscopic redshifts with (left) and without (right) outliers for all sources with available spectroscopic redshifts. Red squares correspond to *PhotZs* using UBVRIz data only while blue points include the additional medium-band filters. Connecting lines are useful to compare both photometric redshifts estimates of the same source, as green lines show a closer estimate when including medium-bands, or a better photometric redshift obtained by broad bands only in red.

Chapter 8

Luminosity Functions of Radio Sources.

Here we present evolutionary properties and luminosity functions of radio sources as part of the analysis of the ancillary data described in chapter 4. Strong radio sources are associated to the most massive black holes and the most powerful starburst. Furthermore, theoretical work suggests an important role for the radio emission from AGN as regulators of star formation (Croton et al. 2006; Bower et al. 2006) although observational evidence is scarce (Rafferty et al. 2006; Nesvodka et al. 2008).

The radio data used here corresponds to 1.4, 2.5, 5.2 and 8.7 GHz maps of the HDFS obtained with the Australia Telescope Compact Array and published by Huynh et al. (2005, 2007) resulting in 466, 71, 24 and 6 sources at a $\sim 5\sigma$ level, respectively. Additional 71, 18 and 2 sources at 2.5, 5.2 and 8.7 GHz were found as lower signal-to-noise counterparts of 1.4 GHz reliable detections. Even though all maps are similarly sensitive, reaching a central rms $\sim 10\mu$Jy in the central regions, the number of sources reflects the much smaller field of views of the higher frequency observations, as shown in Figure 4.1. Source catalogs are available for this survey (ATHDFS) from the journal web page.

The subsample used here is composed by 303 1.4 GHz sources which all have available broad- and medium-band photometry, and radio data at 2.5, 5.2, and 8.7 GHz for 42%, 8% and 1% of the sources, respectively. Our optical and faint radio flux density limits, provide an

opportunity to perform a spectral classification scheme, disentangling starbursts from AGNs, and to study the evolution of this sample of galaxies in the Hubble Deep Field South.

8.1 The Luminosity Function

A luminosity function is usually defined as the number density of galaxies in an interval of luminosity or absolute magnitude. We calculate the differential luminosity function using the sum of non-parametric $1/V_{\rm max}$ estimators (Schmidt 1968) for each galaxy, defining magnitude bins as

$$\phi(M)\Delta M = \sum_i \frac{1}{V_{i,\rm max}(M,z)} \ , \tag{8.1}$$

where $V_{i,\rm max}(M,z)$ is the total comoving volume in which galaxy i could be detected according to the magnitude flux limit of the survey. This assures a spatially homogenous detection of galaxies, as intrinsically bright galaxies can be detected at large distances, while intrinsically faint objects are only detected at short distances due to the survey limiting depths. Instead of propagating errors in magnitude and redshift, we only take statistical Poissson noise from the galaxy counts. Thus the associated errors of $\phi(M)\Delta M$ can be computed from the square roots of the variances as

$$\sigma_\phi = \sqrt{\sum_i 1/V^2_{i,\rm max}(M,z)} \ . \tag{8.2}$$

Rest-frame fluxes were computed from the best-fitting EAZY template, following the procedure detailed by Wolf et al. 2003 for COMBO-17. This is very different from a K-correction, as it uses the observed medium- and broad-bands that are closest in observed wavelength to the redshifted rest-frame band of interest. As the K-correction normally uses a small set of band measurements, which are not always available for high-z/faint sources, our methodology, which relies in the whole SED information, is much more robust when determining rest-frame photometry.

For a parametric calculation of the luminosity function we use a Schechter function (Schechter

1976) of the form

$$\phi(M)dM = 0.4 \ln \left[10\phi^* 10^{-0.4(\alpha+1)(M-M^*)} \exp\left(10^{-0.4*(\alpha+1)(M-M^*)}\right)\right] \ , \qquad (8.3)$$

where M is the galaxy absolute magnitude and $\phi(M)dM$ is the number of galaxies with magnitude between M and $M + dM$ per Mpc^3. The set (α, M^*, ϕ^*) of free parameters are determined from a fit to the data points using an implementation of the nonlinear least-squares (NLLS) Marquardt-Levenberg algorithm. The slope of the function at the faint end is determined by α; M^* is called the characteristic Schechter luminosity after which the luminosity function falls exponentially; and ϕ^* is the number of galaxies per Mpc^3 per magnitude at the characteristic luminosity.

8.2 Luminosity Functions by Spectral Type of Radio Sources

A historic question about the optical luminosity function was whether different luminosity functions should be used for different galaxy types. First clues arised from the study of the local field and galaxy clusters (Sandage et al. 1985, Binggeli et al. 1987). If dwarf ellipticals and ordinary ellipticals are considered separately, two different number density distributions arise; the same is true for irregulars and spirals. It turned out that there was a considerable uncertainty in the local values of α and ϕ^*. Larger surveys solved this for the field (2dF, SDSS).

As luminosity functions depend strongly on SED-type at all redshifts, different galaxy types are expected to evolve differently; redder galaxies are generally presumed to be older and thus more slowly evolving. It has been shown that the faint-end power-law slope is SED-type dependent but with very small variations along redshift (Wolf et al. 2003). The different evolution of different galaxy types can constrain theories on the formation of galaxies; thus, it is of interest to study this differential evolution.

8.2.1 Galaxy Spectral Classification

Since luminosity functions are different for different morphological types, we want to separate our galaxy samples following their SED types and colors. Therefore we perform a simple template-template fitting approach for every object by comparing its best-fitting template combination derived from EAZY and the Kinney-Calzetti spectral atlas of galaxies in the optical range, redshifted according to the best photometric redshift estimate for that object. The most likely Kinney-Calzetti template spectra follows from a χ^2-statistical analysis. The Kinney-Calzetti spectral library covers various galaxy morphological types, including a set of starbursts for low $E(B-V) < 0.10$ to high $0.61 < E(B-V) < 0.70$ internal extinction. Irregular galaxies are partially covered by some starburst templates which were constructed using starburst galaxies classified with this morphological type. Details about how the elliptical to late spiral templates have been constructed can be found in Kinney et al. 1996, and in Calzetti et al. 1994 for the case of starbursts.

Our χ^2 analysis shows that some templates yield similar results for a given galaxy. This is the result of little diferentiation between some of the template SEDs, as can be seen in 8.1.Therefore, it was decided ti group the templates into four composites.

These templates are coupled as shown in Figure 8.1. The new spectral types are defined as ES0, Sab, Scd, and SB, covering elliptical to lenticular galaxies, early Sa to late Sb galaxies, Sc to Sd spirals, and the whole set of starbursts respectively. Cases that do not match any spectral class yielding a large χ^2 in the previous analysis presented in chapter 7, or those that fit very poorly over all Kinney-Calzetti templates, are assigned a black cross in the diagram below. These ambigous cases represent $\sim 15\%$ of all the sample, and will not be necessarily discarded in the next sections. For the remaining of our objects we have elliptical and lenticulars ES0 (62), spirals Sab (77), spirals Scd (73), and starbursts SBs (46).

In order to have a spectral template that would describe luminous, unobscured AGN (the QSO class), we have added to the Kinney-Calzetti atlas the median composite quasar spectrum determined by Van den Berk et al. (2001), which is publically available and shown in the right

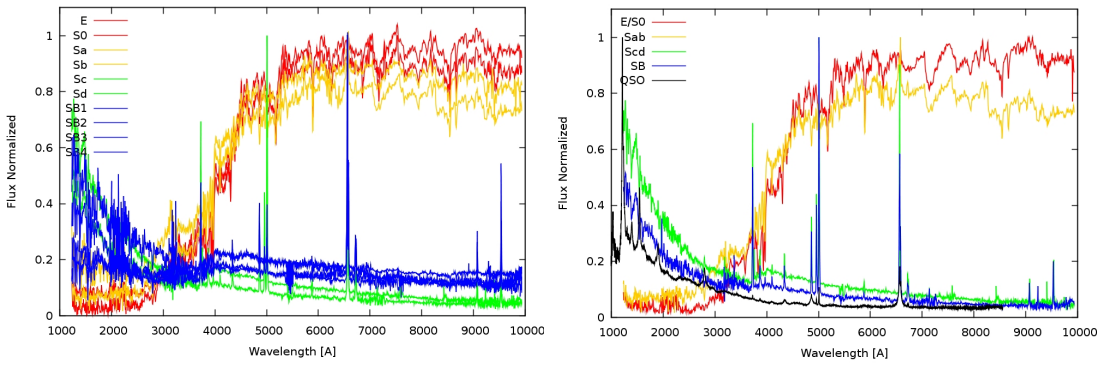

Figure 8.1: Kinney-Calzetti templates from the spectral atlas of galaxies in the optical (left) and the composite templates following same colors as shown (right) with the QSO template included in black

panel of Figure 8.1. This composite quasar template was determined using a homogeneous data set of over 2200 spectra from the Sloan Digital Sky Survey (SDSS), and covers a redshift range of 0.044$\leq z \leq$4.789, an absolute magnitude $-26.5 \leq r' \leq -18.0$, and rest-wavelength coverage of 800-8555 $\mathring{A}$.

Next we obtain synthethic colors by measuring U, B, V and R rest-frame magnitudes from the best fit EAZY SED using the appropiate filter curves. Finally, we construct a rest-frame color-color plot following the definitions made by Wolf et al. 2003. Results of the fitting procedure, and comparison with synthetic colors obtained from EAZY templates (Ts), and the Kinney-Calzetti-AGN spectral atlas of galaxies are shown in Figure 8.2.

Repeating the analysis this time including the quasar template, we found 58 ES0s, 70 Sabs, 62 Scds, 28 SBs, and 40 QSOs spectral types. There is a considerable migration of late type galaxies, Scd and SB, to the QSO class. The number of objects that are re-classified as QSO increases sistematically when moving from early to late types. This effect is easily explainable as the median composite quasar spectrum determined by Van den Berk et al. (2001) corresponds to a luminous unobscured AGN, which makes objects with a blue spectrum in the optical to be better classified as a QSO.

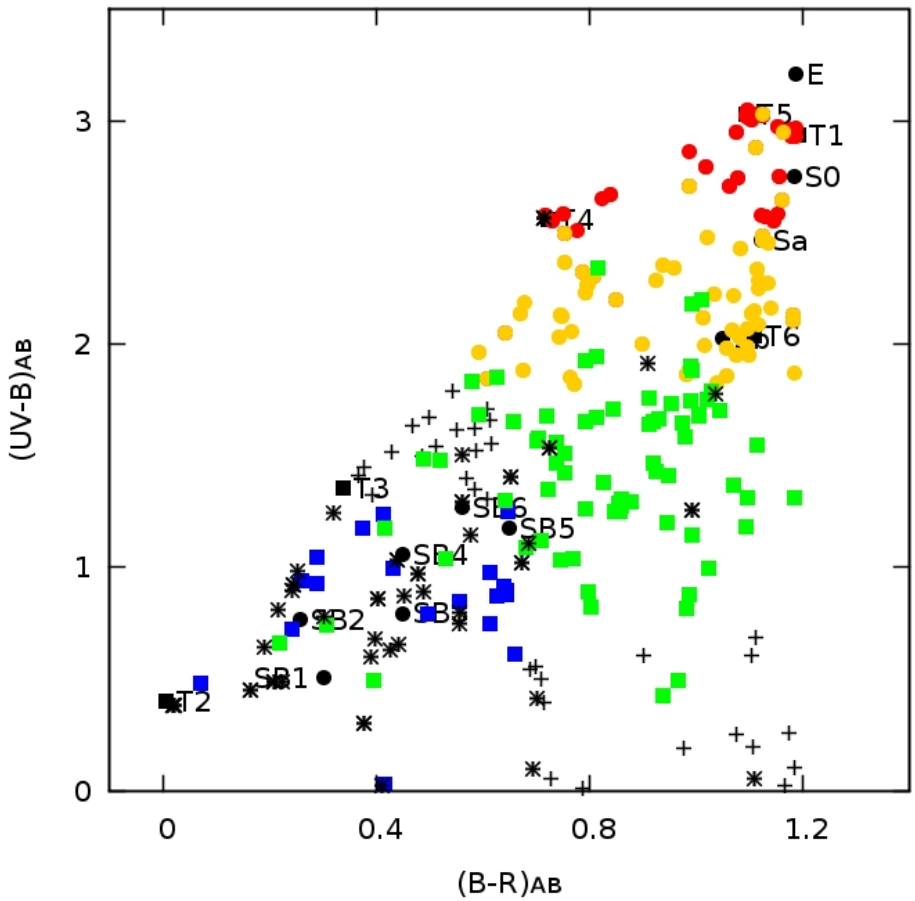

Figure 8.2: Rest-frame colours $(UV-B)_{\rm AB}$ vs $(B-R)_{\rm AB}$ of radio sources. Different symbols represent *ES0* (red), *Sab* (yellow), *Scd* (green) and *SB* (blue) galaxy SED-types following a classification using the Kinney and Calzetti spectral templates, and the *QSO* class with black stars. The ten original Kinney templates (black circles) and EAZY templates (black Ts) are also included. Black crosses represent sources with no reliable spectral classification.

8.2.2 The SED Type Dependence: General results

Because of the relatively small number of radio sources, we first determine the number density of galaxies for the whole sample separated by SED-types in the redshift regime $z = [0.1, 1.0]$. Later we will examine results in different redshift bins. We have discarded the very local regime ($z < 0.1$) as the volume is too small and redshift errors can have a large impact. We do not include those galaxies best fit with a QSO template as we want to compare our results with those found in the literature for the general galaxy population, unless we have a good fit that resembles one of the Kinney-Calzetti spectral types. Given the radio nature of our sources,

it is quite likely, however, that a significant number of AGN still remain in the sample. Figure 8.3 shows the luminosity functions for radio sources in the restframe B passband along with a Schechter fit and the value of the set (α, M^*, ϕ^*) of free parameters. Colours are assigned in agreement with the spectral classification performed in the previous section. Error bars reflect the 1σ Poisson variance. Despite the considerable wavelength coverage, we only construct LFs in the B-band, as for smaller or larger wavelengths many objects fall outside the available coverage for low and high redshifts respectively.

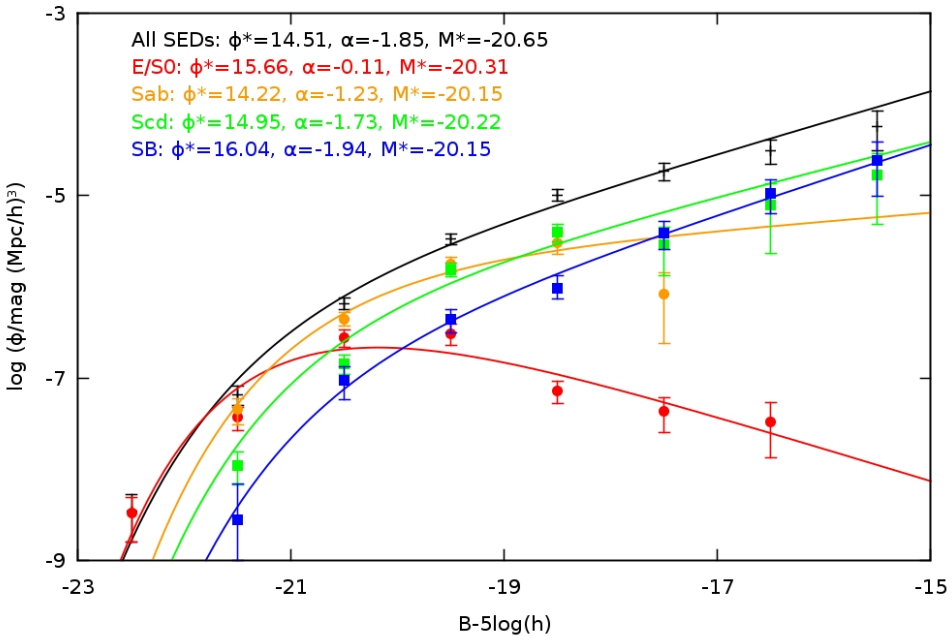

Figure 8.3: Luminosity functions for radio sources and its dependency on SED-types in the redshift regime $z = [0.1, 1.0]$ in the B passband. ES0, Sab, Scd, and SB template ranges are in red, yellow, green, and blue respectively. The combination of all the rest LFs is in black. Schechter functions are fit to $V_{\rm max}$ datapoints with their Poissonian errors for each case, with the determinations of their parameters as shown. ϕ^* is presented in units of 10^{-4}.

Our optical images ($R < 24$) allow us to reach well below the knee of the luminosity function, M^*, so that the faint end slope α is fairly well constrained. Figure 8.3 shows that later SED types have a steeper faint end of the luminosity function, which is in agreement with findings of the general galaxy population (Faber et al. 2007; Bell et al., 2004; Wolf et al., 2003). This behaviour has been shown in many bandpasses by Wolf et al. 2003, despite some migration of objects between classification types when changing bands.

Table I: Best-Fit Schechter Parameters.

Galaxy Type	ϕ^* $\times 10^{-4}$	M^*	α	$\log j_B$
E/S0	15.66	-20.31	-0.11	7.49
Sab	14.22	-20.15	-1.23	7.48
Scd	14.95	-20.22	-1.73	7.98
SB	16.04	-20.15	-1.94	8.67

Our results from the best-fit Schechter functions are presented in Table I. The results are very close to those presented by Wolf et al. 2003 for the COMBO-17 survey. It is obvious from Table I that the characteristic absolute magnitude, M^*, does not show a clear dependency with SED type, except for ES0-type galaxies, which provide most of the contribution at bright magnitudes. The density contribution at faint magnitudes increases for spiral galaxies between Sab and Scd-types while SBs present the steepest α index. The values for SBs are surprisingly too large. Again, this might suggest a significant AGN contribution, since the local AGN LF is characterized by a particular steep slope ($\alpha < -2.0$, Schulze et al. 2009 & Hao et al. 2005).

As suggested by previous works (Faber et al. 2007; Bell et al. 2004), the luminosity density $j_B = \int L\phi(L)dL = L^\star\phi^\star\Gamma(\alpha+2)$ constitutes a more robust parameter to derive since it is less sensitive to the uncertainties in the best-fitting procedure which strongly couples the determination of $L^\star$ and $\phi^\star$. However, the extrapolation to low luminosities becomes extremely sensitive to α through the $\Gamma(\alpha+2)$ term. This is particularly important for the steeper values determined for Scd and SB-type galaxies as seen in Table I.

8.2.3 The Redshift Evolution of M^* and ϕ^* Since z $\sim$ 1.

Since the low luminosity tail of the luminosity function is first impacted by small uncertainties, to study the redshift evolution of the characteristic luminosity M^* and density ϕ^* we fix the value for α. Figure 8.14 shows luminosity functions in the redshift intervals $z_1 = [0.1, 0.4]$, $z_2 = [0.4, 0.7]$, and $z_3 = [0.7, 1.0]$, and the evolutionary patterns (M^*, ϕ^*) separated by SED types adopting the α values found in the previous section depending on SED type for the whole

redshift regime.

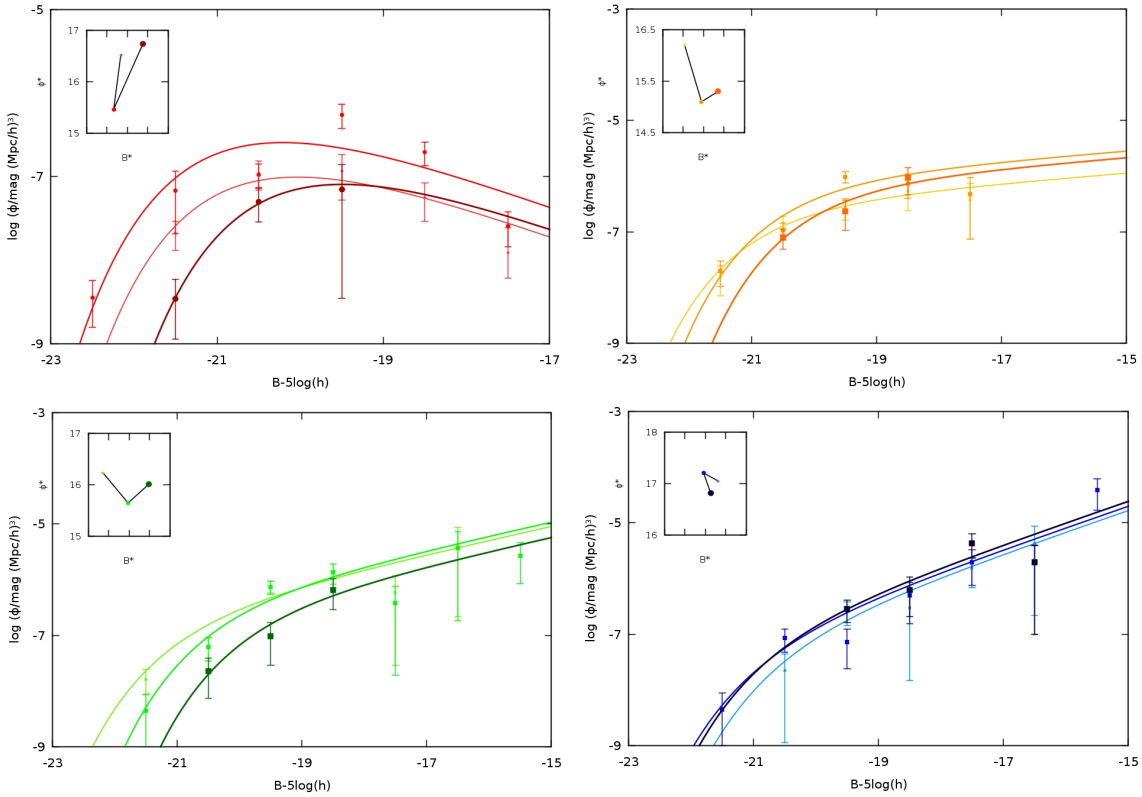

Figure 8.4: Redshift evolution of the B-band luminosity function of radio sources for our selected SED-types. Redshift intervals were chosen to be $z_1 = [0.1, 0.4]$, $z_2 = [0.4, 0.7]$, and $z_3 = [0.7, 1.0]$. ES0, Sab, Scd, and SB template ranges are in red, yellow, green, and blue respectively. The size of datapoints indicate how far we are in redshift, with smaller points corresponding to z_3. The small frame in each graph contains information of how the (M^*, ϕ^*)-vector evolves with redshift.

Displacement of the luminosity function is very clear for ES0 types. Moreover it is possible to notice how the luminosity function parameters evolve depending on SED types, both in its density normalization ϕ^*, and in its characteristic luminosity, M^*. However the errors found in the last redshift regime are too large, so it is not convenient to trace an evolutionary pattern from the highest redshifts.

Excluding the last redshift interval we find a common magnitude fading with cosmic time for all SED types excepting SBs, which show almost no luminosity evolution. The strongest evolving type corresponds to the ES0 galaxies, a result already seen in the general galaxy population (Faber et al., 2007, Bell et al., 2004). Is is also noticeable that the evolution of ϕ^* increases by more than an order of magnitude from $z = 0.7$ for ES0 and Sab types; for Scd types this

increase is about half an order of magnitude; while for SBs ϕ^* remains almost constant from $z = 1.0$.

8.3 Luminosity Functions of Radio Detected AGN and SFGs

The study of the evolution and luminosity functions of AGNs and star-forming galaxies (SFGs) in the radio band should provide a view of the extragalactic universe unaffected by the absorption which limits information obtained at most other wavelengths. Radio observations can help to understand the relationship between star formation and active galactic nuclei, as the growth of supermassive black holes in AGNs seems to be related to the growth of stellar mass in galaxies. In more detail, winds and jets from active black holes can compress or blow up the surrounding gas, accelerating or stopping star formation, playing a regulating, albeit complex, role in galaxy evolution. Which process is dominant and how this impacts the stellar growth in the host galaxies remains an open issue. In this section we characterize the radio source population to determine a sensus of galaxies and their radio emission mechanisms using the ATHDFS radio sample.

8.3.1 AGN / SFG Separation

The bright radio sky is composed by a population of galaxies whose luminosities range from $\sim 10^{20}$ W Hz^{-1} to $\sim 10^{27}$ W Hz^{-1}. AGNs and star forming galaxies (SFG) are the type of objects that should dominate our sample.

In this part of our study we define radio-quiet AGNs as sources in which most of the electromagnetic emission is thermal and jets are absent or very weak; on the other hand, radio-loud AGNs correspond to sources in which there is significant non-thermal emission produced through very strong radio jets. This last group also includes the radio galaxies class with jets lying in or near the plane of the sky while the active nucleus remains obscured and therefore not having a QSO spectral class. Obscured AGNs and AGNs hosted by relatively luminous galaxies

might also not have a QSO spectral class.

In terms of flux level, it was generally accepted that the sub-millijansky radio source population was dominated by synchrotron emission generated from supernovae explosions, which is associated with star formation in mergers, interacting galaxies and normal starbursting galaxies. However, recently Padovani et al. 2011 have found that the sub-milijansky radio sky turns out to be a 50/50 mixture of SFGs and radio-quiet AGNs evolving at a similar rate, which is in agreement with other recent papers (e.g., Seymour et al. 2008; Smolčić et al. 2008). At higher flux levels, radio emission is mostly associated with the classical extended jet and double lobe radio emission from radio-loud AGN.

When radio data are available there are two key parameters that can be used to make a preliminary classification to separate AGN from SFGs. These are the radio power at 1.4 GHz ($P_{1.4\mathrm{GHz}}$), and the rest-frame ratio of radio-to-optical flux density, which is defined as $R = \log(S_{1.4\mathrm{GHz}}/S_B)$ in this work, where S_B is the rest-frame B-band flux density. It is possible to define some ranges for these parameters which might allow us to distinguish between the dominant radio emission properties in galaxies. Unfortunately, overlaping between radio sources of different nature is also present.

$R > 1.4$ signals radio-loud AGN hosted by massive ellipticals (e.g., Kellermann et al. 1989; Stocke et al. 1992). Radio-loud AGNs span a very large range of radio powers, and they can be separated into low- and high-luminosity Fanaroff-Riley (FR) I and II sources, respectively (Fanaroff & Riley 1974). The radio power dividing line between FRI and FRII sources is found at $P_{1.4\mathrm{GHz}} \sim 2 \times 10^{24}\mathrm{WHz}^{-1}$. A radio power as low as $P_{1.4\mathrm{GHz}} \sim 10^{22}$ W Hz^{-1} can also be accepted as a lower limit to single out radio-loud AGN, as this is at the faint end of the luminosity function derived by Urry & Padovani 1995. However, this is well within the range of powers seen in starforming galaxies, which dominate at $P_{1.4\mathrm{GHz}} \sim 10^{23}$ W Hz^{-1} and can extend to $P_{1.4\mathrm{GHz}} \sim 10^{24}$ W Hz^{-1} for the most powerful examples (Sadler et al. 2002; Best et al. 2005). Powers up to $P_{1.4\mathrm{GHz}} \sim 10^{26}$ W Hz^{-1} are only seen in powerful radio-loud AGN. From studies at $z < 0.4$, $R < 1.4$ and $P_{1.4\mathrm{GHz}} < 10^{22}$ W Hz^{-1} are generally associated with starbursts hosted

by spiral-type galaxies. However, low values of R and $P_{1.4\mathrm{GHz}}$, are also typical of radio-quiet AGNs.

We start by showing the distribution of the radio power at 1.4 GHz ($P_{1.4\mathrm{GHz}}$) and its dependency on SED-types (Figure 8.5) as defined by their spectral classification according to 8.2.1, namely elliptical and lenticulars (58), spirals Sab (70), spirals Scd (61), starbursts (28), and quasars (40). For a K-correction in the radio bands we use the observed radio spectral index measured between 1.4 and 2.5 GHz ($\alpha_{1.4\mathrm{GHz}}^{2.5\mathrm{GHz}}, S_\nu \propto \nu^\alpha$), which is available for almost all sources. For objects without $\alpha_{1.4\mathrm{GHz}}^{2.5\mathrm{GHz}}$ information, we use the median of this value corresponding to the spectral type of that object.

The distribution in Figure 8.5 is clearly dominated by sources in the $P_{1.4\mathrm{GHz}} \sim 10^{22-24}$ range. Therefore it is not clear whether they are dominated by AGN or starforming galaxies. Clearly, the general radio source population below $z \sim 1$ is not dominated in numbers by powerful $P_{1.4\mathrm{GHz}} \sim 10^{26}$ W Hz^{-1} radio-loud AGN. Also, it can be seen that while most types concentrate around $P_{1.4\mathrm{GHz}} \sim 10^{22.5}$ W Hz^{-1}, SB types show a significant peak at $P_{1.4\mathrm{GHz}} \sim 10^{23}$ W Hz^{-1}. Very low powers ($P_{1.4\mathrm{GHz}} < 10^{21}$ W Hz^{-1}) found for a small minority of sources are most likely driven by wrong values of the photometric redshift. With the purpose of making the analysis more robust, we focus on the distribution of sources with signal to noise ratios among the best first third, whose distribution is displayed in the right panel of Figure 8.5. In all radio power within the range displayed by our sources, $P_{1.4\mathrm{GHz}}$ is a poor discriminant on the nature of the radio emission.

Figure 8.6 shows the distribution of rest-frame radio-to-optical flux density ratio $R = \log(S_{1.4\mathrm{GHz}}/S_B)$ for our objects separated by their spectral classification. The various types have different characteristic R values. Galaxies classified as QSOs have the largest R values with a mean of $\langle R \rangle = 1.53$, followed very closely by SBs with a mean of $\langle R \rangle = 1.48$. Elliptical and lenticular types have $\langle R \rangle = 0.89$, while spirals have means of $\langle R \rangle = 0.67$ and $\langle R \rangle = 0.82$ for the cases of Sab and Scd respectively. In the right panel for high S/N sources, mean R values increase for all type of sources sistematically.

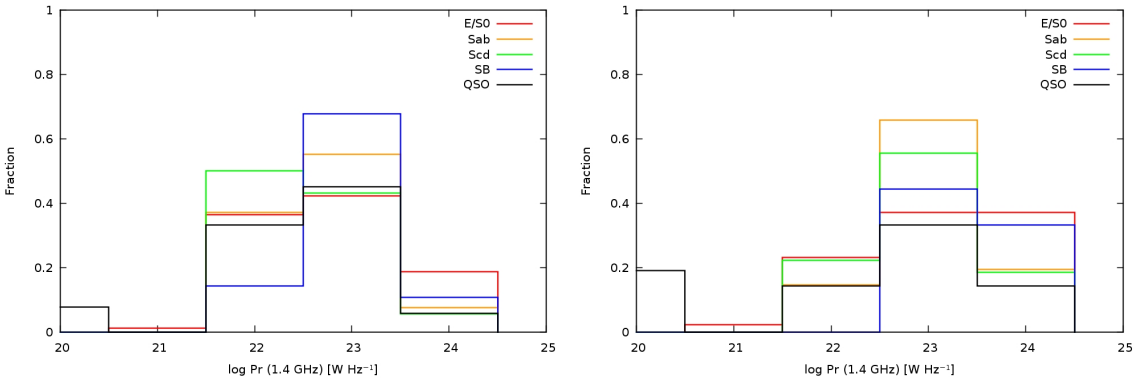

Figure 8.5: Distribution of the radio power at 1.4 GHz ($P_{1.4\text{GHz}}$) and its dependency on SED-types for the radio sample in the redshift regime $z = [0.1, 1.0]$, for all radio sources (left) and those with a good signal-to-noise ratio (right). ES0, Sab, Scd, SB, and QSO template ranges are in red, yellow, green, blue, and black respectively.

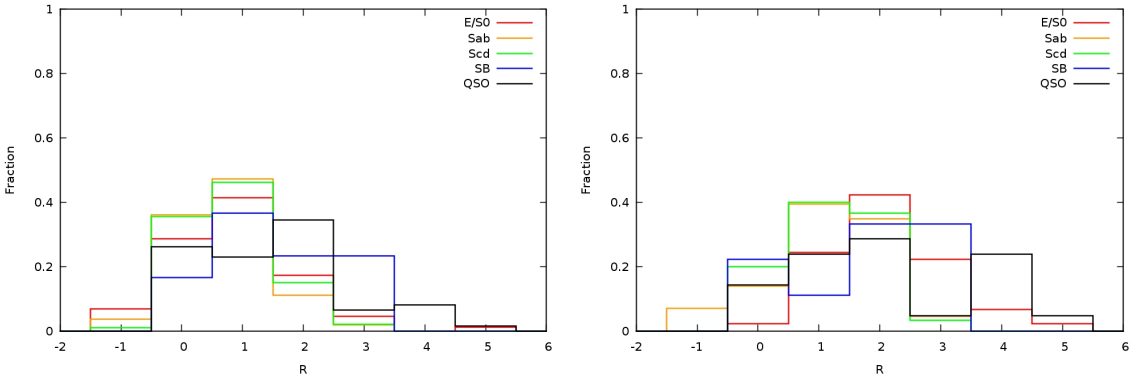

Figure 8.6: Distribution of the rest-frame radio-to-optical flux density ratio $R = \log(S_{1.4\text{GHz}}/S_B)$ and its dependency on SED-types for the radio sample in the redshift regime $z = [0.1, 1.0]$, for all radio sources (left) and those with a good signal-to-noise ratio (right). ES0, Sab, Scd, SB and QSO template ranges are in red, yellow, green, blue, and black respectively.

The large fraction of objects with $R > 1.4$ and not classified previously as QSOs hints a significant contribution of AGN activity in theses galaxy types. In particular, it is expected that SFGs have relatively small R values, which is in disagreement with the distribution of some SBs in Figure 8.6 and their mean R value. This could be explained by the lower redshifts of previous studies when compared with ours ($\langle z \rangle \sim 0.54$), but it would require the presence of a significant population of SFGs with very powerful radio emission at $z > 0.4$, which is not supported by our data in the z versus $P_{1.4\text{GHz}}$ diagram shown in Figure 8.7. Hence it is expected that some of the galaxies currently classified as SBs will be better characterized as AGN. Alternatively,

the larger values could correspond to SFG with considerable obscuration in the optical part of the electromagnetic spectrum, which might boost the value of R. This is however unlikely, as prototype local dusty starburst galaxies such as NGC 253 and M82 (NGC3052) have small R values ($R \leq 1$ NED database), although the local ULIRG Arp 220 has $R \sim 1.4$. This source however, might still have a heavily obscured AGN as an important source of radiation.

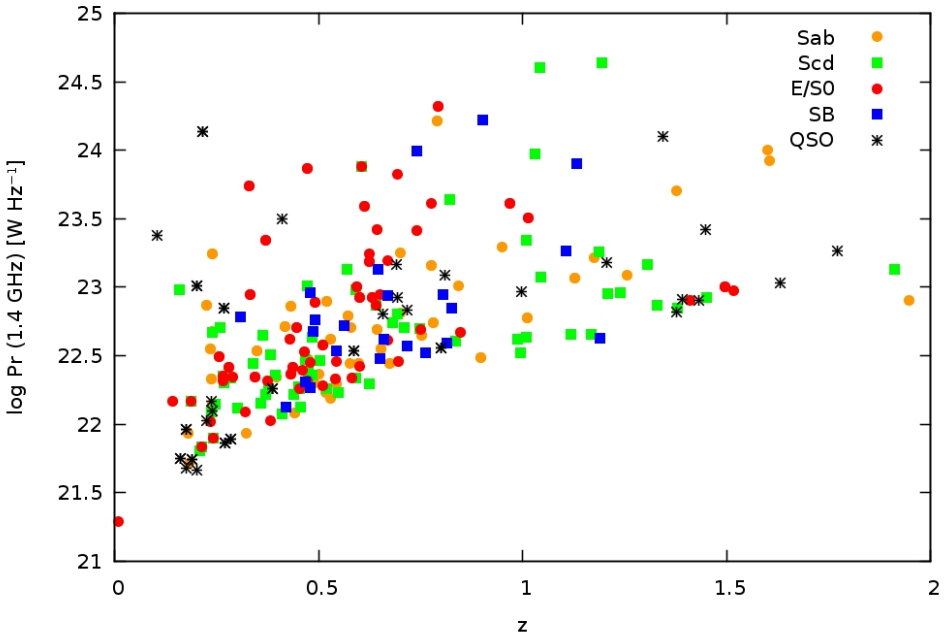

Figure 8.7: Radio power at 1.4 GHz ($P_{1.4\text{GHz}}$) versus redshift diagram in the redshift regime $z = [0.1, 1.0]$, for all radio sources. ES0, Sab, Scd, SB, and QSO template ranges are in red, yellow, green, blue, and black respectively.

Another potential discriminant to determine the nature of the radio sources is the radio spectral index α ($S_\nu \propto \nu^\alpha$). It has been shown that the synchrotron emission from star-forming galaxies typically has $< \alpha > \sim -0.7$, while AGNs have a flat ($\alpha \sim 0$) or even 'inverted' ($\alpha > 0$) spectral index, which cannot be produced by normal synchrotron emission (e.g., Huynh et al. 2007).

Figure 8.8 shows the distribution of the radio spectral index measured between 1.4 and 2.5 GHz $\left(\alpha_{1.4\text{GHz}}^{2.5\text{GHz}}\right)$ and its dependency on SED-types. In this study, α has typical uncertainties of $\sim 0.1 - 0.2$ and become larger for sources with $S_{1.4\text{GHz}} < 0.5$ mJy. Even though a clear trend between spectral galaxy-type and radio index is not seen, a large fraction of the sources show

values $\alpha > 0$, which indicate an AGN origin for their emission, while a peak appears centered around $\alpha \sim -0.7$, indicating that synchrotron emission is the dominant emission mechanism in these sources. Most of the galaxies associated to this peak are classified as spiral-types. Moreover, if we limit median α values only to sources with a good signal to noise ratio, which are shown in the right panel of Figure 8.8, it is possible to see that ES0 and QSO type galaxies have α values close to flat spectrums, with $< \alpha >= -0.11$ and $< \alpha >= -0.23$ respectively, while SBs have $< \alpha >= -0.84$, typical of synchrotron emission. Sab and Scd type galaxies have $< \alpha >= -0.42$ and $< \alpha >= -0.41$ respectively. Notice however, that this argument goes against previous suggestions of a significant fraction of AGN among SB galaxy types.

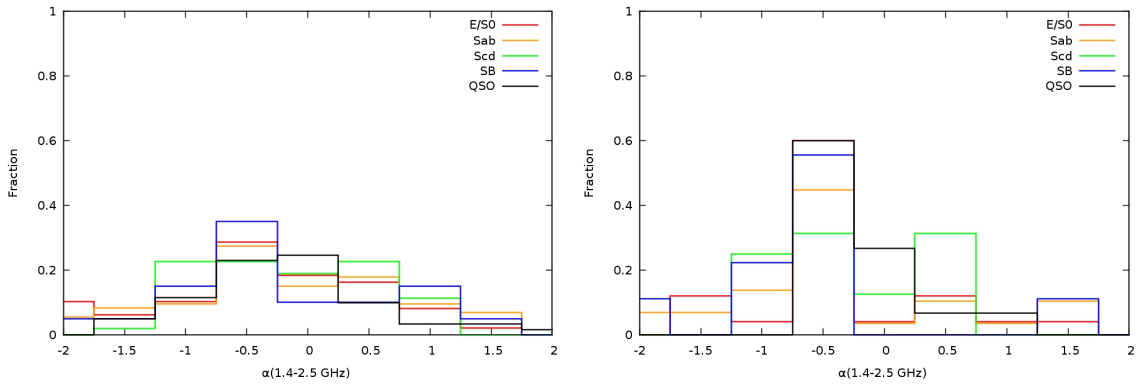

Figure 8.8: Distribution of the radio spectral index measured between 1.4 and 2.5 GHz ($\alpha_{1.4\mathrm{GHz}}^{2.5\mathrm{GHz}}$) and its dependency on SED-types for the whole sample in the redshift regime $z = [0.1, 1.0]$, for all radio sources (left) and those with a good signal-to-noise ratio (right). ES0, Sab, Scd, SB and QSO template ranges are in red, yellow, green, blue, and black respectively.

Padovani et al. 2009 and Padovani et al. 2011 selected SFGs based on low R (< 1.7) and moderate $P_{1.4\mathrm{GHz}}$ ($< 10^{24}$ W Hz^{-1}) values, optical morphology different from elliptical or lenticulars, and low X-ray power. The redefinition of R from the earlier value of 1.4 is due to a correction driven by the evolution of the starforming galaxy population asumming that radio power goes as $P \propto (1+z)^{2.7}$, as prescribed by Hopkins 2004. Counterintuitively, Padovani et al. 2009 assumed a passive evolution for the optical bands, hence finding a larger value of R at higher ($0.8 < z < 2$) redshifts. A better justified assumption would be to use results from the UV luminosity density evolution of starforming galaxies which goes as $\propto (1+z)^{2.5}$ up to $z \sim 1$, as presented by Arnouts et al. 2005 and Schiminovich et al. 2005. This UV,

and presumably optical evolution, would balance the change in radio power, resulting in an unchanged value of R at higher z.

The selection of radio-quiet AGNs in Padovani et al. 2009 and Padovani et al. 2011 was based on low values for R and $P_{1.4\text{GHz}}$, and high X-ray powers. AGNs not fulfilling this sequence of criteria were classified as radio-loud AGNs. The X-ray power criterion was only available for 33% of the sources, and is used to exclude AGNs from potential SFGs. To refine the classification procedure, near- and far-IR data were also included.

Figure 8.9 shows the rest-frame radio-to-optical flux density ratio versus the 1.4 GHz radio power for all the sources with spectral classification, highlighting objects classified as radio-loud AGN (see below). As it is expected, no sources occupy the bottom right quadrant, this is, there are no sources with power above $P_{1.4\text{GHz}} \sim 10^{24}$ W Hz^{-1} which have $R < 1.7$.

In our work we introduce similar criteria to those used by Padovani et al. 2011 but also include the information from the radio spectral index and do not include X-ray or IR observation. In order to compare with the work done by Padovani et al. 2011 we adopt the same dividing line between radio-quiet and radio-loud AGNs of $R \sim 1.7$ which, despite the previous discussion, makes this criterion more conservative.

RADIO-LOUD AGNS must satisfy the following requirements in our classification:

1. $R = \log\left(S_{1.4\text{GHz}}/S_B\right) > 1.7$
2. $P_{1.4\text{GHz}} > 10^{23.5}\text{WHz}^{-1}$
3. Spectral index $\alpha > -0.5$

We found a total of 14 radio-loud AGNs, with spectral types QSO (1), SB (2), E/S0 (6), Sab (4), Scd (1). These sources are at relatively high redshifts with a mean of $\langle z \rangle = 0.71$, and present high radio-to-optical ratios ($\langle R \rangle = 2.53$). Three sources with $R > 4$ are not displayed in the diagram of Figure 8.9, and corresponds to powerful radio galaxies. Those sources found in the upper right quadrant of the plot which have not been classified as radio-loud AGN do not

satisfy the α flatness requirement. Interestingly, one source shows a SED corresponding to a bona-fide unobscured AGN (1 QSO), while the remaining SEDs seem to be dominated by the host galaxy. Scd and SB type galaxies were not expected, since common wisdom dictates that radio-loud AGN are usually hosted by spheroidal galaxies. However, at higher redshifts the stellar population of many radio-loud AGN hosts is expected to have significant emission from powerful starbursts (Tadhunter et al. 2011).

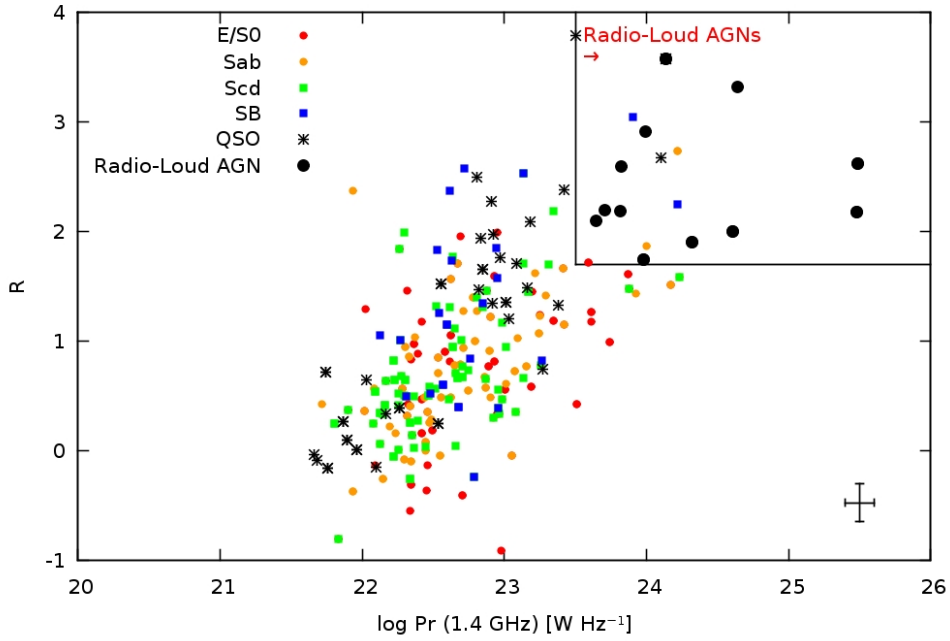

Figure 8.9: Rest-frame radio-to-optical flux density ratio $R = \log(S_{1.4\mathrm{GHz}}/S_B)$ versus the 1.4 GHz radio power $P_{1.4\mathrm{GHz}}$ for all sources. Optical spectral classifications are as before. The upper right region encloses sources classified as radio-loud AGNs.

We now turn into the classification of star forming galaxies (SFGs), which is displayed in Figure 8.10. The most challeging task is to differentiate SFGs from radio-quiet AGN in the bottom left quadrant of the R–$P_{1.4\mathrm{GHz}}$ plot.

We have seen that SFGs have relatively small R values, and can be strong radio emitters but still with radio luminosities lower than powerful radio-loud AGNs (i.e., $P_{1.4\mathrm{GHz}} < 10^{23.5}\mathrm{WHz}^{-1}$). At the same time, it is well established that the level of star-formation increases from early to late spirals, i.e., from Sa to Sc Hubble types. Hence, the high power end should be reserved for spectral types which agree with the presence of a dominant starburst (i.e., Scd

or SB spectral types). On the contrary, it is expected that Sab types of intermediate radio power correponds to AGNs.

Hence, we perform a twofold classification to define SFGs:

1. For $P_{1.4\text{GHz}} > 10^{22.5}\text{WHz}^{-1}$
   - $R = \log\left(S_{1.4\text{GHz}}/S_B\right) < 1.7$
   - Spectral index $\alpha \in [-0.5 : -0.9]$
   - Spectral classification Sab, Scd or SB.
2. For $P_{1.4\text{GHz}} <\sim 10^{22.5}\text{WHz}^{-1}$
   - $R = \log\left(S_{1.4\text{GHz}}/S_B\right) < 1.7$
   - Spectral index $\alpha \in [-0.5 : -0.9]$
   - Spectral classification SB or Scd.

We found a large fraction of SFGs (61). In more detail, we have star forming galaxies with spectral types Sab (13), Scd (36), and SBs (12). The mean redshift for this group of SFGs is $\langle z \rangle = 0.27$, clearly much lower than that of radio-loud AGN.

At this stage, we simply assume that all those galaxies found in this region which do not satisfy the criteria outlined above and have $P_{1.4\text{GHz}} \geq 10^{22}\text{WHz}^{-1}$ correspond to RADIO-QUIET AGN. We found a total of 124 of these objects, with spectral types E/S0 (44), Sab (35), and Scd (19) SB (5) QSO (15). They are at relatively high redshifts with $\langle z \rangle = 0.61$. We also find 22 unusual sources classified as radio-quiet AGNs, at $z \sim 0$ that fit very well the quasar template, have very high radio-to-optical ratios ($R > 2.0$) but extremely low radio powers ($\log P_{1.4\text{GHz}} < 20$). This rare cases may be explained by errors in the fits derived by EAZY, and they most likely correspond to high-z RL-AGN. Since we have no good information about their redshifts, we drop them from any further analysis.

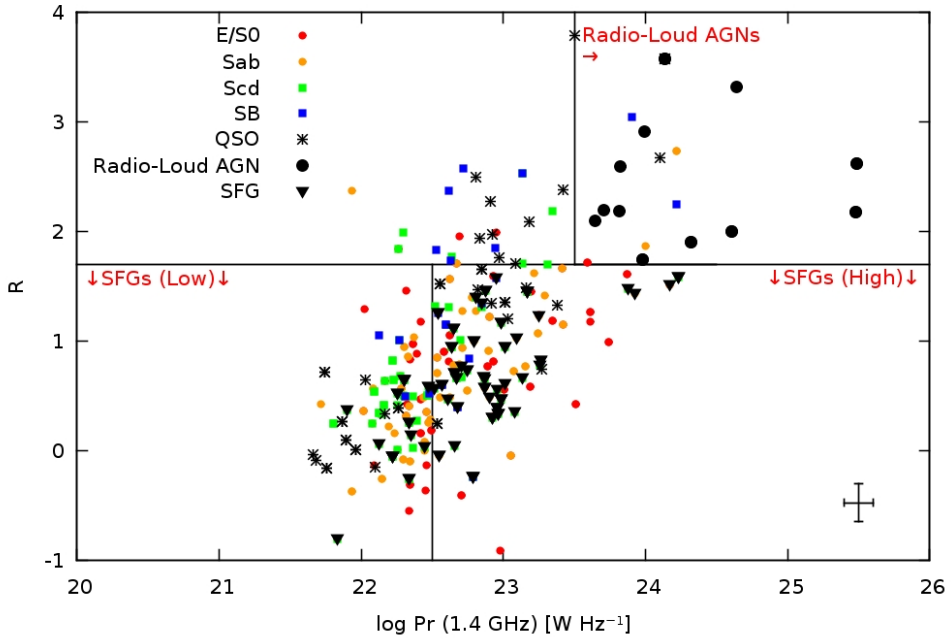

Figure 8.10: Rest-frame radio-to-optical flux density ratio $R = \log(S_{1.4\mathrm{GHz}}/S_B)$ versus the 1.4 GHz radio power $P_{1.4\mathrm{GHz}}$ for all sources. We highlight objects classified as radio-loud AGN and star-star forming galaxies according to redshift constraints. Other spectral classifications are as before.

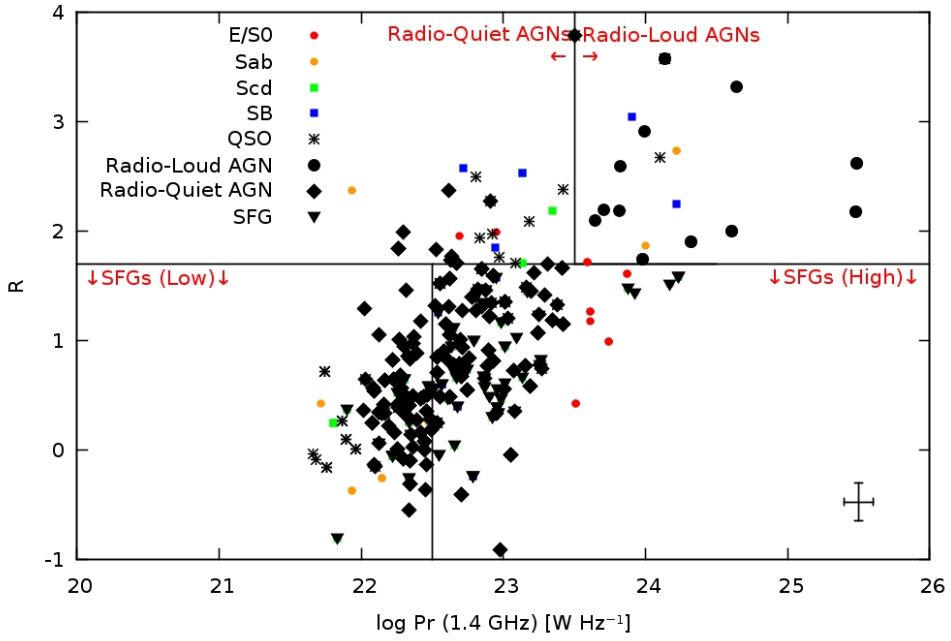

Figure 8.11: Rest-frame radio-to-optical flux density ratio $R = \log(S_{1.4\mathrm{GHz}}/S_B)$ versus the 1.4 GHz radio power $P_{1.4\mathrm{GHz}}$ for all sources. We highlight objects classified as radio-loud and radio quiet AGNs, and star-forming galaxies according to mentioned constraints. Other spectral classifications are as before.

We add one more step to find radio-quiet AGNs by focusing on the region that has not been considered in the definitions of radio-loud AGN and SFGs: the upper left corner of the R versus $P_{1.4\text{GHz}}$ diagram. We keep the requirements that AGNs are unlikely to have spectral indices values below -0.5. Hence adding radio loudness information the next conditions that must be satisfied by sources to be classified as RADIO-QUIET AGNS IN THIS QUADRANT ARE:

1. $R = \log\left(S_{1.4\text{GHz}}/S_B\right) > 1.7$
2. $P_{1.4\text{GHz}} < 10^{23.5}\text{WHz}^{-1}$
3. Spectral index $\alpha \notin [-0.5 : -0.9]$

This region of the R–$P_{1.4\text{GHz}}$ parameter space could be occupied by relativistically boosted radio-quiet AGN (also known as radio-intermediate AGN; Falcke et al. 1996; Barvainis et al. 2005), which correponds to radio-quiet AGN with a intrinsically weak jet, but which could be aligned with our line of sight. In this case the radio emission could show high values of R without being an intrinsically powerful radio source. Interestingly, a large fraction of sources with QSO classification occupy this quadrant of the diagram.

We found a total of 10 objects, with spectral types E/S0 (1), Sab (1), and Scd (3) SB (3) QSO (2) classified as radio-intermediate AGNs. They are found at higher redshifts ($\langle z \rangle = 0.79$) in very good agreement with the previous group of radio-quiet AGNs.

The remaining objects in the lower left quadrant of the plot that we have not classified according to our selection criteria are to be named NORMAL GALAXIES, i.e., those with radio powers $P_{1.4\text{GHz}} \leq 10^{22}\text{WHz}^{-1}$. In the literature they are thought to have their radio emission dominated by synchrotron radiation from interstellar relativistic electrons, but in this work we cannot determine whether this is the case.

In summary, we have been able to clasify 201 RL/RQ/SFG sources out of a total of 227. This comes from the fact that not all of them have a measured spectral index, or do not follow the selection criteria outlined before. Therefore we add new requirements in order to include

all the sources, through the flow chart shown in Figure 8.12. The new adjustments to the classification are as follows: Two sources with $\log P_r > 23.5$ & $R > 1.7$ do not satisfy the radio spectral index requirement to be classified as RL-AGN. These could be examples of extreme radio powerful starbursts which can have up to $P_r \sim 24$ and as Arp 220 $R > 1.0$. The best fit template to these object correspond to an obscured starburst or an unobscured starburst with uncertainties in the spectral index. Hence, we finally classify them as SFG.

Sixteen sources have $\log P_r > 23.5$ & $R < 1.7$. These could be extreme starburst or RQ-AGN. Since our α measurements are uncertain we will divide them into those two classes using only the best fit spectral type. This approach yields 12 SFGs and 4 RQ-AGN.

Most sources (194) have $\log P_r < 23.5$. Of those only 27 have $R > 1.7$. Some powerful starburst can still enter in this group. Again we will use the spectral type as main discriminator, using radio index to separate between RQ-AGN and SFGs among the QSO, ES0 and Sab classes.

Finally, 167 sources have $\log P_r < 23.5$ and $R < 1.7$. This corresponds to 167/227$\sim$ 0.74 of the total sample. These sources separate between 63 with spectral types SB and Scd, and 104 sources with types QSO, ES0 and Sab. Here, again, it is crucial to use the information of the radio index α to separate the last group into SFGs and RQ-AGN. It is found that the mayority correspond to the later.

Table II summarizes our final results on the classification, with relevant values for every class. As seen in the flow chart presented in Figure (8.12), radio sources are classified into radio-quiet ($\sim$ 46%) and -loud AGNs ($\sim$ 9%), star-forming galaxies ($\sim$ 39%), and normal (6%).

As mentioned before, Padovani et al. 2011 found a 50/50 mixture between SFGs and RQ-AGNs. The porcentual fraction of SFGs and RQ-AGNs is 46% and 54% respectively.

Table II: SUMMARY ON THE COMPLETE RADIO SOURCE CLASSIFICATION.

Galaxy Class	Spectral Type	N°	Redshift $\langle z \rangle$	Ratio $\langle R \rangle$	Radio Power $\langle \log(P_r) \rangle$
Radio Loud AGN	E/S0	8	0.73	1.47	24.61
	Sab	6	0.18	1.82	24.74
	Scd	2	1.25	2.31	24.68
	SB	2	0.66	2.69	23.63
	QSO	1	0.40	1.61	23.50
Radio Quiet AGN	E/S0	41	0.56	0.40	22.69
	Sab	35	0.61	0.47	22.71
	Scd	17	0.43	0.51	22.40
	SB	9	0.48	0.85	22.61
	QSO	10	0.48	0.85	22.61
Star Forming	E/S0	5	0.01	2.73	19.62
	Sab	18	0.20	0.54	22.91
	Scd	42	0.19	0.34	22.34
	SB	19	0.05	2.34	22.11
	QSO	12	0.05	2.34	22.11
Normal	E/S0	2	0.01	3.72	20.99
	Sab	4	0.20	0.47	19.87
	Scd	3	0.09	1.50	21.87
	SB	3	0.01	2.73	19.07
	QSO	3	0.01	2.73	19.07

8.3.2 Radio Luminosity Functions for AGNs and SFGs at $z < 1$.

Now that we have performed the classification into AGNs and star-forming galaxies, we can find the Radio Luminosity Function (RLF) and its evolution in redshift for the radio sources separately. We use the standard $1/V_{\rm max}$ method (Schmidt 1968) in a similar way as done in previous sections. We limit the accesible volumes according to magnitude limitations of the radio sample. We chose the 1.4 GHz band as this is available for all sources, and to compare with other works that predominantly make use of this radio frecuency. The parametric form of the fitted to the RLF is the Schechter function as described before. The parametric formulation this time uses

$$\Phi(L)dL = \Phi^* \left(L/L^*\right)^{\alpha} e^{-L/L^*} dL \ , \tag{8.4}$$

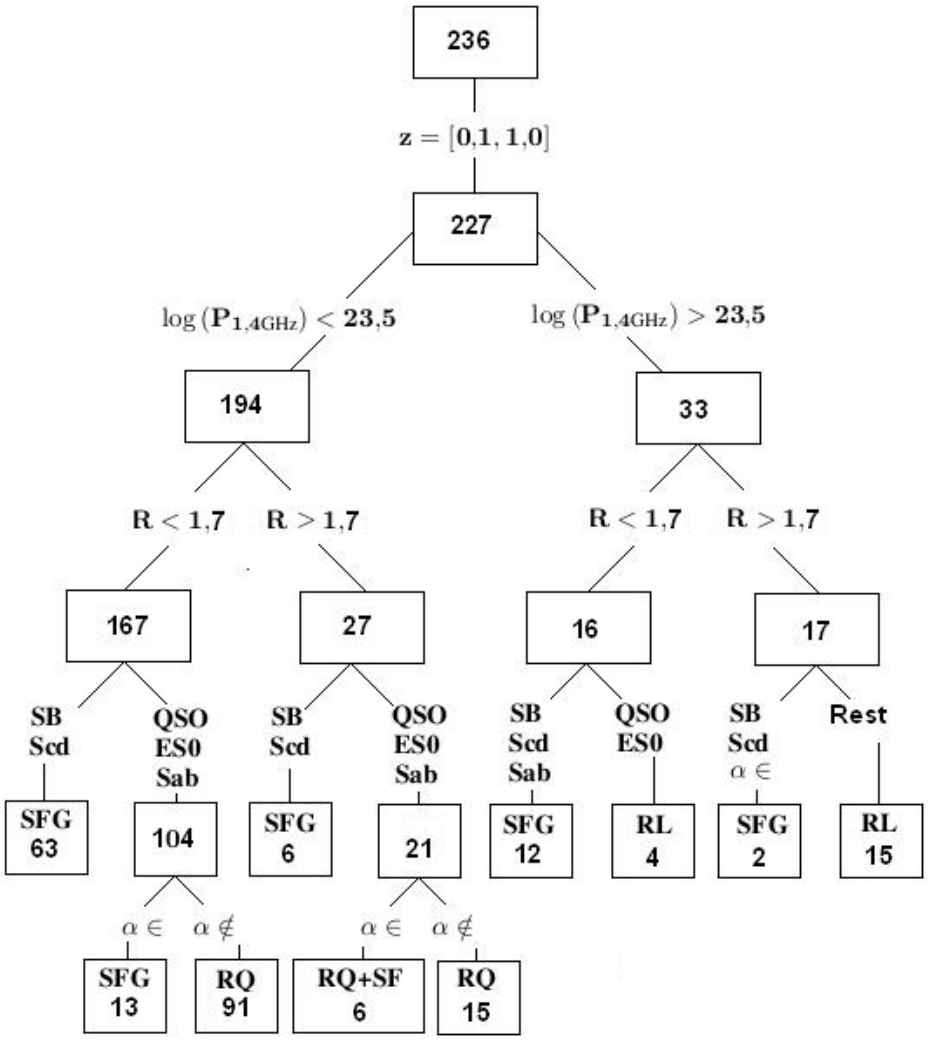

Figure 8.12: Flow chart of our final classification scheme.

where L is the galaxy radio luminosity and $\Phi(L)dL$ is the number of galaxies with luminosities between L and $L + dL$ per Mpc^3. This is done with the aim of a direct comparison with other works, as presented in the previous section.

For the redshift intervals we limit the available volume in which a galaxy can be located. The errors of $\Phi(L)dL$ are determined in the same way as done before, which means that we take only statistical Poisson noise from the galaxy counts into account.

In the next figures we show the 1.4 GHz RLFs for the whole sample of AGNs, radio-quiet and -loud AGNs, and star-forming galaxies. We define luminosity bins of $\Delta \log P_{1.4\mathrm{GHz}} = 0.5$

and redshift intervals $z_1 = [0.1, 0.4]$, $z_2 = [0.4, 0.7]$, and $z_3 = [0.7, 1.0]$ for our luminosity functions in all cases, excepting radio-loud AGNs due the small number of sources available. Symbols are associated with the definitions made before.

Figure 8.13 shows the 1.4 GHz luminosity functions for AGNs in the HDFS for the whole sample, which contains a total of 131 sources, and separated by our predefined redshift ranges. We also include the radio observations made by Smolčić et al. 2008 from the 1.4 GHz, 2-degree^2 VLA-COSMOS Survey and find a good agreement with our data. The large area mapped by Smolčić et al. 2008 explains the detection of the rare active AGNs with radio powers $P_{1.4\text{GHz}} > 5 \times 10^{25}$W Hz^{-1} in comparison with the small number of radio sources available in the Huynh's sample with high radio powers. The redshift intervals used by Smolčić et al. 2008 differ a little from ours. They are defined as $z_1 = [0.1, 0.35]$, $z_2 = [0.35, 0.6]$, and $z_3 = [0.6, 0.9]$.

L^* values increase with redshifts as expected, which means that sources with higher luminosities correspond to the characteristic luminosity after which the luminosity function falls exponentially. In the last redshift bin, the fit parameters have much larger errors than previous cases and L^* is not constrained by the data.

Fit parameters in the form $(\log L^*, \alpha, z)$ for radio-quiet AGNs only are $(23.79, -1.47, z > 0)$, $(23.63, -0.11, z_1)$, $(23.97, -0.21, z_2)$, and $(27.40, -0.71, z_3)$. As radio-quiet AGNs are almost seven times more abundant than radio-loud AGNs, the luminosity function for the former is expected to be very similar at lower luminosities as those shown in Figure 8.13.

Figure 8.14 shows the 1.4 GHz luminosity functions for radio-loud AGNs in the HDFS, which contains a total of 19 sources. Due the small number of radio-loud AGNs, we used a fixed value for α and no separation with redshift. We fixed this value as $\alpha = -0.46$ which is the average of the values obtained from fits made to the population of AGNs for $z > 0.4$ which is supposed to be the region where most radio-loud sources arise. By fixing the value for α we found a characteristic luminosity $\log L^* = 24.52$ with an uncertainty less than 2%.

Figure 8.15 shows the 1.4 GHz luminosity functions for radio-quiet AGNs in the HDFS. There is a total of 112 sources which are separated by our predefined redshift ranges. As

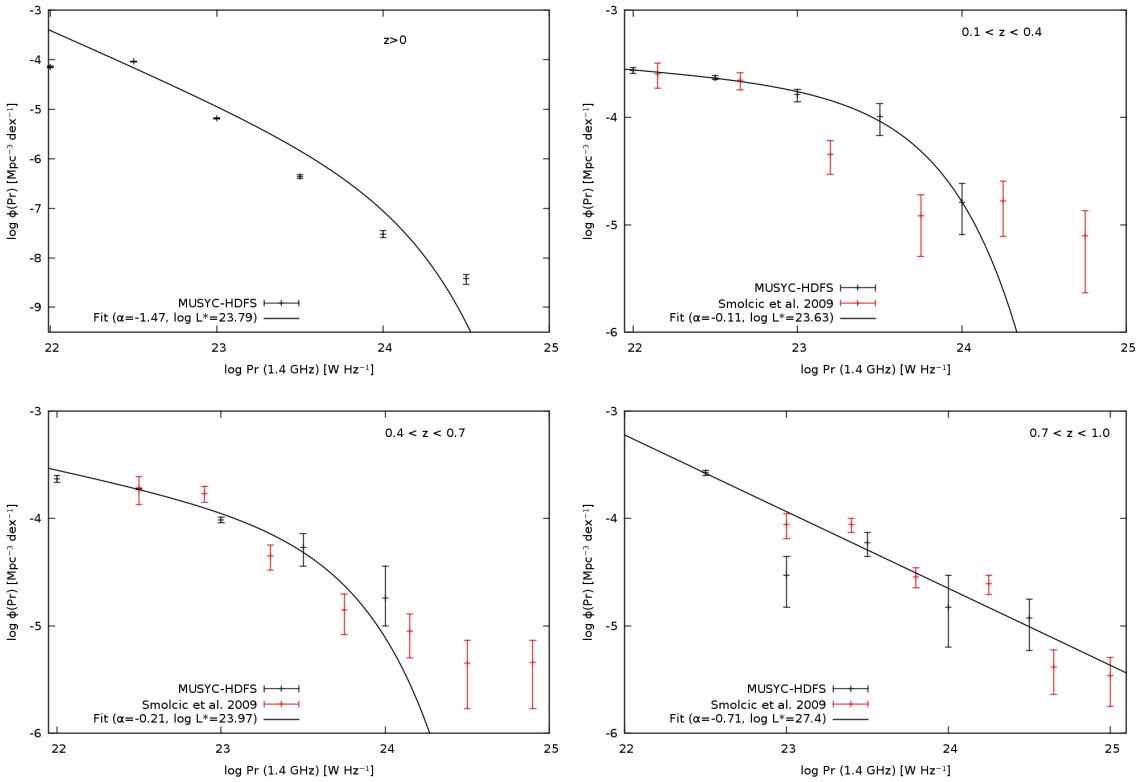

Figure 8.13: 1.4 GHz radio luminosity functions for AGNs in the HDFS for the redshifts intervals shown in every frame. The redshift AGN volume densities derived by Smolčić et al. 2008 are distributed in redshift intervals $z_1 = [0.1, 0.35]$, $z_2 = [0.35, 0.6]$, and $z_3 = [0.6, 0.9]$, and shown as red points in the top right panel and the two at the bottom. Main fit parameters of the Schechter function are shown in the legend.

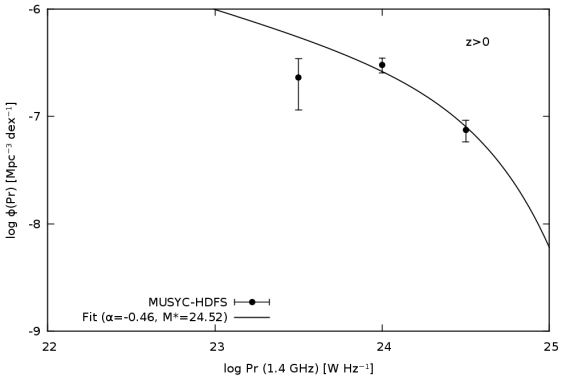

Figure 8.14: 1.4 GHz luminosity functions for radio-loud AGNs in the HDFS for in the redshift range $0.1 < z < 1.0$. Due the small number of sources classified as radio-loud AGNs, a fixed α value is used.

mentioned before, these luminosity functions are quite similar to those presented for all AGNs. The main difference resides on the characteristic luminosity, which gets lower as all high power objects belong to the radio-loud AGN sample.

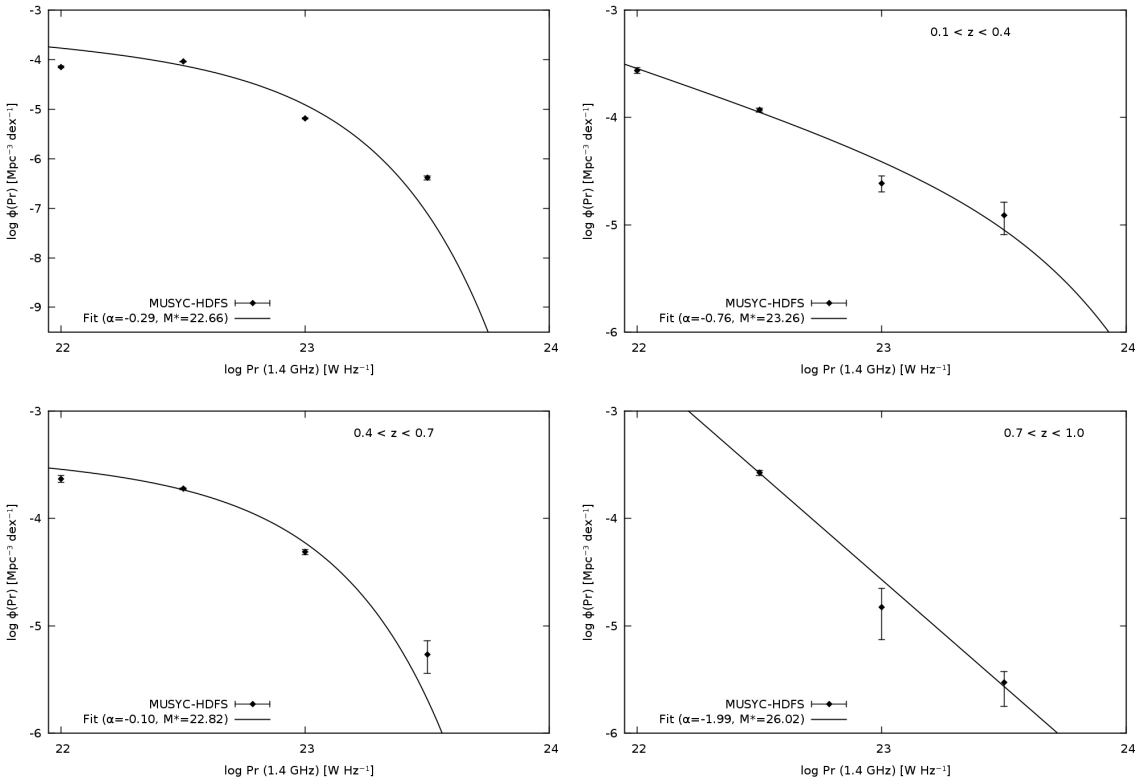

Figure 8.15: 1.4 GHz luminosity functions for radio-quiet AGNs in the HDFS for the redshifts intervals shown in every frame. The top left panel shows the whole sample of identified radio-quiet AGNs. Main fit parameters of the Schechter function are shown in the legend.

Figure 8.16 shows the 1.4 GHz luminosity functions for SFGs in the HDFS for our sample of 101 sources, and separated by our predefined redshift ranges. Data from Padovani et al. 2011 are also included for comparison.

As can be seen we find inconsistencies when comparing with the work done by Padovani et al. 2011 in the bottom left panel corresponding to the [0.4:0.7] redshift bin. The contribution to the volume densities in the range $z = [0.1 : 0.4]$ looks fine, while in the bottom right panel corresponding to $z = [0.7 : 1.0]$, it seems that our data do not follow Padovani's luminosity function, while in the highest redshift bin the data agree again. The similarity at lower redshifts is of particular interest, as in the lowest redshift bin the co-moving volumes are smaller. This redshift bin is the most critical in that sense, and agreements in the comparison can be interpreted as a good sign.

Despite the fact that our redshift ranges are not in perfect agreements with those defined

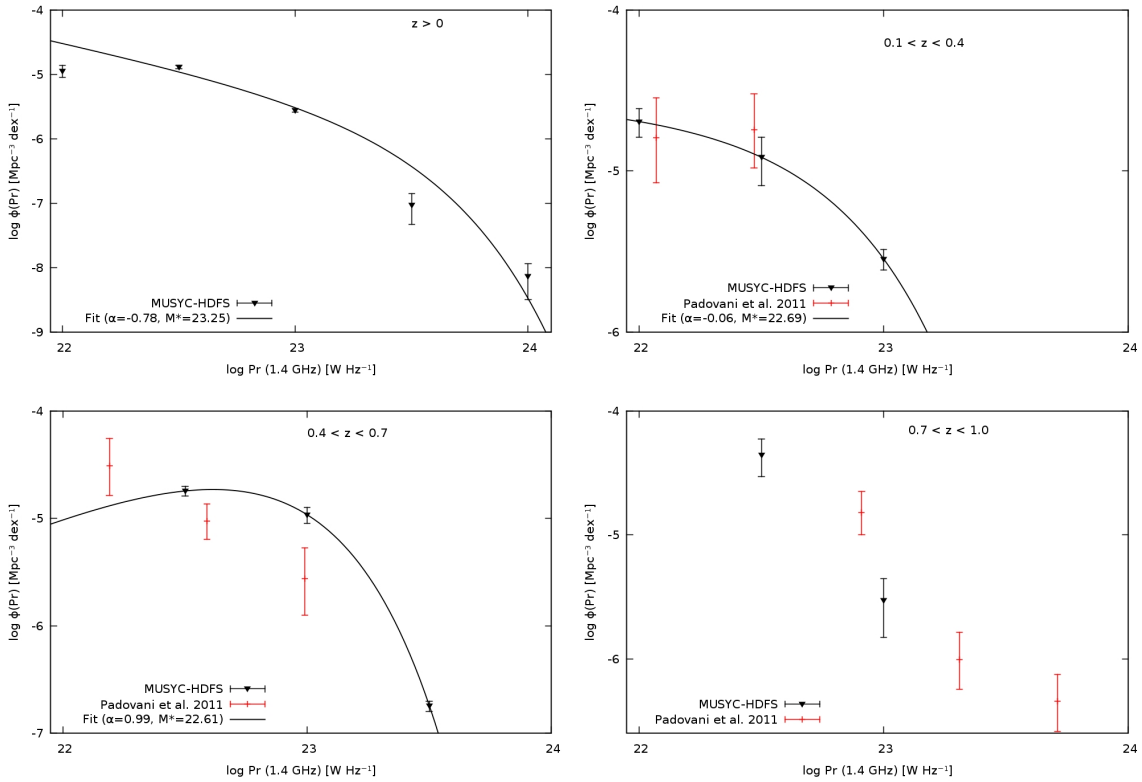

Figure 8.16: 1.4 GHz luminosity functions for SFGs in the HDFS for the redshifts intervals shown in every frame. The top left panel shows the whole sample of identified SFGs. The redshift AGN volume densities derived by Padovani et al. 2011 are distributed in redshift intervals $z_1 = [0.04, 0.22]$, $z_2 = [0.22, 0.53]$, and $z_3 = [0.53, 1.0]$, and shown as red points in the top right panel and the two at the bottom. Main fit parameters of the Schechter function are shown in the legend.

by Padovani et al. 2011, the main differences found at the medium redshift interval should arise due to other factors like the small number of sources available in both samples; wrong redshift determinations which have a large impact onto the luminosity estimates, selection effects, or simply differences in galaxy densities among fields, which has shown to be related to large scale structure fluctuations. These issues can explain the usual differences seen among surveys that aim to find luminosity functions.

Chapter 9

Summary and Conclusions

In the first part of this work we have used existent MUSYC $UBVRIzJHK$ data along with our optical 11-medium bands for the determination of photometric redshifts and the compilation of a uniform catalog of the sources in the Hubble Deep Field South (HDFS). In the second part, we have used radio observations at 1.4, 2.5, 5.2, and 8.7 GHz with a central rms of ~ 10 Jy reached at all frecuencies, and our photometric redshifts, to investigate and discuss the nature of the radio luminosity function, characterize radio sources from microjansky to high flux density levels, and understand the nature of submilijansky sources, their evolution, and luminosity functions.

We determine optimal apertures for accurate photometry for a broad number of object sizes and brightnesses, and provide their uncertainties through an improved technique that considers noise correlations. We performed photometric redshift determinations for the whole uses a template set based on synthetic photometry of galaxies in a semianalytic model which is complete at higher redshifts than spectroscopic samples. To test the reliability on our photometric redshift determinations, we used spectroscopic data from different surveys to analyse the scatter in $z_{\rm phot} - z_{\rm spec}$ diagrams. We compared to nearly ~ 500 spectroscopically identified objects in the field in order to test the accuracy and performance of the medium-band filters. For BVR-selected samples in the HDFS with spectroscopic redshift counterparts, we found a 1 σ scatter

in $\Delta z/(1+z)$ of 0.029. Photometric redshifts show to be more reliable at $R < 24$, particularly at $0.1 < z < 1.2$, by evenly sampling the optical range and strong continuum features such as the Balmer break. Galaxy photometric redshifts degrade in quality for fainter galaxies or when less bands are used.

The radio sample includes a mixture mostly of starburst-dominated and AGN-dominated galaxies. Using the multiwavelength information in the radio and optical bands, radio spectral index when available, SED-types determined through the fitting of our photometry with several galaxy templates, including that of a quasar, and redshift-luminosity dependence, we classified all the sources in our sample into radio-quiet AGNs (46$\%$), radio-loud AGNs (9$\%$), star forming galaxies (39$\%$), and normal galaxies (6$\%$). This classification is discussed in detail for all the sources and is expected to be robust as we applied multiple criteria during the classification procedure.

Among all the criteria used to differentiate active galactic-nuclei from star forming galaxies, the radio-to-optical ratio (R) is not found to be a good discriminant between SFG and AGNs, being more unreliable as redshift increases; Radio power fares somewhat better, but still there is a considerable range where theses two populations overlap; Radio spectral indices do no show a clear trend with spectral galaxy-type, but many sources with $\alpha > 0$ were found, indicating an AGN origin for their emission. When limiting α values only to sources with good signal to noise ratio, many late spectral type sources centered around $\alpha \sim -0.7$, indicating that synchrotron emission is the dominant emission mechanism in these sources.

Combining all these parameters we confirmed previous results that radio sources (radio galaxies and radio-loud AGNs) also make a significant contribution to the sub-milijansky population. Thanks to the faint optical and radio emission levels used in this study, we found that at sub-milinjansky levels star-forming galaxies and RQ-AGNs make up an approximately equal fraction with 46$\%$ and 54% respectively. Some other sources show an unusually high radio-to-optical ratio, which might be caused by dust extinction. There is also some evidence that the luminosity of some galaxies may be generated by a combination of a starburst and AGN.

This classification also provides us a first approximation to support a reliable study of the evolution and luminosity functions of sub-milijansky radio sources, which is important as almost no radio evolution of radio-quiet AGNs is currently available.

The composite template fit turned out to be vital on increasing the number of AGNs. However we expected more radio-loud AGNs to arise in our sample when analizing the porcentual contribution of these sources in other surveys. The lack of these objects in our sample could be explained by cosmic variance.

We find agreements of the LFs between our classified objects and recent works, which based their classification on somewhat different methods demostrating that our photometric redshifts are sufficiently accurate to determine representative radio luminosity functions of galaxies. All these factors verifies that both our selection method, as well as the derivation of the LF seem to be correct.

Chapter 10

Bibliography

Bibliography

Arnouts, S., et al. 2005, *ApJ*, 619, L43

Baade, D., et al. 1999, The Messenger, 95, 15

Bahcall, J. N., & Soneira, R. M. 1981, *ApJS*, 47, 357

Barvainis, R., Lehár, J., Birkinshaw, M., Falcke, H., & Blundell, K. M. 2005, *ApJ*, 618, 108

Baum, W. A. 1962, in IAU Symposium, Vol. 15, Problems of Extra-Galactic Research, ed. G. C. McVittie, 390

Bell, E. F., et al. 2004, *ApJ*, 608, 752

Benítez, N. 1999, in Astronomical Society of the Pacific Conference Series, Vol. 191, Photometric Redshifts and the Detection of High Redshift Galaxies, ed. R. Weymann, L. Storrie-Lombardi, M. Sawicki, & R. Brunner, 31

Bertin, E., & Arnouts, S. 1996, *A&AS*, 117, 393

Best, P. N., Kauffmann, G., Heckman, T. M., Brinchmann, J., Charlot, S., Ivezić, Ž., & White, S. D. M. 2005, *MNRAS*, 362, 25

Binggeli, B., Tammann, G. A., & Sandage, A. 1987, *AJ*, 94, 251

Blaizot, J., Wadadekar, Y., Guiderdoni, B., Colombi, S. T., Bertin, E., Bouchet, F. R., Devriendt, J. E. G., & Hatton, S. 2005, *MNRAS*, 360, 159

Blanc, G. A., et al. 2008, *ApJ*, 681, 1099

Blanton, M. R., & Roweis, S. 2007, *AJ*, 133, 734

Bolzonella, M., Miralles, J.-M., & Pelló, R. 2000, *A&A*, 363, 476

Bower, R. G., Benson, A. J., Malbon, R., Helly, J. C., Frenk, C. S., Baugh, C. M., Cole, S., & Lacey, C. G. 2006, *MNRAS*, 370, 645

Brammer, G. B., van Dokkum, P. G., & Coppi, P. 2008, *ApJ*, 686, 1503

Burstein, D., & Heiles, C. 1978, *ApJ*, 225, 40

Calzetti, D., Kinney, A. L., & Storchi-Bergmann, T. 1994, *ApJ*, 429, 582

Cardamone, C. N., et al. 2010, *ApJS*, 189, 270

Chen, H.-W., et al. 2003, *ApJ*, 586, 745

Croton, D. J., et al. 2006, *MNRAS*, 365, 11

Daddi, E., Cimatti, A., Renzini, A., Fontana, A., Mignoli, M., Pozzetti, L., Tozzi, P., & Zamorani, G. 2004, *ApJ*, 617, 746

Davis, M., et al. 2003, in Society of Photo-Optical Instrumentation Engineers (SPIE) Conference Series, Vol. 4834, Society of Photo-Optical Instrumentation Engineers (SPIE) Conference Series, ed. P. Guhathakurta, 161–172

De Lucia, G., & Blaizot, J. 2007, *MNRAS*, 375, 2

Faber, S. M., et al. 2007, *ApJ*, 665, 265

Falcke, H., Sherwood, W., & Patnaik, A. R. 1996, *ApJ*, 471, 106

Fanaroff, B. L., & Riley, J. M. 1974, *MNRAS*, 167, 31P

Fioc, M., & Rocca-Volmerange, B. 1997, *A&A*, 326, 950

Franceschini, A., et al. 2003, *A&A*, 403, 501

Gawiser, E., et al. 2006, *ApJS*, 162, 1

Glazebrook, K., Verma, A., Boyle, B., Oliver, S., Mann, R. G., & Monbleau, D. 2006, *AJ*, 131, 2383

Grazian, A., et al. 2006, *A&A*, 453, 507

Hamuy, M., Walker, A. R., Suntzeff, N. B., Gigoux, P., Heathcote, S. R., & Phillips, M. M. 1992, *PASP*, 104, 533

Hauschildt, P. H., Allard, F., Ferguson, J., Baron, E., & Alexander, D. R. 1999, *ApJ*, 525, 871

Hopkins, A. M. 2004, *ApJ*, 615, 209

Huynh, M. T., Jackson, C. A., & Norris, R. P. 2007, *AJ*, 133, 1331

Ilbert, O., et al. 2009, *ApJ*, 690, 1236

Kellermann, K. I., Sramek, R., Schmidt, M., Shaffer, D. B., & Green, R. 1989, *AJ*, 98, 1195

Kinney, A. L., Calzetti, D., Bohlin, R. C., McQuade, K., Storchi-Bergmann, T., & Schmitt, H. R. 1996, *ApJ*, 467, 38

Kron, R. G. 1980, *ApJS*, 43, 305

Labbé, I., et al. 2003, *AJ*, 125, 1107

Le Fèvre, O., et al. 2005, *A&A*, 439, 845

Madau, P. 1995, *ApJ*, 441, 18

Metcalfe, N., Shanks, T., Fong, R., & Roche, N. 1995, *MNRAS*, 273, 257

Padovani, P., Mainieri, V., Tozzi, P., Kellermann, K. I., Fomalont, E. B., Miller, N., Rosati, P., & Shaver, P. 2009, *ApJ*, 694, 235

Padovani, P., Miller, N., Kellermann, K. I., Mainieri, V., Rosati, P., & Tozzi, P. 2011, *ApJ*, 740, 20

Palunas, P., et al. 2000, *ApJ*, 541, 61

Pickles, A. J. 1998, VizieR Online Data Catalog, 611, 863

Probst, R. G., et al. 2003, in Society of Photo-Optical Instrumentation Engineers (SPIE) Conference Series, Vol. 4841, Society of Photo-Optical Instrumentation Engineers (SPIE) Conference Series, ed. M. Iye & A. F. M. Moorwood, 411–419

Quadri, R., et al. 2007, *AJ*, 134, 1103

Rafferty, D. A., McNamara, B. R., Nulsen, P. E. J., & Wise, M. W. 2006, *ApJ*, 652, 216

Rigopoulou, D., Vacca, W. D., Berta, S., Franceschini, A., & Aussel, H. 2005, *A&A*, 440, 61

Sadler, E. M., et al. 2002, *MNRAS*, 329, 227

Sandage, A., Binggeli, B., & Tammann, G. A. 1985, *AJ*, 90, 1759

Sawicki, M., & Mallén-Ornelas, G. 2003, *AJ*, 126, 1208

Schechter, P. 1976, *ApJ*, 203, 297

Schiminovich, D., et al. 2005, *ApJ*, 619, L47

Schlegel, D. J., Finkbeiner, D. P., & Davis, M. 1998, *ApJ*, 500, 525

Schmidt, M. 1968, *ApJ*, 151, 393

Seymour, N., et al. 2008, *MNRAS*, 386, 1695

Smolčić, V., et al. 2008, *ApJS*, 177, 14

Springel, V. 2005, *MNRAS*, 364, 1105

Steidel, C. C., Adelberger, K. L., Shapley, A. E., Pettini, M., Dickinson, M., & Giavalisco, M. 2003, *ApJ*, 592, 728

Stocke, J. T., Morris, S. L., Weymann, R. J., & Foltz, C. B. 1992, *ApJ*, 396, 487

Tadhunter, C., et al. 2011, *MNRAS*, 412, 960

Taylor, E. N., et al. 2009, *ApJS*, 183, 295

Teplitz, H. I., Hill, R. S., Malumuth, E. M., Collins, N. R., Gardner, J. P., Palunas, P., & Woodgate, B. E. 2001, *ApJ*, 548, 127

Urry, C. M., & Padovani, P. 1995, *PASP*, 107, 803

van der Bliek, N. S., et al. 2004, in Society of Photo-Optical Instrumentation Engineers (SPIE) Conference Series, Vol. 5492, Society of Photo-Optical Instrumentation Engineers (SPIE) Conference Series, ed. A. F. M. Moorwood & M. Iye, 1582–1589

Wolf, C., Meisenheimer, K., Rix, H.-W., Borch, A., Dye, S., & Kleinheinrich, M. 2003, *A&A*, 401, 73

Wolf, C., et al. 2004, *A&A*, 421, 913

Wuyts, S., van Dokkum, P. G., Franx, M., Förster Schreiber, N. M., Illingworth, G. D., Labbé, I., & Rudnick, G. 2009, *ApJ*, 706, 885